

Neutral meson production in $d + \text{Au}$ and $p + p$
collisions at $\sqrt{s_{NN}} = 200 \text{ GeV}$ in STAR

Oleksandr Grebenyuk

Cover: $p + p$ collision at the center-of-mass energy of 200 GeV, simulated by the PYTHIA event generator and tracked through the complete STAR geometry.

**Neutral meson production in $d + \text{Au}$ and $p + p$
collisions at $\sqrt{s_{NN}} = 200 \text{ GeV}$ in STAR**

**Productie van neutrale mesonen in $d + \text{Au}$ en $p + p$
botsingen bij $\sqrt{s_{NN}} = 200 \text{ GeV}$ in STAR**
(met een samenvatting in het Nederlands)

Proefschrift

TER VERKRIJGING VAN DE GRAAD VAN DOCTOR
AAN DE UNIVERSITEIT UTRECHT
OP GEZAG VAN DE RECTOR MAGNIFICUS, PROF. DR. J.C. STOOF,
INGEVOLGE HET BESLUIT VAN HET COLLEGE VOOR PROMOTIES
IN HET OPENBAAR TE VERDEDIGEN OP
DONDERDAG 29 NOVEMBER 2007 DES OCHTENDS TE 10.30 UUR
DOOR

Oleksandr Grebenyuk

geboren op 27 november 1980 te Ufa, Rusland

Promotor: Prof. dr. Th. Peitzmann
Co-promotor: Dr. M. A. J. Botje

Dit werk maakt deel uit van het onderzoekprogramma van de Stichting voor Fundamenteel Onderzoek der Materie (FOM), financieel gesteund door de Nederlandse Organisatie voor Wetenschappelijk Onderzoek (NWO).

Contents

1	Heavy Ion Physics	1
1.1	Introduction	1
1.2	Heavy ion collisions	4
1.3	Heavy ion physics at RHIC	6
1.4	Proton-proton collisions	12
2	The experiment	15
2.1	RHIC accelerator complex	15
2.2	STAR detector	19
2.2.1	Time Projection Chamber	21
2.2.2	Forward TPC modules	22
2.2.3	Zero Degree Calorimeter	23
2.2.4	Beam-Beam Counter	25
3	STAR Electromagnetic Calorimeter	27
3.1	Mechanical layout	27
3.2	Optical structure	31
3.3	Shower Maximum Detector	32
3.4	Preshower Detector	32
3.5	BEMC electronics	34
4	Event reconstruction in STAR	35
4.1	Data aquisition and trigger	35
4.2	STAR reconstruction chain	36
4.3	BEMC status tables	37
4.4	BEMC energy calibration	38
4.4.1	MIP calibration	39
4.4.2	Electron calibration	40
4.5	Event selection	41

4.5.1	Beam background rejection	41
4.5.2	Vertex reconstruction	42
4.5.3	HighTower trigger condition	45
4.6	Centrality selection in $d + \text{Au}$ data	45
5	Neutral meson reconstruction	47
5.1	BEMC clustering	48
5.2	BEMC cluster cuts	52
5.3	Invariant mass distribution	55
5.4	Combinatorial background	56
5.5	Low-mass background	60
5.6	Yield extraction	63
6	Invariant yield calculation	71
6.1	Acceptance and efficiency correction	72
6.2	Corrections for random vetoes	79
6.3	HighTower trigger scale factors	80
6.4	Vertex finding efficiency	81
6.5	Residual beam background contamination	82
6.6	Bin centering scale factors	83
6.7	Jacobian correction	83
6.8	Fully corrected yields	83
7	Results and discussion	89
7.1	Cross section	89
7.2	Eta to pion ratio	96
7.3	Nuclear modification factor	98
7.4	Conclusions and outlook	103
A	BEMC electronics operation	105
B	STAR Collaboration	111
	Bibliography	113
	Summary	121
	Samenvatting	123
	Acknowledgements	125

Chapter 1

Heavy Ion Physics

1.1 Introduction

Colliding heavy ions in particle accelerators offers a unique opportunity to study the strong interaction of matter in the regime of extremely high densities and temperatures. It is believed that in such collisions temperatures and densities are reached that prevailed in the universe the first few microseconds after the Big Bang.

In the Standard Model of particle physics, the strong interactions between the fundamental quark constituents of matter are described by a field theory called Quantum Chromo Dynamics (QCD) [1]. In this theory the quarks carry a strong charge, called color, and the strong force is mediated between the colored quarks by the exchange of gluons, which are the quanta of the strong field. A very important feature of QCD is that the gluons also carry color charge so that they do not only act as mediators but also themselves couple to the strong force. It turns out that, as a consequence, the potential increases with increasing distance between the color charges. This is in sharp contrast with the field theory of Quantum Electro Dynamics (QED) [2] where the force between electrically charged particles is mediated by the electrically neutral photon. Here the potential vanishes for large distances.

The behavior of the strong coupling with varying distance, which is related to the behavior of the potential as discussed above, has profound phenomenological consequences. First, the coupling between the colored quarks becomes weak at short distances, a property called asymptotic freedom. Such short distances are

probed in hard scattering processes where the momentum exchange between the participating quarks is large. Since the strong coupling is weak in the hard regime, the interaction cross sections can be calculated in a framework called perturbative QCD (pQCD). Because they are calculable, hard scattering processes form a unique probe of the constituents of matter while being, at the same time, a testing ground for the validity of QCD. In this way, QCD has been firmly established as the correct theory of the strong interaction in the last four decades by performing a large variety of experiments on deep inelastic scattering of electrons and muons on protons and neutrons and by the study of electron-positron and proton-(anti)proton collisions at large centre of mass energies in storage rings.

The strong coupling increases with the distance between the quarks and the interaction becomes, in fact, so strong that in ordinary matter the quarks are permanently confined to colorless hadrons. In this regime of large distances or, equivalently, small momentum transfers pQCD breaks down so that it cannot be used to calculate soft scattering cross sections from first principles. However, recently much progress has been made in the understanding of the non-perturbative domain by so-called lattice QCD calculations where the QCD field equations are numerically solved on a discrete space-time lattice [3].

One of the remarkable results of lattice QCD is the prediction that hadronic matter at sufficiently high temperatures and densities will undergo a phase transition to a state of quasi free quarks and gluons. This deconfined dense state of matter is called a Quark Gluon Plasma (QGP). In Figure 1.1 are shown lattice QCD calculations of the energy density ε divided by the fourth power of the temperature T [4]. This dimensionless quantity is proportional to the effective number of degrees of freedom available in the medium. Below the critical temperature T_c the medium consists mainly of confined hadrons while above T_c the quarks and gluons become deconfined causing a rapid increase in the number of degrees of freedom. Figure 1.1 shows that the phase transition occurs when nuclear matter is heated to a temperature T_c of about 175 MeV, corresponding to an energy density of 0.7 GeV/fm^3 .

In the limit of an ideal Stefan-Boltzmann gas the equation of state (EoS) of a QGP is given by

$$P_{\text{SB}} = \frac{\varepsilon_{\text{SB}}}{3} \quad \text{and} \quad \varepsilon_{\text{SB}} = \frac{\pi^2}{30} g T^4, \quad (1.1)$$

where P_{SB} is the pressure, ε_{SB} the energy density, g the effective number of partonic degrees of freedom and T is the temperature [5]. The effective number

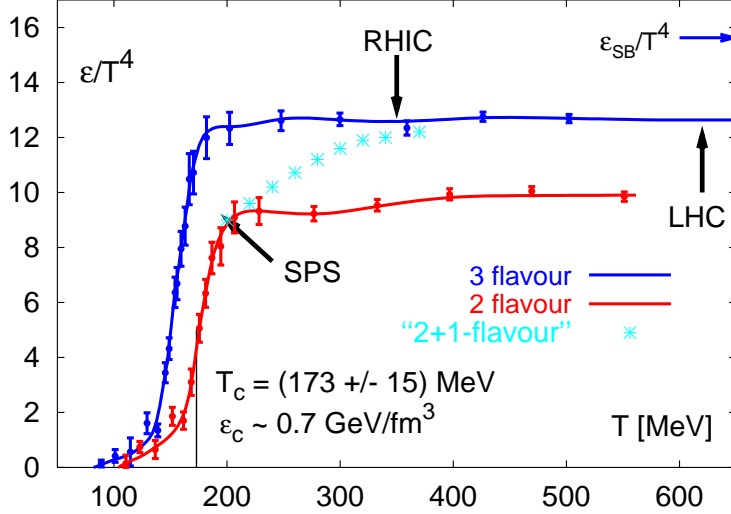


Figure 1.1: The energy density ε scaled by T^4 calculated from lattice QCD with (2, 3) degenerate quark flavors as well as with two light and one heavy (strange) quark. The arrow on the right-hand side shows the Stefan-Boltzmann limit for an ideal quark-gluon gas. The critical temperature T_c and the temperatures which can presumably be reached by RHIC and LHC are also indicated. Figure taken from [4].

of partonic degrees of freedom is given by

$$g = \frac{7}{8} g_q + g_g, \quad (1.2)$$

where g_q and g_g are the degeneracies of, respectively, the quark and gluon states. Each quark flavor has a quark/antiquark state, two spin states and three color states whereas each gluon has two spin states and eight color states. The total degeneracy is therefore given by

$$g = \frac{7}{8} \times n_f \times 2 \times 2 \times 3 + 2 \times 8 = \frac{21}{2} n_f + 16, \quad (1.3)$$

which yields the value $g = 37(95/2)$ for an $n_f = 2(3)$ flavor QGP. This is an order of magnitude larger than for a hadron gas where $g \approx 3$.

The horizontal arrow in Figure 1.1 indicates the Stephan-Boltzmann limit for a QGP with $n_f = 3$ light flavors. The lattice QCD calculation shows that ε/T^4 above T_c remains far below this limit indicating that a QGP, according to these calculations, does not behave as an ideal gas of quarks and gluons.

The possible existence of a QGP was conjectured before the advent of lattice QCD calculations and already in the 1980's experiments started to look for signatures of this plasma in heavy ion collisions. This initiated the rapidly developing field of heavy ion physics and led to a large series of experiments performed at the AGS in Brookhaven, the ISR and the SPS at CERN and, since the year 2000, at the Relativistic Heavy Ion Collider (RHIC) at the Brookhaven National Laboratory (BNL) in the USA.

1.2 Heavy ion collisions

To describe a particle collision we denote by p_A the 4-momentum of particle A moving along the beam (z axis), and by p_B the 4-momentum of particle B moving in the opposite direction. The Lorentz-invariant measure of the square of the center-of-mass energy available in the collision is

$$s = (p_A + p_B)^2. \quad (1.4)$$

The Lorentz-invariant inclusive cross section of the scattering process

$$AB \rightarrow CX$$

is defined by

$$E \frac{d^3\sigma(AB \rightarrow CX)}{d\mathbf{p}^3} = \frac{d^3\sigma}{p_T dp_T dy d\phi}, \quad (1.5)$$

where C is the final state particle being measured and X denotes all other particles produced in the collision [6]. Because of azimuthal symmetry it is convenient to separate longitudinal and transverse momentum components. In Eq. (1.5), E and \mathbf{p} are the energy and 3-momentum, p_T is the transverse component of the momentum, ϕ is the azimuthal angle and y is the rapidity of particle C in the center-of-mass frame. The rapidity is a measure of the longitudinal momentum component p_L and is defined by

$$y = \frac{1}{2} \ln \left(\frac{E + p_L}{E - p_L} \right). \quad (1.6)$$

The rapidity variable has the advantage of being additive under Lorentz boosts along the z axis. Another commonly used variable is the pseudorapidity η , defined by

$$\eta = -\ln \tan(\theta/2), \quad (1.7)$$

which is simply a measure of the polar angle θ and does not depend on the particle mass. This is therefore a convenient variable since it can be calculated without knowing the particle identity. In the limit $E = \sqrt{p^2 + m^2} \approx p \gg m$ of very energetic particles the pseudorapidity η approaches the rapidity y because particle masses can then be neglected.

Because atomic nuclei are spatially extended objects, a characteristic of nucleus-nucleus collisions is the impact parameter b which is the transverse distance between the centers of the two colliding nuclei as shown in Figure 1.2.

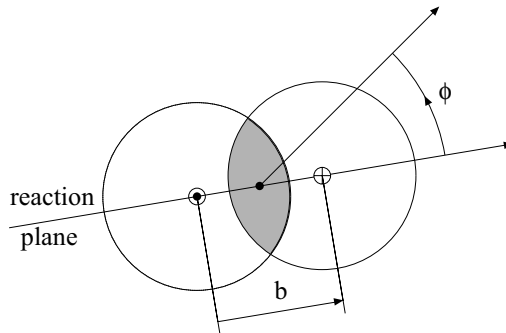


Figure 1.2: Transverse view of two colliding nuclei defining the reaction plane, the impact parameter b and the azimuthal angle ϕ of a produced particle with respect to the reaction plane.

Other measures of the collision centrality are the number of participants N_{part} and the number of binary collisions N_{coll} . The number of binary collisions N_{coll} is defined as the number of individual inelastic nucleon-nucleon collisions which happened during the nucleus-nucleus collision. The number of participants N_{part} is defined as the number of nucleons which suffered at least one inelastic collision with another nucleon. The relation between the impact parameter b and the number of collisions N_{coll} or N_{part} is calculable in the framework of the Glauber model [7].

Experimentally the centrality of a heavy ion collision is estimated from a measurement of one or more quantities which vary monotonically with the impact parameter. Such quantities are the charged particle multiplicity N_{ch} , the transverse energy E_T of all charged particles emitted near midrapidity or the forward energy E_F measured close to the beam line. The relation between the observables and the impact parameter is established by Monte Carlo event generators that model nuclear collisions at relativistic energies [8].

The range of impact parameters can be represented as a fraction of the total geometric cross section. It is customary to define centrality classes as adjacent intervals in b which contain a certain percentile of the differential cross section $d\sigma/db$. For instance, a 0–5% centrality class contains events with five percent of the smallest impact parameters such that it corresponds to five percent of the total geometric cross section.

1.3 Heavy ion physics at RHIC

RHIC is a multipurpose colliding beam facility [9, 10] capable of accelerating protons, deuterons and heavy ions over a broad energy range. At present RHIC has delivered colliding beams of protons, deuterons, copper and gold ions with beam energies of up to 100 GeV per nucleon [11, 12].

An estimate of the energy density in the created medium is obtained from the Bjorken formula [13]

$$\varepsilon_{\text{Bj}} = \frac{dE_T}{dy} \frac{1}{c\tau_0 \pi R^2}, \quad (1.8)$$

where τ_0 is the formation time and R is the initial radius of the expanding system. Using the value $dE_T/d\eta = 503 \pm 2$ GeV measured in central Au + Au collisions [14] and taking $R = 1.2A^{1/3}$ fm, together with reasonable guess for the parameter value $\tau_0 = 1$ fm/c, an initial energy density of about 5 GeV/fm³ is calculated. This is well above the critical energy density of about 1 GeV/fm³ predicted by lattice QCD for a phase transition to the quark-gluon plasma as shown in Figure 1.1. A major part of the physics program at RHIC is therefore to measure particle production in high energy nuclear collisions with the aim to study the properties of the state of matter (presumably a QGP) produced in such collisions.

Particles emitted with large transverse momentum are important probes of the medium produced in the collision because they most likely originate from high energetic partons which propagate through and couple to the created medium and thus carry information about its properties. A convenient way to observe medium-induced modification of particle production is to compare a nucleus-nucleus collision ($A + B$) with an incoherent superposition of the corresponding number of individual nucleon-nucleon collisions ($N + N$). This is done via the nuclear modification factor R_{AB} , defined as the ratio of the particle yield in nucleus-nucleus collisions and the yield in nucleon-nucleon collisions

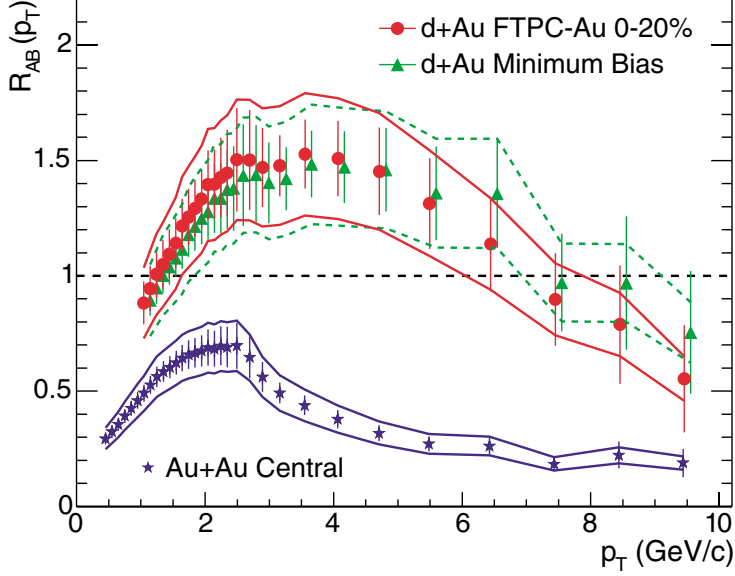


Figure 1.3: Ratio R_{dA} of charged hadron production as a function of p_T measured by the STAR Collaboration in $d + \text{Au}$ and R_{AA} measured in central $\text{Au} + \text{Au}$ collisions at $\sqrt{s_{NN}} = 200$ GeV. Figure taken from [15].

scaled with the number of binary collisions N_{coll}

$$R_{AB} = \frac{d^2 N_{AB} / dp_T dy}{\langle T_{AB} \rangle d^2 \sigma^{p+p} / dp_T dy}. \quad (1.9)$$

Here $\langle T_{AB} \rangle$ is the nuclear overlap function which is related to the number of inelastic nucleon-nucleon collisions in one $A + B$ collision through

$$\langle T_{AB} \rangle \times \sigma_{\text{inel}}^{NN} = \langle N_{\text{coll}} \rangle. \quad (1.10)$$

In the absence of medium effects the nuclear modification factor is unity while $R_{AB} < 1$ indicates a suppression of particle production in heavy ion collisions, compared to an expectation based on an incoherent sum of nucleon-nucleon collisions.

In Figure 1.3 we show the ratio R_{AA} of charged hadron production as a function of p_T measured by the STAR Collaboration in central $\text{Au} + \text{Au}$ collisions at $\sqrt{s_{NN}} = 200$ GeV [15] (the quantity $\sqrt{s_{NN}}$ is the center-of-mass energy of

an individual nucleon-nucleon collision). It is evident that charged particle production in Au + Au collisions is significantly suppressed compared to that in $p + p$ collisions at the same center-of-mass energy, in particular at large $p_T \approx 8 \text{ GeV}/c$ where R_{AA} reaches a value of about 0.2.

Also shown in Figure 1.3 is the nuclear modification factor measured in minimum bias (no centrality selection) and central $d + \text{Au}$ collisions. This measurement is important to distinguish between initial and final state effects. Since we can safely assume that in $d + \text{Au}$ collisions no hot and dense medium is created, the presence of a suppression would indicate initial state effects like nuclear modification of the parton densities in the gold nucleus. It is seen from Figure 1.3 that such suppression is absent in $d + \text{Au}$ collisions, indicating that the suppression observed in Au + Au collisions is a final state effect caused by the dense medium created in such collisions.

A significant enhancement $R_{dA} > 1$ seen in $d + \text{Au}$ collisions in the region $2 < p_T < 7 \text{ GeV}/c$ in Figure 1.3 can be explained by the so-called Cronin effect [16]. This effect is likely caused by multiple scattering of the projectile parton inside the target nucleus, which acts as an additional transverse momentum kick of the parton, overpopulating the $p_T > 2 \text{ GeV}/c$ region. Since there is an indication in Figure 1.3 of a possible suppression in $d + \text{Au}$ collisions at $p_T > 8 \text{ GeV}/c$, it is interesting to measure the R_{dA} factor at even higher p_T . This thesis presents such a measurement.

For peripheral collisions the number of participant nucleons is small and the creation of a dense medium is not expected. This is illustrated in Figure 1.4 which shows the centrality dependence of R_{AA} for charged hadrons as measured by STAR in Au + Au collisions. Indeed, the large suppression observed in central collisions gradually vanishes with decreasing centrality. This suggests that, instead of $p + p$ interactions, peripheral collisions can be used as a reference. This is done through the ratio of particle production in central (C) and peripheral (P) events:

$$R_{CP} = \frac{\langle N_{\text{coll}} \rangle_P}{\langle N_{\text{coll}} \rangle_C} \frac{d^2 N_C / dp_T dy}{d^2 N_P / dp_T dy}. \quad (1.11)$$

The advantage of this measure is that no $p + p$ reference data are needed. The disadvantage is that a stronger model dependence is introduced because the uncertainties in $\langle N_{\text{coll}} \rangle$ are much larger for peripheral collisions. In Figure 1.5 is shown R_{CP} for charged hadrons measured in Au + Au collisions by STAR [17].

To provide a useful reference, it is important to measure particle production in nucleus-nucleus interactions as well as in the $p + p$ collisions under the same experimental conditions. For instance, prior to having the first $p + p$ collisions

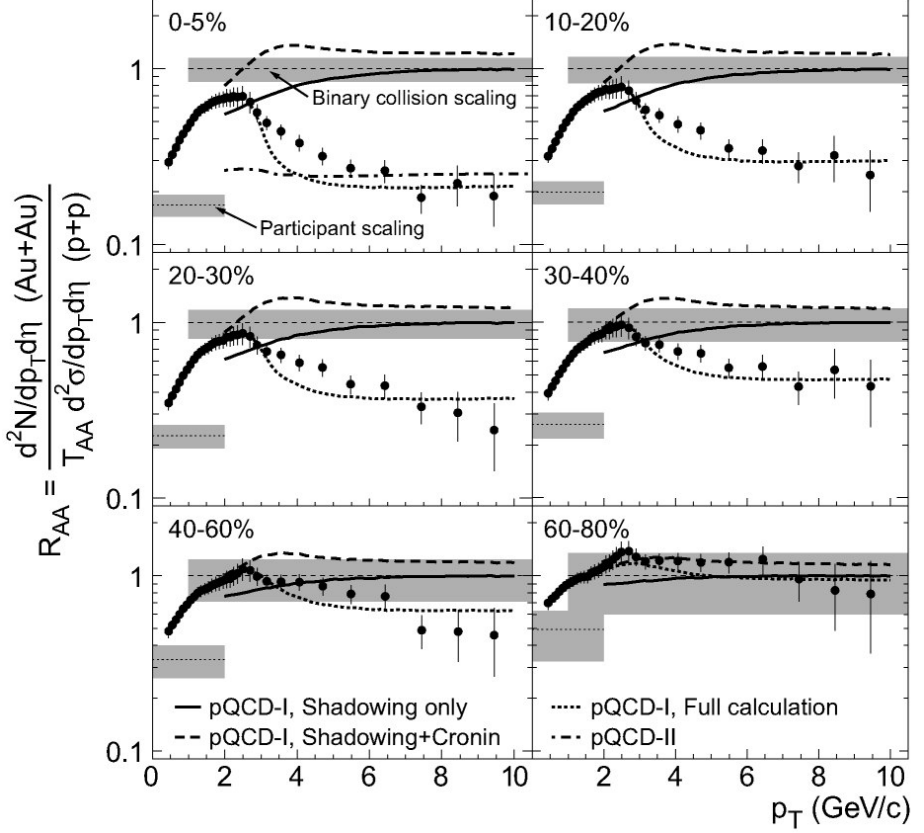


Figure 1.4: Ratio R_{AA} of charged hadron production as a function of collision centrality measured by the STAR Collaboration in Au + Au collisions at $\sqrt{s_{NN}} = 200$ GeV. Figure taken from [17].

delivered by RHIC, both STAR and PHENIX collaborations have published the measurements of R_{AA} [18, 19] based on $p + p$ and $\bar{p} + p$ reference spectra obtained from a large body of world data, extrapolated to RHIC energies. These extrapolations yielded significant systematic uncertainties and more precise measurements of R_{AA} [17, 20] only became available when $p + p$ reference data were taken at RHIC in 2001–2002.

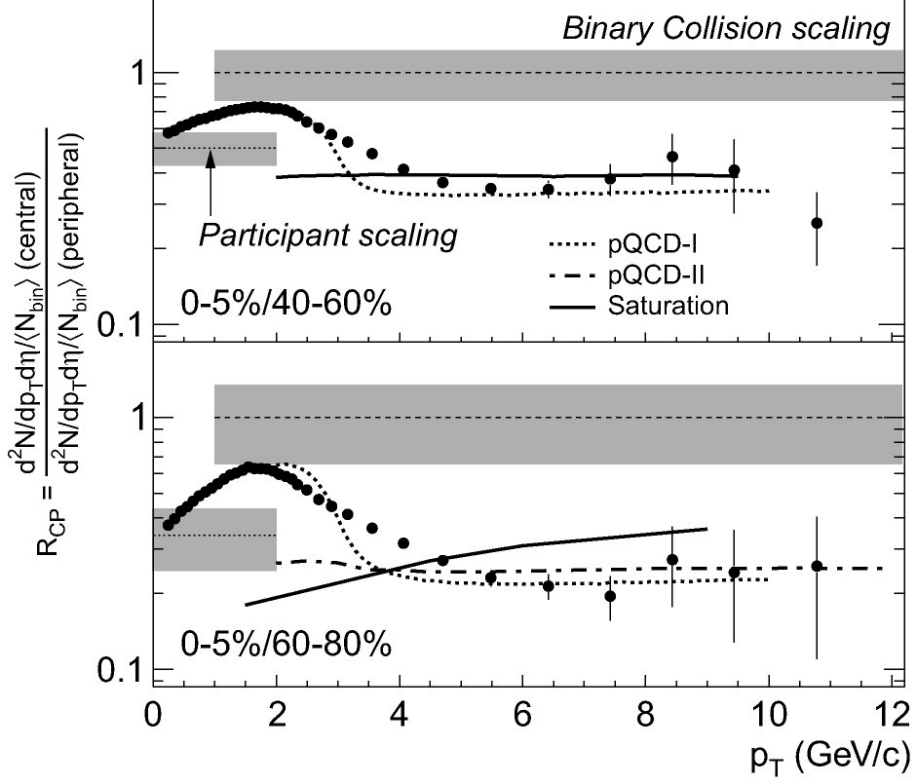


Figure 1.5: Ratio R_{CP} of the charged hadron production measured by the STAR Collaboration in Au + Au collisions at $\sqrt{s_{NN}} = 200$ GeV. Figure taken from [17].

A detailed study of the intermediate- and high- p_T production of different hadron species shows that there is a systematic difference between meson and baryon production in Au + Au collisions, as illustrated in Figure 1.6 [21]. The R_{CP} ratio for identified hadrons is shown separately for mesons (a) and baryons (b), and the clear difference between them suggests that the particle production in this p_T range depends not on the mass of the hadron but rather on the number of valence quarks contained within it. This can be explained naturally in the quark recombination model for hadron formation, rather than fragmentation. We do not discuss here this model and refer to [22, 23, 24, 25, 26, 27] for

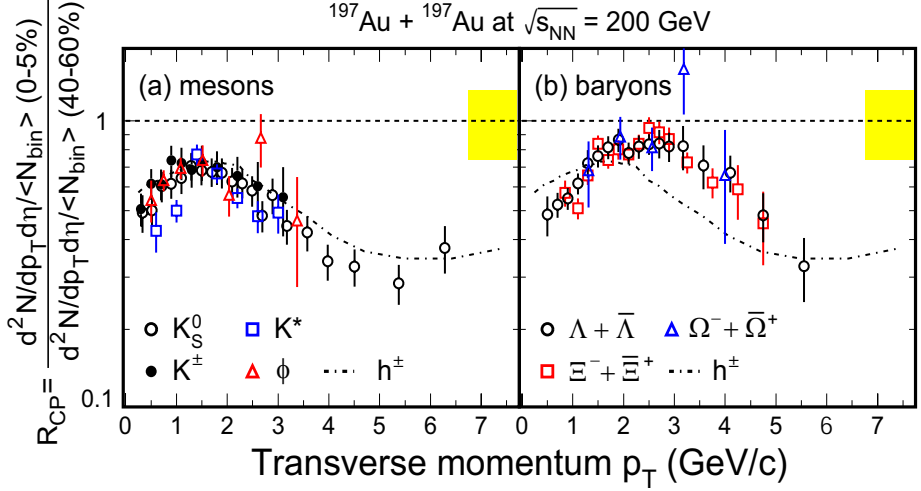


Figure 1.6: Ratio R_{CP} of identified hadron production measured by the STAR Collaboration for mesons (a) and baryons (b) in Au + Au collisions at $\sqrt{s_{NN}} = 200$ GeV. Figure taken from [21].

details. The measurement of R_{CP} for neutral pions and eta mesons would also be interesting in context of this observation.

This thesis presents a baseline measurement with the STAR detector of neutral pion and eta meson production in $p+p$ and $d+Au$ collisions at a center-of-mass energy of $\sqrt{s_{NN}} = 200$ GeV. The neutral pion spectrum complements that of the charged pions measured in STAR in the range $0.35 < p_T < 10$ GeV/c [28] and extends up to $p_T = 17$ GeV/c. Preliminary results of this analysis have been published in [29, 30]. Also presented in this thesis are the first measurements by STAR of η meson production.

1.4 Proton-proton collisions

In QCD, the hadronic interactions are described in terms of the interactions of their constituent partons. The inclusive cross section of the reaction

$$AB \rightarrow CX$$

is calculated as the weighted sum of differential cross sections of all possible parton scatterings that can contribute [6]:

$$E_C \frac{d^3\sigma(AB \rightarrow CX)}{d\mathbf{p}_C^3} = \sum_{abcd} \int_0^1 dx_a \int_0^1 dx_b f_A^a(x_a) f_B^b(x_b) \frac{1}{\pi z_c} \frac{d\sigma(ab \rightarrow cd)}{d\bar{t}} D_c^C(z_c). \quad (1.12)$$

Here $f_A^a(x_a)$ is the parton density function (PDF) giving the probability that hadron A contains a parton a which carries the fraction $x_a = q_a/p_A$ of its momentum. A similar definition applies to the density $f_B^b(x_b)$.

The cross section $d\sigma/d\bar{t}$ of the hard partonic scattering

$$ab \rightarrow cd$$

is calculated in pQCD. The invariant kinematic variables for the partonic sub-process are

$$\begin{aligned} \bar{s} &= (q_a + q_b)^2 \\ \bar{t} &= (q_a - q_c)^2, \end{aligned}$$

where $\sqrt{\bar{s}}$ is the partonic center-of-mass energy and $\sqrt{-\bar{t}}$ is the momentum transfer from a to c .

The fragmentation function $D_c^C(z)$ in Eq. (1.12) describes the probability that a given parton c produces a final state hadron C carrying a momentum fraction $z_c = p_C/q_c$.

From the above it follows that the cross section calculations rely on two inputs — parton densities f_A^a and fragmentation functions D_c^C . These functions are non-perturbative so that they cannot be calculated in QCD from first principles. However, they represent a properties of individual hadrons independent of the process in which they participate. Parton densities and fragmentation functions can therefore be obtained from an analysis of a large variety of scattering data.

A widely used set of parton densities is obtained by the CTEQ Collaboration from a global QCD analysis of a large body of experimental data [31]. The global fit, together with a detailed treatment of published experimental

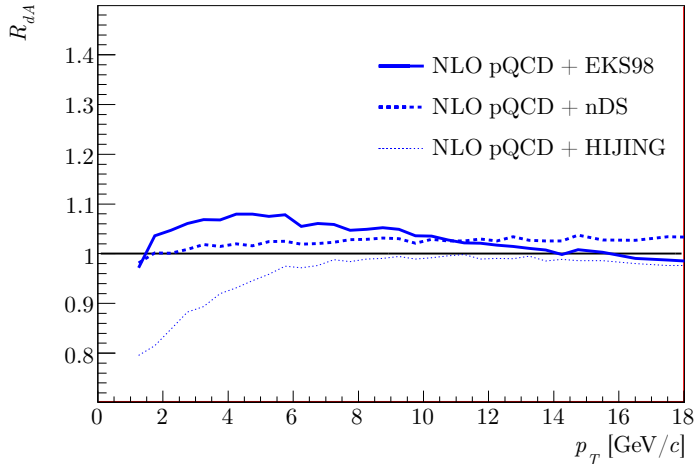


Figure 1.7: Nuclear shadowing effects on the R_{dA} ratio, calculated with EKS98 [37], nDS [38] and HIJING [39] shadowing parametrizations.

uncertainties, resulted in an excellent agreement with all available data. An alternative popular parametrization is MRST [32].

The fragmentation functions $D_c^C(z)$ can be obtained directly from the process $e^+e^- \rightarrow (\gamma, Z) \rightarrow CX$ in which the initial state has no hadrons. Such annihilation process has been measured at many different e^+e^- colliders over a wide range of center-of-mass energies. The most recent parametrizations of fragmentation functions are KKP [33], BKK [34], BFGW [35] and Kretzer [36].

The cross sections of the individual partonic sub-processes are calculated in pQCD with no additional input, except for the strong coupling constant α_S . These calculations are usually performed at next-to-leading order (NLO) or even at next-to-next-to-leading order (NNLO).

An important initial state effect in the heavy ion collisions is the modification of parton distribution functions inside nuclei. It is well known that the quark structure functions at low fractional momentum are depleted in a nucleus relative to a free nucleon. This depletion is commonly referred to as nuclear shadowing. In Figure 1.7 we show the shadowing effects in $d + \text{Au}$ collisions on the R_{dA} ratio [40], calculated with different parametrizations — EKS98 [37], nDS [38] and HIJING [39]. It is also a motivation for the present analysis to observe the nuclear shadowing and differentiate between models, although the required experimental precision may be prohibitively high.

Chapter 2

The experiment

2.1 RHIC accelerator complex

The STAR experiment is located at the Brookhaven National Laboratory (BNL) on Long Island, USA. An important part of the physics program of the Laboratory is carried out at the Relativistic Heavy Ion Collider (RHIC). This is a multipurpose colliding beam facility [9, 10] capable of accelerating protons, deuterons and heavy ions over a broad energy range from the injection energy per nucleon of 10 GeV/ u up to the top energy of 100 GeV/ u for heavy ions and 250 GeV for protons.

The layout of the accelerator complex is shown in Figure 2.1. Heavy ions are accelerated in the Tandem Van de Graaff accelerator, the Booster, the Alternating Gradient Synchrotron (AGS), and in the RHIC accelerator itself. The Linac serves to accelerate protons which are then injected into the Booster. Below we will give a short description of each component of the accelerator complex.

Tandem Van de Graaff generator Gold ions with unit negative charge are generated in the Pulsed Sputter Ion Source which delivers 250 μ A pulses of 600 μ s duration each. The ions are then accelerated in the Tandem Van de Graaff generator from the ground to +14 MV potential. They pass a set of stripping foils where they acquire a unit positive charge and are subsequently accelerated again to the ground potential. The 1 MeV/ u ions leaving the Tandem are stripped further to a charge of +32. There are two identical Tandems available to provide two different ion species simultaneously (presently deuterium

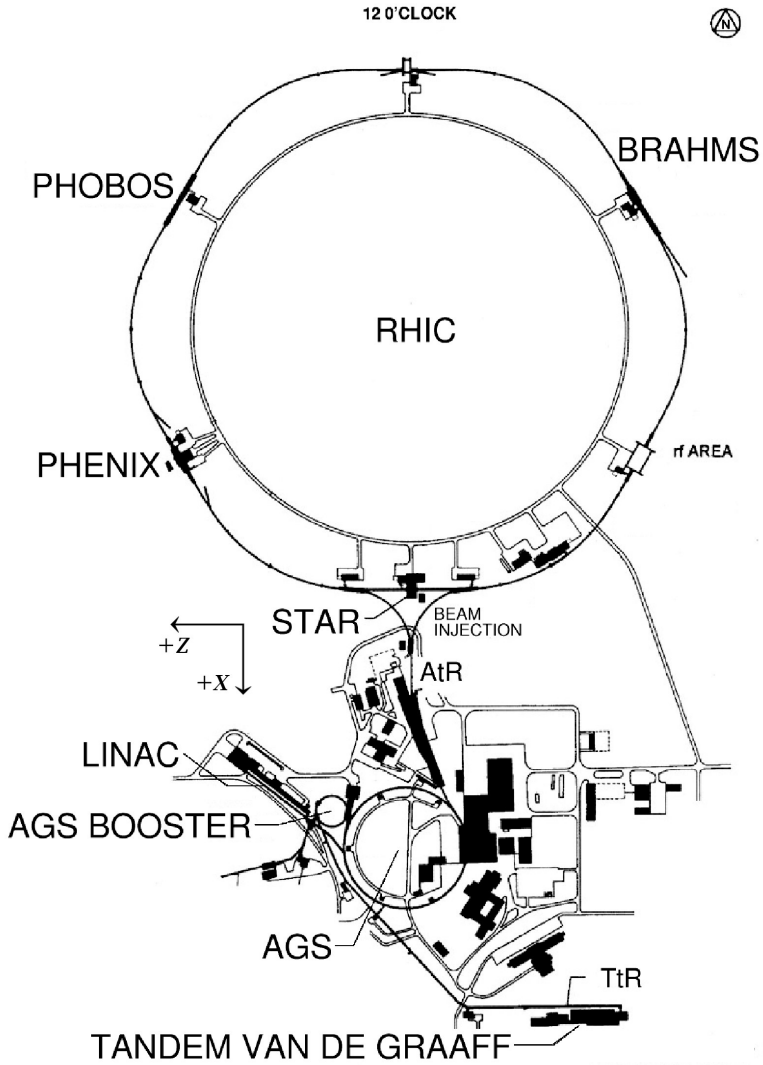


Figure 2.1: Layout of the RHIC accelerator complex. Shown are the locations of the STAR, PHENIX, PHOBOS and BRAHMS experiments around the RHIC ring. Also indicated in the figure is the STAR coordinate system with the positive z axis pointing in the West direction. Figure taken from [9].

and copper in addition to gold).

LINAC The LINAC serves to accelerate protons to an energy of 200 MeV, which are injected directly into the Booster.

Booster synchrotron The 600 μ s long Tandem pulse is injected into the Booster after which the particles are captured into six bunches and accelerated to an energy of 95 MeV/ u . Gold ions, when they are extracted from the Booster, are stripped to the charge +77, leaving only two tightly bound K -shell electrons to be stripped at a later stage in the acceleration chain.

AGS From the Booster, 24 bunches are injected into the AGS and rearranged into four final bunches containing 10^9 ions each. Those bunches are accelerated to an energy of about 10 GeV/ u . When transferred to the RHIC accelerator, the ions are fully stripped to the charge +39 in case of copper and +79 in case of gold.

RHIC accelerator The final stage of acceleration takes place in the RHIC synchrotron where beams are circulating in two rings in opposite directions. The rings have a circumference of 3.83 km and are equipped with independent bending and focusing magnets and RF cavities. This provides the capability of operating the accelerator with two beams of unequal species. The bending magnets are superconductive and cooled by liquid helium. The complete cooling of the rings from room temperature to the operating temperature of 4.6°K takes about ten days.

Up to 120 bunches can be injected in each ring and accelerated to an energy between 30 and 100 GeV/ u . After acceleration the bunches are transferred to the storage RF system which maintains the bunch length at 1.52 m or 5 ns. The lifetime of a stored beam is about 10 hours, whereafter the beam is dumped and a new fill begins. A chosen pattern of empty buckets provides a sample of unpaired bunches crossing each interaction region for beam-background studies.

Beams are made to cross at six points along the ring, four of which are used by the experiments STAR [41], PHENIX [42], PHOBOS [43] and BRAHMS [44]. Of the remaining two crossing points, one is occupied by the RF system while the other is not used at present.

Table 2.1: RHIC runs in the years 2000–2007.

Run	Year	Particle species	Beam energy [GeV/ u]	Integrated luminosity [pb^{-1}]	Average beam polarization [%]
Run-1	2000	Au + Au	27.9	$< 10^{-9}$	
		Au + Au	65.2	20×10^{-6}	
Run-2	2001–2002	Au + Au	100.0	258×10^{-6}	
		Au + Au	9.8	0.4×10^{-6}	
		$p + p$	100.0	1.4	14
Run-3	2002–2003	$d + \text{Au}$	100.0	73×10^{-3}	
		$p + p$	100.0	5.5	34
Run-4	2003–2004	Au + Au	100.0	3740×10^{-6}	
		Au + Au	31.2	67×10^{-6}	
		$p + p$	100.0	7.1	46
Run-5	2004–2005	Cu + Cu	100.0	42.1×10^{-3}	
		Cu + Cu	31.2	1.5×10^{-3}	
		Cu + Cu	11.2	0.02×10^{-3}	
		$p + p$	100.0	29.5	46
		$p + p$	204.9	0.1	30
Run-6	2006	$p + p$	100.0	93.3	58
		$p + p$	31.2	1.05	50
Run-7	2006–2007	Au + Au	100.0	7250×10^{-6}	

RHIC performance To date, RHIC has delivered a variety of colliding beams of protons, deuterons, copper (Cu^{29+}) and gold ions (Au^{79+}) [11, 12].

In Table 2.1 we list the RHIC runs from the beginning of operations in the year 2000 up to the year 2007. The $p + p$ runs provide reference data for the heavy ion physics program as well as data to measure the proton spin structure at RHIC. For this purpose the proton beams are polarized, reaching degrees of up to 60% in 2006. The data used in this thesis are taken in the $d + \text{Au}$ run in 2002/03 and $p + p$ in 2005, both at center-of-mass energies of 200 GeV/ u .

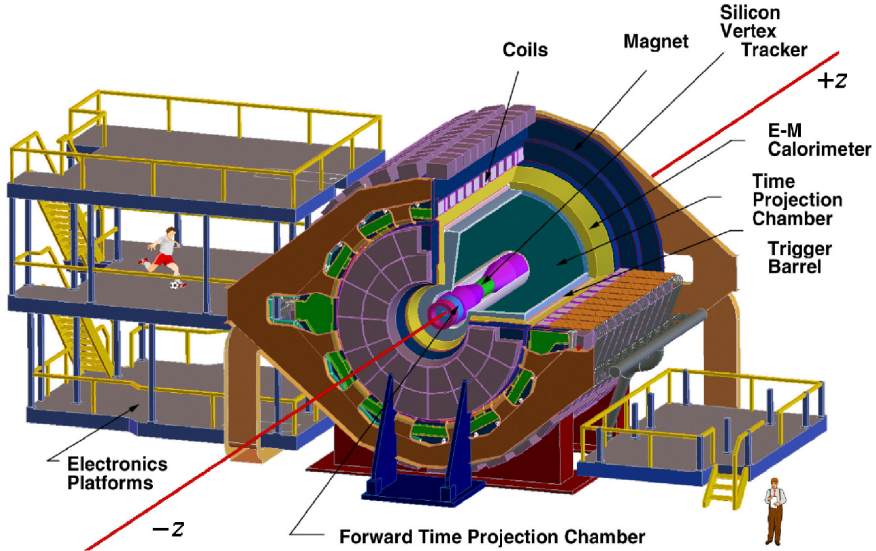


Figure 2.2: Perspective view of the STAR detector. Figure taken from [41].

2.2 STAR detector

The STAR detector (Solenoidal Tracker At RHIC) [41] was designed primarily for measurements of hadron production in heavy ion and proton-proton collisions over a large solid angle. For this purpose large acceptance high granularity tracking detectors are placed inside a large volume magnetic field. A perspective view of the detector is shown in Figure 2.2 and a cutaway side view in Figure 2.3.

The barrel tracking detectors in STAR are a Silicon Vertex Tracker surrounding the beam pipe (SVT, not used in this analysis) and a large volume Time Projection Chamber (TPC) with an inner radius of 0.5 m, an outer radius of 2 m and a length of 4.2 m. The TPC covers a pseudorapidity range of $|\eta| < 1.8$ and is designed to reconstruct the very high multiplicity events produced in heavy ion collisions. These multiplicities can reach up to 1000 charged tracks per unit rapidity in a central Au + Au collision at the largest beam energies. High granularity tracking in the forward and backward regions is achieved by two Forward TPCs (FTPC), each covering a range of $2.5 < |\eta| < 4$ in pseudorapidity.

For trigger purposes, the TPC is surrounded by a layer of scintillator tiles (Central Trigger Barrel, CTB), not used in this analysis.

To trigger on the energy deposited by high transverse momentum photons,

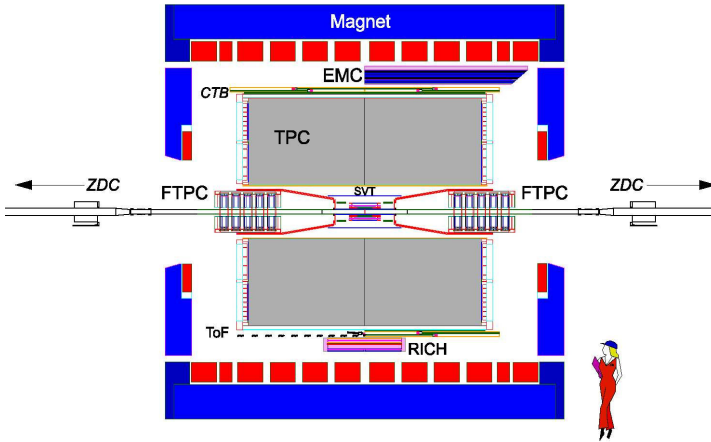


Figure 2.3: Cutaway side view of the STAR detector as configured in 2001. Figure taken from [41].

electrons and electromagnetically decaying hadrons, a Barrel Electromagnetic Calorimeter (BEMC) [45] was incrementally added to the STAR setup from the year 2001 to 2005.

The calorimeter surrounds and covers the full acceptance of the TPC and CTB. An Endcap Electromagnetic Calorimeter (EEMC) [46] was installed in 2002–2003 to cover the pseudorapidity range $1 < \eta < 2$. In the data taking period covered by this thesis only the West half of the BEMC was fully operational ($0 < \eta < 1$).

The STAR barrel detectors are placed inside a room temperature solenoidal magnet with maximum field of 0.5 T. The inner dimensions of the magnet are 5.8 m in length and 5.27 m in diameter.

To provide a minimum bias trigger and to measure centralities in heavy ion collisions two sampling calorimeters (ZDC) are placed in the RHIC tunnel at 18 m from the interaction point. Tiled arrays of scintillator counters (Beam-Beam Counter, BBC) are mounted around the beam pipe at a distance of 3.7 m from the interaction point to provide a minimum bias trigger in $p + p$ collisions. The detector subsystems relevant for the present analysis are briefly described in the following sections. We refer to Chapter 3 for a detailed description of the BEMC which plays a central role in the analysis.

Throughout this thesis we will use a Cartesian coordinate system defined as follows: z pointing along the beam in the West direction (see Figure 2.1), y pointing upward, right-handed.

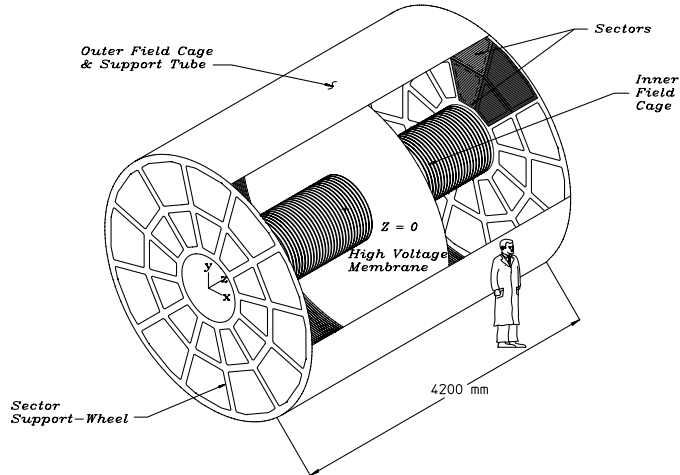


Figure 2.4: Schematic perspective view of the STAR TPC. Figure taken from [47].

2.2.1 Time Projection Chamber

The Time Projection Chamber [47] is the central tracking device in STAR. It allows to track charged particles, measure their momenta and identify the particle species by measuring the ionization energy loss dE/dx .

A schematic layout of the TPC is shown in Figure 2.4. The TPC barrel measures 4.2 m in length and has an inner radius of 0.5 m and an outer radius of 2 m. The TPC acceptance covers ± 1.8 units in pseudorapidity and full azimuth. Particles are identified over a momentum range from 100 MeV/ c to 1 GeV/ c and their momentum is measured in the range from 100 MeV/ c to 30 GeV/ c .

The TPC is a gas filled cylindrical volume with a well defined uniform electric field gradient of about 135 V/cm. The secondary electrons released by ionizing particles along their path drift in the electric field towards the readout endcaps. The electric field is generated between a central membrane held at 28 kV potential and the endcaps which are held at ground potential. A uniform field gradient is maintained by concentric equi-potential field cage cylinders biased via 2 M Ω resistors. The drift volume is filled with a gas mixture of 10% methane and 90% argon which is held slightly above atmospheric pressure. The drift

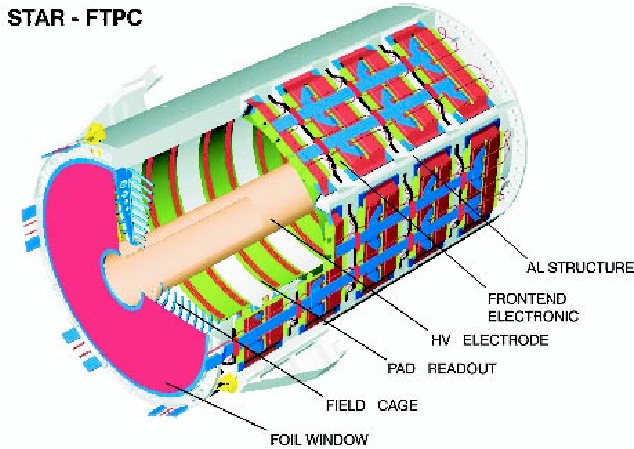


Figure 2.5: Perspective view of a STAR FTPC. Figure taken from [48].

velocity is $5.45 \text{ cm}/\mu\text{s}$ and the maximum drift time from the central membrane to endcap is $38.5 \mu\text{s}$.

The endcaps are instrumented with Multi-Wire Proportional Chambers (MWPC) with pad readout. The transverse coordinates of a track are reconstructed from the hits in the MWPCs while the z coordinate is reconstructed from a measurement of the drift time. The total drift time of $5.45 \mu\text{s}$ is sampled by the readout electronics in 512 time buckets.

In each endcap, the MWPCs are arranged in 12 sectors, each consisting of inner and outer sub-sector. The inner sub-sectors are in the region of highest track density and are therefore optimized for better two-track resolution while the outer sub-sectors are optimized for better performance in the measurement of dE/dx .

In the analysis presented in this thesis the TPC is used as a charged particle veto in the identification of photons in the BEMC. Samples of electrons reconstructed in the TPC serve to calibrate the energy response of the BEMC.

2.2.2 Forward TPC modules

Two Forward Time Projection Chambers (FTPC) [48] extend the STAR tracking capability to the pseudorapidity range $2.5 < |\eta| < 4$. The layout of the FTPC is shown in Figure 2.5. Each FTPC is a cylindrical volume with a

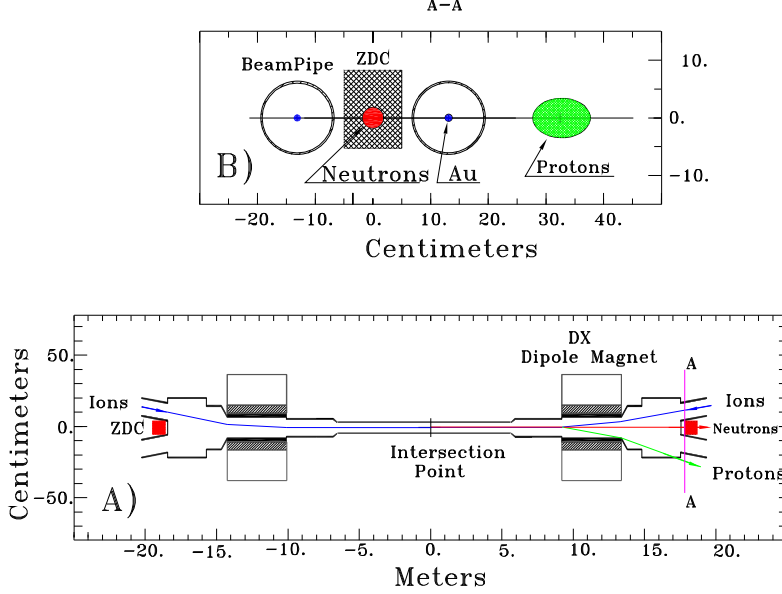


Figure 2.6: Transverse view of the collision region indicating the beam pipes, the Zero Degree Calorimeter and the impact regions of neutrons and charged fragments with $Z/A = 1$ (top). Top view showing the position of the ZDC modules behind the DX dipole magnets in between the two RHIC beam pipes (bottom). Figure taken from [49].

diameter of 75 cm and a length of 120 cm, with radial drift field and pad read-out chambers mounted on the outer cylindrical surface. Two such detectors are installed partially inside the main TPC on both sides of the interaction point. The FTPC is capable of reconstructing all charged tracks (typically 1000) traversing the detector in a central Au + Au event.

In this thesis, the forward charged track multiplicity recorded in the FTPCs is used as a measure of the centrality in $d + \text{Au}$ collisions.

2.2.3 Zero Degree Calorimeter

In addition to the STAR barrel detectors, a sampling calorimeter is placed at a distance of 18 m from the interaction point in the RHIC tunnel on both sides of the experimental hall, as shown in Figure 2.6. These Zero Degree Calorimeters (ZDC) [50, 49] are used to provide the minimum bias trigger and to measure centralities in heavy ion collisions. Furthermore, identical ZDC detectors are

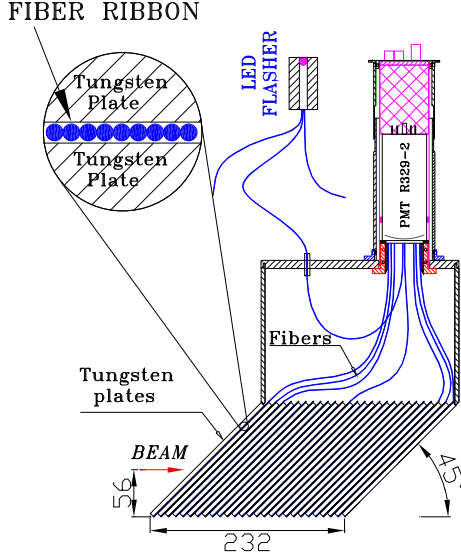


Figure 2.7: Mechanical design of the ZDC modules. Figure taken from [49].

installed at each of the four RHIC experiments providing comparable collision rate measurements to monitor the RHIC luminosity.

The ZDC detector measures the total energy of the unbound neutrons emitted from the nuclear fragments after a collision. The charged fragments of the collision are bent away by the RHIC dipole magnets DX. In the upper plot of Figure 2.6 is shown a transverse view at the front face of the ZDC indicating the position of the two beam pipes, the neutron spot inside the ZDC acceptance and the spot of deflected fragments with $Z/A = 1$.

The mechanical layout of the ZDC is shown in Figure 2.7. It consists of alternating layers of tungsten absorber and Cherenkov fibers with a total length of about 0.7 m. The transverse dimension of $x \times y = 10 \times 13.6 \text{ cm}^2$ corresponds to an angular acceptance of about 2.5 mrad around the forward direction.

In this thesis we do not use the ZDC for centrality measurement and refer to [49] for details on such a measurement. For the $d + \text{Au}$ data used in the present analysis, the ZDC provided a minimum bias trigger by requiring the detection of at least one neutron in the Au beam direction. The acceptance of this trigger corresponds to $95 \pm 3 \%$ of the total $d + \text{Au}$ geometrical cross section as determined from detailed simulations of the ZDC acceptance [15].

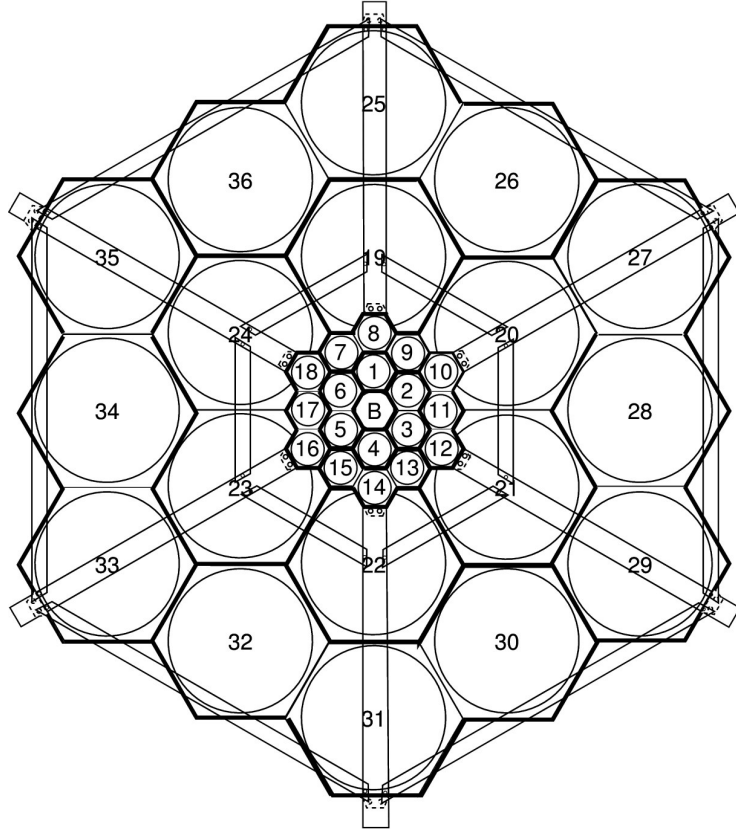


Figure 2.8: Schematic view of the BBC detector. Figure taken from [52].

2.2.4 Beam-Beam Counter

To provide a minimum bias trigger in $p + p$ collisions, Beam-Beam Counters (BBC) [51, 52] are mounted around the beam pipe beyond both poletips of the STAR magnet at a distance of 3.7 m from the interaction point. The BBC also serves to reject beam-gas events at the trigger level and to measure the beam luminosity in $p + p$ runs.

The detector consists of two sets of hexagonal scintillator tiles, see Figure 2.8. A ring with radius between 9.6 and 48 cm is formed by 18 small tiles while 18 large tiles on the outside cover a radius between 38 and 193 cm. The small

and large tile arrangements cover the pseudorapidities $3.4 < |\eta| < 5.0$ and $2.1 < |\eta| < 3.6$, respectively.

In $p + p$ runs, a minimum bias trigger is provided by a coincidence of signals in at least one of the 18 small BBC tiles on each side of the interaction region.

The two BBC counters also record the time of flight which provides a measurement of the z position of the interaction vertex to an accuracy of about 40 cm. Large values of the time of flight difference between the two BBC counters indicate the passage of beam halo which is rejected at the trigger level.

A measurement of the counting rate in the BBCs allows for a determination of the absolute luminosity to an accuracy of about 15%, the relative luminosities per run are determined to a precision of better than 10^{-3} [51, 52].

Chapter 3

STAR Electromagnetic Calorimeter

The Barrel Electromagnetic Calorimeter (BEMC) [45] is a lead-scintillator sampling calorimeter surrounding the STAR TPC as shown in Figure 3.1. The BEMC was installed in several stages during the period of 2001–2005. Only the West half of the BEMC was fully operational during the 2003 and 2005 runs which provided the data presented in this thesis. The Endcap Calorimeter [46], which is not used in the present analysis, was installed in the years 2002–2003.

The BEMC is used to trigger on and to measure jets, leading hadrons, direct photons and electrons from heavy quarks produced at large transverse momentum. For this purpose, the BEMC provides large acceptance for photons, electrons, π^0 and η mesons in all colliding systems ranging from $p + p$ up to $\text{Au} + \text{Au}$. In the next sections we will describe the BEMC in more detail.

3.1 Mechanical layout

The calorimeter is located inside the magnet coil and surrounds the TPC. It covers a pseudorapidity range of $|\eta| < 1$ and full azimuth, matching the TPC acceptance. The calorimeter is divided in two adjacent barrels, one positioned at the West half of the STAR detector ($0 < \eta < 1$) and the other one at the East half ($-1 < \eta < 0$). Each half barrel has a length of 293 cm, an inner radius of 223 cm and an outer radius of 263 cm.

The half barrel is azimuthally segmented into 60 modules. Each module is

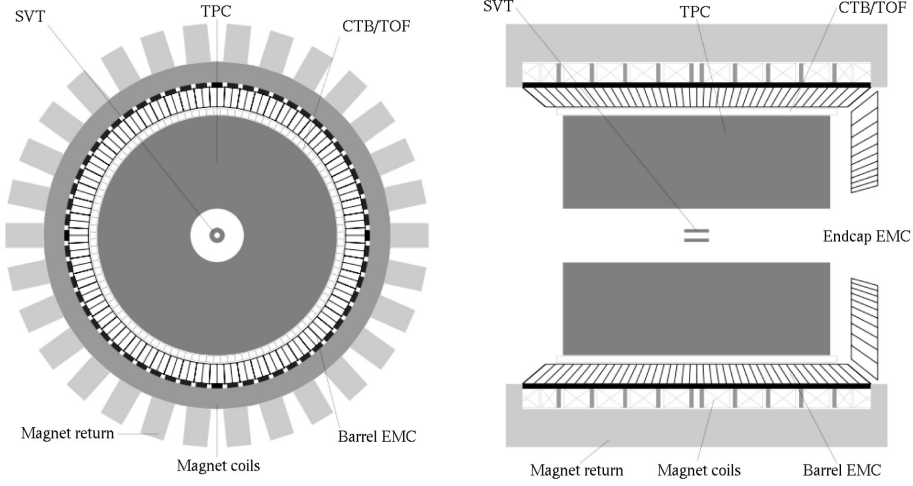


Figure 3.1: Cross-sectional and longitudinal view of the STAR detector showing the layout of the BEMC. Figure taken from [45].

approximately 26 cm wide and covers 6 degrees (17 mrad) in azimuth and one unit in pseudorapidity. The active depth is 23.5 cm to which is added 6.6 cm of structural elements at the outer radius. The longitudinal and transverse segmentation of a module is shown in Figure 3.2 and the radial structure in Figure 3.3.

The modules are segmented into 40 projective towers of lead-scintillator stacks, 2 in ϕ and 20 in η . A tower covers 0.05 in $\Delta\phi$ and 0.05 in $\Delta\eta$. Each calorimeter half is thus segmented into a total of 2400 towers.

Each tower consists of an inner stack of 5 layers of lead and 5 layers of scintillator and an outer stack of 15 layers of lead and 16 layers of scintillator. All these layers are 5 mm thick, except the innermost two scintillator layers which are 6 mm thick. A separate readout of these latter two layers provides the calorimeter preshower signal. A Shower Maximum Detector (SMD) is positioned between the inner and outer stacks at a depth of approximately 5 radiation lengths. The whole stack is held together by mechanical compression and friction between layers.

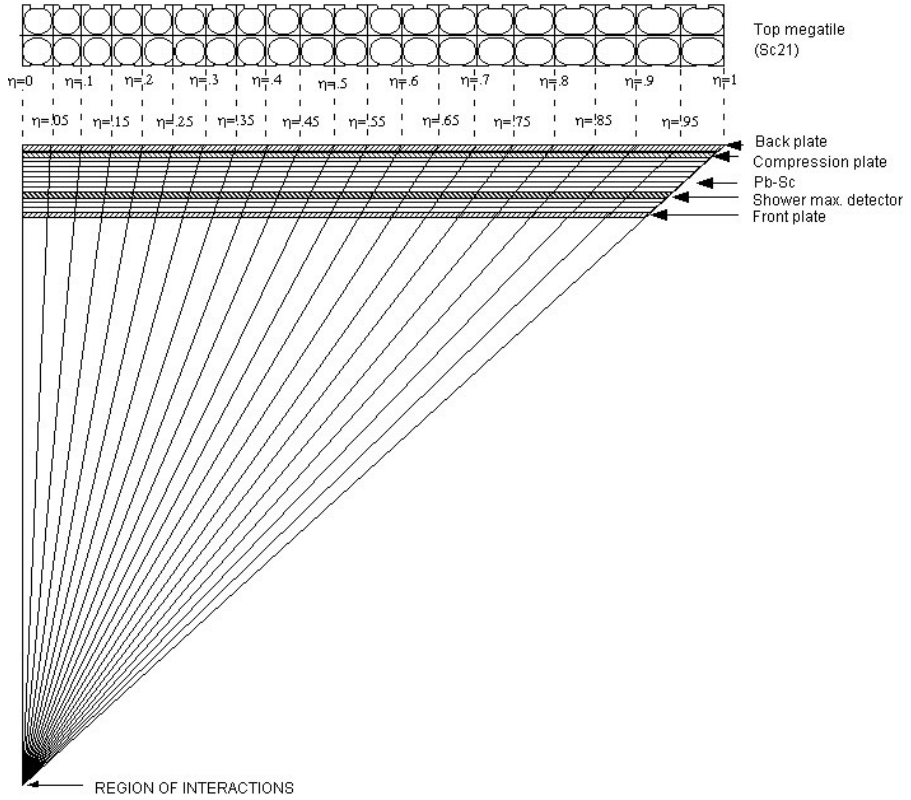


Figure 3.2: Side view of a calorimeter module and top view of a scintillator plate segmented into 20×2 towers. Figure taken from [45].

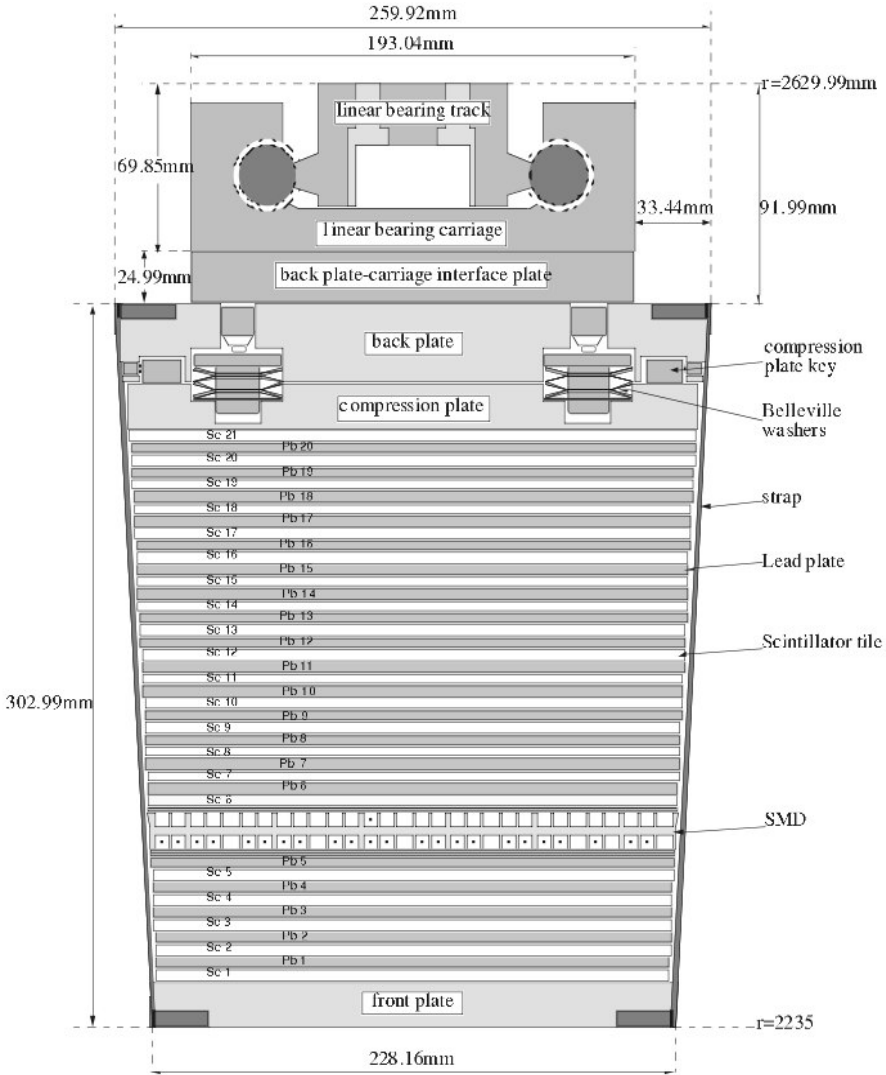


Figure 3.3: Transverse view of a calorimeter module showing the inner layer of lead/scintillator stacks, the shower maximum detector (SMD), the outer layer of stacks and the carriage structure at the outer radius of the BEMC barrel. Figure taken from [45].

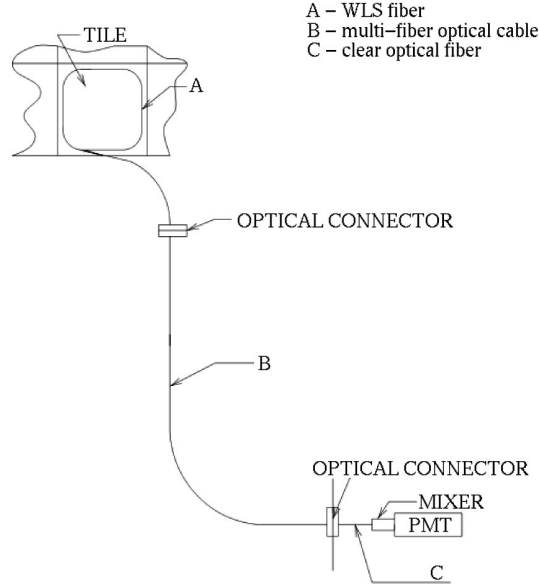


Figure 3.4: Optical readout scheme of a BEMC tower. Figure taken from [45].

3.2 Optical structure

The plastic scintillator layers are machined as “megatiles”, covering the full length and width of a module. These megatiles are segmented into 40 optically isolated tiles, as shown in the top diagram of Figure 3.2. The optical separation between the individual tiles is achieved by 95% deep cuts in the scintillator filled with opaque epoxy. The optical crosstalk between adjacent tiles is reduced to a level of 0.5% by painting a black line on the surface opposite to the isolation groove.

The optical readout scheme is shown in Figure 3.4. The signal from each tile is collected by a wavelength shifting (WLS) fiber embedded in a σ -groove in the tile. The WLS fibers run along the outer surface of the stack and terminate in an optical connector mounted at the back-plate of the module. From the back-plate, 2.1 m long fibers run through the STAR magnet structure to the readout boxes mounted on the outer side of the magnet. In these boxes the 21 fibers from the tiles of one tower are connected to a single photomultiplier tube (PMT). The PMTs are powered by Cockroft-Walton bases that are remotely

controlled over a serial communication line by the slow control software.

From layer by layer tests of the BEMC optical system, together with an analysis of cosmic ray and test beam data, the nominal energy resolution of the calorimeter is estimated to be $\delta E/E = 15\%/\sqrt{E[\text{GeV}]} \oplus 1.5\%$ [53].

3.3 Shower Maximum Detector

The Shower Maximum Detector (SMD) is a multi-wire proportional counter with strip readout. It is located at a depth of approximately 5.6 radiation lengths at $\eta = 0$ increasing to 7.9 radiation lengths at $\eta = 1$, including all material immediately in front of the calorimeter.

The purpose of the SMD is to improve the spatial resolution of the calorimeter. This is necessary because the transverse dimension of each tower (about $10 \times 10 \text{ cm}^2$) is much larger than the lateral spread of an electromagnetic shower. The improved resolution is essential to separate the two photon showers originating from the decay of high momentum π^0 and η mesons.

The layout of the SMD is shown in Figure 3.5. Independent cathode planes with strips along η and ϕ directions allow the reconstruction of a two dimensional image of a shower. The coverage in $\Delta\eta \times \Delta\phi$ is 0.0064×0.1 for the η strips and 0.1×0.0064 for the ϕ strips. There are a total of 36000 strips in the full detector.

Beam test results at the AGS have shown that the SMD has an approximately linear response versus energy. The energy resolution in the η coordinate (front plane) is approximately $\delta E/E = 86\%/\sqrt{E[\text{GeV}]} \oplus 12\%$ whereas that in the ϕ coordinate (back plane) is worse by about 3–4%. The position resolution is $\sigma(r\phi) = 5.6/\sqrt{E[\text{GeV}]} \oplus 2.4 \text{ mm}$ and $\sigma(z) = 5.8/\sqrt{E[\text{GeV}]} \oplus 3.2 \text{ mm}$.

3.4 Preshower Detector

The first and second scintillating layers of each calorimeter module are used as a preshower detector (PSD). To achieve a separate readout of these layers two WLS fibers are embedded instead of one in the σ -groove of each tile. This additional pair of fibers from the two layers illuminate a single pixel of a multi-anode PMT. A total of 300 16-pixel multi-anode PMTs are used to provide the 4800 tower preshower signals.

The preshower detector was fully instrumented and read out only in 2006 so that it could not be used in the present analysis.

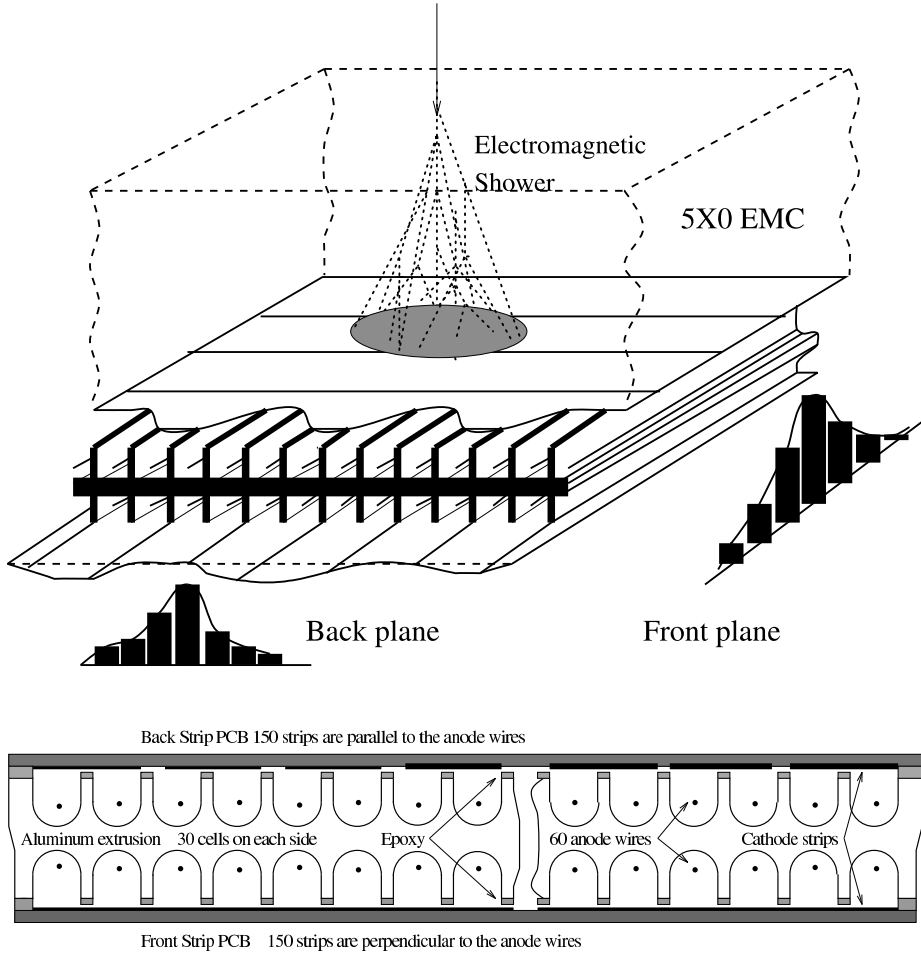


Figure 3.5: Schematic illustration of the SMD showing in the top figure a three dimensional view of the extruded aluminium profile containing the anode wires and the two read-out pad planes running parallel and perpendicular to the wires. The profile of a BEMC shower as recorded in the two SMD pad planes is shown by the histograms. The bottom plot shows a transverse view of the aluminium extrusion, the anode wires and the pad planes. Figure taken from [45].

3.5 BEMC electronics

The calorimeter is a “fast” detector in STAR so that its ADCs can be read out on each RHIC bunch crossing. The calorimeter data is also used in the STAR level-0 trigger, in the form of the “High Tower” and “Patch Sum” trigger primitives.

The level-0 HighTower trigger used in this analysis is a requirement that the energy deposited in any single calorimeter cell in the event exceeds a given threshold. This allows to enhance the statistics at the high energy part of the spectrum.

The complete description of the BEMC electronics operation is given in Appendix A.

Chapter 4

Event reconstruction in STAR

4.1 Data acquisition and trigger

The STAR data acquisition system (DAQ) [54] receives the input from multiple detectors at different readout rates. The typical recorded event rate of 100 Hz is limited by the drift time in the TPC (the slowest detector in STAR). The total event size can reach up to 200 MB in Au + Au collisions. STAR takes data in runs of about half an hour duration, each having $50\text{--}100 \times 10^3$ events.

The STAR trigger [55] is a pipelined system, capable to cope with the RHIC beam crossing frequency of 10 MHz. The trigger processes information from fast detectors, such as the ZDC, BBC, CTB or BEMC, and decides if the event should be read out and saved to tape. Each event is categorized by multiple trigger criteria and the events selected by different branches of the decision tree are written to tape sharing the available 100 Hz DAQ bandwidth.

The datasets used in the present analysis are taken in the $d + \text{Au}$ run of 2003 and the $p + p$ run of 2005, see also Table 2.1. The following trigger conditions had to be satisfied:

Minimum bias (MinBias) trigger in $d + \text{Au}$ collisions This condition required the presence of at least one neutron signal in the ZDC in the gold beam direction. As given in [15], this trigger condition captured $95 \pm 3\%$ of the total $d + \text{Au}$ geometric cross section of $\sigma_{\text{hadr}}^{d+\text{Au}} = 2.21 \pm 0.09 \text{ b}$.

Table 4.1: HighTower trigger thresholds used in $d + \text{Au}$ 2003 and $p + p$ 2005 data runs.

Dataset	HighTower-1 threshold [GeV]	HighTower-2 threshold [GeV]
$d + \text{Au}$ 2003	2.5	4.5
$p + p$ 2005	2.6	3.5

MinBias trigger in $p + p$ collisions This condition required the coincidence of signals from two BBC tiles on the opposite sides of the interaction point. Due to the dual-arm configuration this trigger is sensitive to the non-singly diffractive (NSD) cross section, which is a sum of the non-diffractive and doubly diffractive cross section. The total inelastic cross section is a sum of the NSD and singly diffractive cross section.

A minimum bias cross section of $\sigma_{\text{BBC}} = 26.1 \pm 0.2_{\text{syst}} \pm 1.8_{\text{stat}}$ mb was independently measured via Vernier scans in dedicated accelerator runs [56]. This trigger captured $87 \pm 8\%$ of the $p + p$ non-singly diffractive (NSD) cross section, as was determined from the detailed simulation of the BBC acceptance [17]. Correcting the BBC cross section for the acceptance we obtain a value for the NSD cross section of $\sigma_{\text{NSD}}^{p+p} = 30.0 \pm 3.5$ mb.

HighTower trigger This condition required, in addition to the MinBias, an energy deposit above a predefined threshold in at least one calorimeter tower. Two different thresholds were applied giving the HighTower-1 and HighTower-2 datasets. The values of these thresholds for the different runs are shown in Table 4.1. The purpose of this trigger is to enrich the sample with events that have a large transverse energy deposit.

4.2 STAR reconstruction chain

The events recorded on tape are passed through the standard STAR reconstruction chain. This reconstruction is performed routinely on the RHIC Computing Facility (RCF) which is a large computing farm located at BNL.

The most important part of the data reconstruction at this stage is tracking in the TPC and FTPCs. Charged tracks are reconstructed in the main TPC using a Kalman filter [57] and in the FTPCs using a conformal mapping

method [58]. The primary vertex is found by extrapolating and intersecting all reconstructed tracks. The vertex resolution in z is between 0.9 mm and 0.35 mm depending on the track multiplicity whereas in the transverse plane it is about 0.5 mm. Once the vertex has been found all tracks that approach to it closer than 3 cm are re-fitted to include the vertex position as the origin. Although the wire chambers are sensitive to almost 100% of the drifting electrons, the overall tracking efficiency is only 80–90% due to fiducial cuts, track merging, bad pads and dead channels. The momentum resolution of tracks decreases linearly with p_T from 2% for 300 MeV/ c pions to 7% for 4 GeV/ c pions.

Because the BEMC reconstruction was not yet available in the standard STAR reconstruction, the raw BEMC data were passed to the physics analysis. The tower ADC data could be directly passed because they only take a small fraction of the event size. The SMD strip ADC were zero-suppressed and then also passed to the analysis. This scheme implies that removal of malfunctioning elements and a full calibration of the BEMC is performed as a part of the physics analysis. This has the advantages that the reconstructed electron tracks in the TPC can be used to calibrate the energy response of the BEMC, and that the successive improvements in the BEMC calibration do not require re-generating the full dataset from the raw events on tape.

All data reconstruction and analysis in STAR is performed using the ROOT framework [59]. The processing of a full dataset such as $p + p$ or $d + \text{Au}$ takes about three months.

4.3 BEMC status tables

A quality assurance (QA) procedure for the BEMC is routinely performed before the physics analysis in order to remove malfunctioning detector components from the data and to correctly reproduce the time dependence of the detector acceptance in the Monte Carlo simulation. This QA procedure results in timestamped status tables which are used as an input to the physics analysis. Below we describe the QA procedure performed for the BEMC towers, a similar procedure is applied to the SMD strips.

For each run, the raw ADC spectra of all towers were accumulated and a number of criteria were applied to recognize common failure modes like the malfunctioning of entire readout boards and crates. A typical ADC spectrum of a tower is displayed in Figure 4.1 and shows the signal distribution and the accumulation of ADC counts in absence of a signal (pedestal). The position of these pedestals provide the zero offset of the ADC measurement and are,

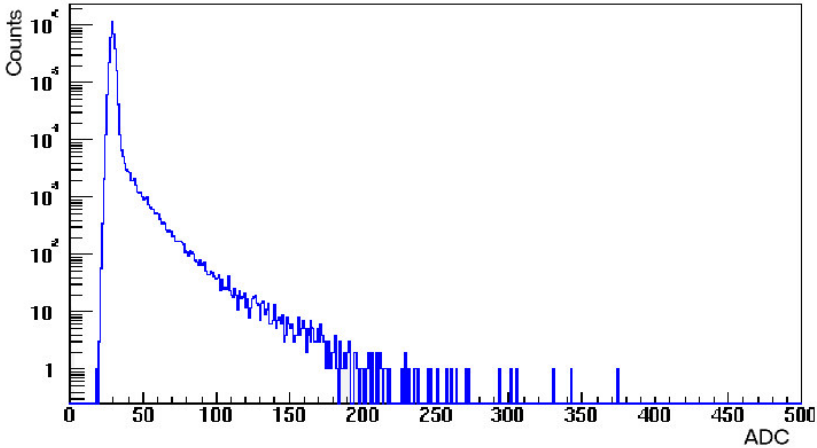


Figure 4.1: ADC spectrum of a BEMC tower showing a pedestal located at 30 ADC counts.

together with the width, stored in time dependent tables for each tower. Channels with anomalous pedestal positions and widths are flagged as bad. The signal fraction was defined as the number of ADC counts which are more than six standard deviations above the pedestal. Towers with a signal fraction smaller than 0.001 are flagged as “cold” or “dead” while those with a fraction above 0.1 are marked as “hot” or “noisy” (the exact numbers are multiplicity dependent and are adjusted for each collision system). Saved are, as function of run number, the position of the pedestals, their widths and flags indicating the status of each tower. The average fraction of good towers was found to be about 90% in the 2003 $d + \text{Au}$ run, with run-to-run fluctuations of about 2–5%. In the 2005 $p + p$ data the fraction of good towers was found to be about 97%.

In the BEMC reconstruction performed in this analysis the status tables were read in and used for pedestal subtraction of the ADC signals and removal of towers which were flagged as bad.

4.4 BEMC energy calibration

The purpose of the energy calibration is to establish the relation between ADC counts and the energy scale in GeV. The calibration proceeds in two stages.

First, a relative calibration matches the gains of individual towers to achieve an overall uniform response of the detector. A common scale between ADC counts and energy is then determined in a second absolute calibration step. The relative tower-by-tower calibration is done using minimum ionizing particles (MIP) while the absolute energy scale is determined from energy measurements of identified electrons in the TPC.

4.4.1 MIP calibration

A significant fraction (30–40%) of high energy charged hadrons traversing the BEMC only deposit a small amount of energy in the towers, equivalent to a 250–350 MeV electron, largely due to ionization energy loss (minimum ionizing particles). The signal from these particles is usually well separated from the tower pedestals.

To identify MIP particles, TPC tracks of sufficiently large momentum above 1.2 GeV/c are extrapolated to the BEMC and the response spectra are accumulated provided that the track extrapolation is contained within one tower and that there are no other tracks found in a 3×3 patch around this tower. In Figure 4.2 is shown a tower ADC spectrum collected from the $d + \text{Au}$ dataset which clearly shows the position of the MIP peak superimposed on a broad

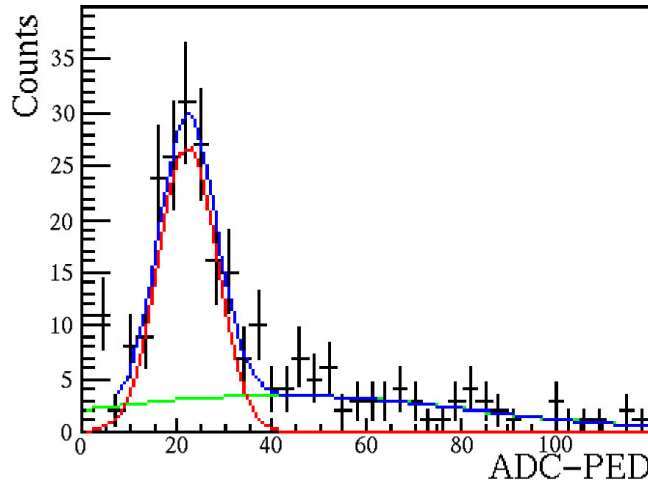


Figure 4.2: The BEMC tower response to MIP tracks. The curves indicate a fit to two Gaussians, one for the peak and one for the background. Figure taken from [60].

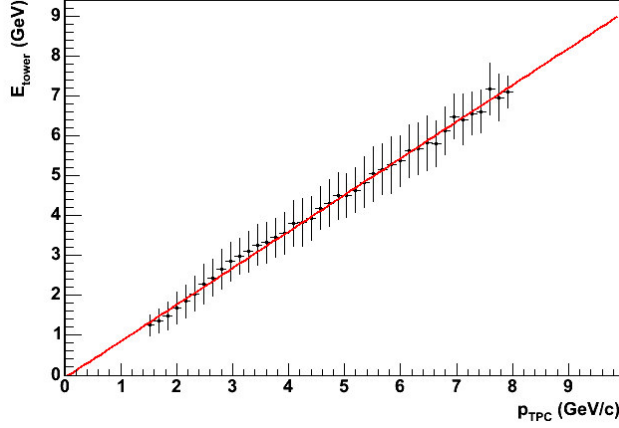


Figure 4.3: Electron energy measured in BEMC vs. momentum measured in TPC. The first order polynomial fit determines the global calibration constant. Figure taken from [60].

background [60]. The position of the fitted Gaussian is calculated for each tower and used to calculate the tower-by-tower gain corrections needed to equalize the detector.

The disadvantage of this method is that the calibration is performed at the low end of the scale where the signal is more susceptible to noise and where the lack of lever arm does not allow to detect possible non-linearities in the detector response.

4.4.2 Electron calibration

Because the electron momentum can be independently measured in the TPC it is possible to calibrate the absolute energy scale of the calorimeter using the simple relation for the ultra-relativistic electrons: $E/p = 1$.

Figure 4.3 shows the electron energy measured in the calorimeter versus its momentum measured in the TPC [60]. The calorimeter response is quite linear up to 8 GeV and the global gain correction obtained from the linear fit is applied to all towers.

This method takes advantage of the well understood TPC detector for the precise measurement of the electron track momentum in a wide range. However it requires high statistics to calibrate the high energy part of the spectrum so that only one global calibration constant for the calorimeter is obtained at

present. The systematic year-to-year uncertainty on the electron calibration was estimated to be 5% [61].

It has been found that the current calibration is less reliable at the edges of the calorimeter half-barrel, therefore the tower signals from the two η -rings at each side are later removed from this analysis (see Section 5.2).

This combination of the MIP-based equalization and electron-based absolute calibration is applied to the data after each running period, starting from 2003 $d + \text{Au}$ run. The run dependent calibration constants are saved in the STAR database and automatically applied to the ADC readout in the software.

4.5 Event selection

The event selection starts with rejecting events where subdetectors needed for this analysis were not operational or malfunctioning. In the following subsections we will describe several additional selection criteria in detail.

4.5.1 Beam background rejection

In $d + \text{Au}$ events, interactions of gold beam particles with material approximately 40 m upstream from the interaction region give rise to charged tracks that traverse the detector almost parallel to the beam direction. To identify events containing such background tracks the ratio

$$r = \frac{E_{\text{BEMC}}}{E_{\text{BEMC}} + E_{\text{TPC}}}$$

is calculated, where E_{BEMC} is the total energy recorded in the BEMC and E_{TPC} is the energy of all charged tracks reconstructed in TPC. In events containing background tracks the ratio r tends to become large because the background tracks give a large energy deposit in a calorimeter without being reconstructed in the TPC since they do not point to the vertex. This is shown in Figure 4.4 where the distribution of r is plotted for the $d + \text{Au}$ and $p + p$ datasets. The peak near unity in the left-hand plot indicates the presence of beam halo in $d + \text{Au}$ collisions and events with $r > 0.8$ are removed from the $d + \text{Au}$ analysis. This cut rejected 3.4% of MinBias and 13% of HighTower-2 triggered events. From a polynomial fit to the $d + \text{Au}$ distribution in the region $r = 0.6\text{--}0.8$ (curve in Figure 4.4) the false rejection rate was estimated to be 3.6% in the $d + \text{Au}$ HighTower-2 data and less than 1% in the other datasets.

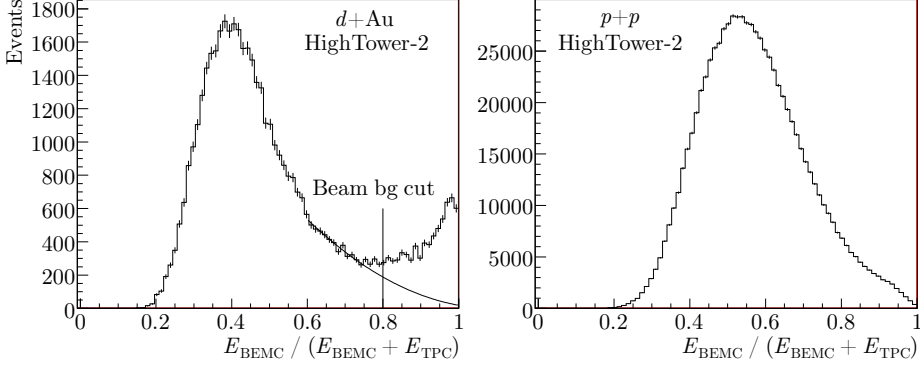


Figure 4.4: Distribution of $r = E_{\text{BEMC}} / (E_{\text{BEMC}} + E_{\text{TPC}})$ which shows beam background at $r > 0.8$ in $d + \text{Au}$ events (left) and its absence in $p + p$ events (right). The curve in the left hand plot indicates a polynomial fit used to estimate the false rejection rate in the $d + \text{Au}$ data.

The cut was not applied for the $p + p$ data since here the beam background is almost absent as can be seen in the right-hand plot of Figure 4.4.

During the summer in 2006 additional shielding walls were installed in STAR to reduce this beam background to a negligible level.

4.5.2 Vertex reconstruction

The event vertex is reconstructed to an accuracy of better than a millimeter in the z direction from the tracks reconstructed in the TPC. The distribution of the vertex z coordinate in the $p + p$ MinBias data is shown in Figure 4.5.

Events with $|z_{\text{vertex}}| > 60 \text{ cm}$ were rejected in the analysis, as indicated by the vertical lines in Figure 4.5. This cut is applied because the amount of material traversed by a particle increases dramatically at large values of $|z_{\text{vertex}}|$. As a consequence, the TPC tracking efficiency drops for vertices located far from the center of the detector.

In the HighTower trigger data the track multiplicity is almost always sufficient for a TPC vertex reconstruction but this is not so in the $p + p$ and $d + \text{Au}$ minimum bias data. Since the $p + p$ minimum bias trigger is based on coincidences in the BBC we can use the timing information of the BBC to reconstruct a vertex for every event even when the TPC vertex reconstruction failed (about 35% of the minimum bias events). The timing information from the BBC was calibrated against the z vertex coordinate reconstructed in the TPC as illus-

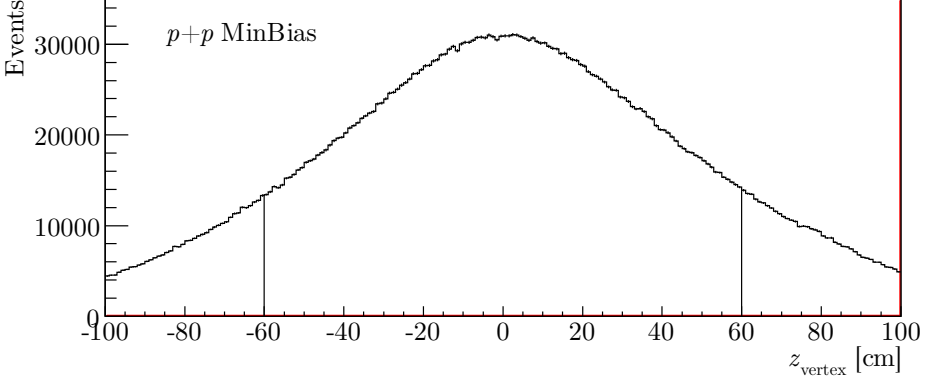


Figure 4.5: Vertex distribution in the $p + p$ MinBias dataset. Vertical lines indicate the cut used in the analysis.

trated in Figure 4.6 (top) where we show the correlation between the BBC time difference Δt and z_{vertex} in the TPC. The straight line in the plot corresponds to a linear fit

$$z_{\text{vertex}} = a\Delta t + b$$

yielding $a = 2.824 \pm 0.003$ cm per ADC count and $b = 11.00 \pm 0.02$ cm. In the bottom plot of Figure 4.6 we show the distribution of $z_{\text{BBC}} - z_{\text{TPC}}$, together with a Gaussian fit. From this fit we obtain the BBC vertex resolution of 40 cm.

Whereas $p + p$ events without a TPC vertex can be recovered by using the BBC timing information this cannot be done for $d + \text{Au}$ events because the BBC is not in the trigger and timing information may be absent. Since the π^0 reconstruction requires the presence of vertex the $d + \text{Au}$ events without a TPC vertex are removed from the analysis. The vertex finding efficiency was determined from detailed Monte Carlo simulation of the full $d + \text{Au}$ events and was found to be 93 ± 1 % in the ± 60 cm window [15]. This result is used to correct the $d + \text{Au}$ data for vertex inefficiencies, as will be explained in Section 7.1.

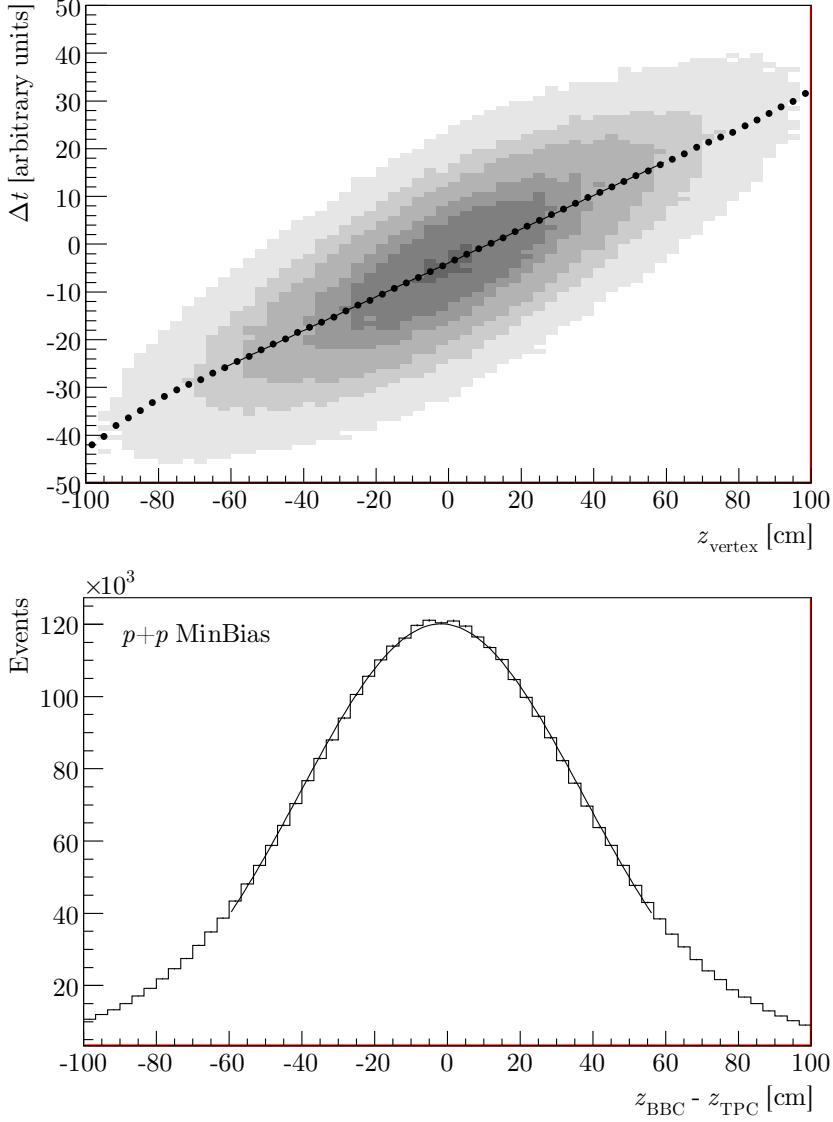


Figure 4.6: The correlation between the BBC time difference and z_{vertex} (top). Dots represent the positions of a fitted Gaussian in each vertical slice. The straight line indicates a linear fit used to calibrate the BBC readings. The distribution of $z_{\text{BBC}} - z_{\text{TPC}}$ and a Gaussian fit (bottom).

4.5.3 HighTower trigger condition

The HighTower-triggered data are filtered using a software implementation of the HighTower trigger. In this filter, the highest tower ADC value found in the event is required to exceed the same HighTower-1 (HighTower-2) threshold as the one that was used during the run. This filter is needed to remove events that were falsely triggered due to the presence of noisy channels (hot towers). Such channels are identified offline in a separate analysis and recorded in a database as described Section 4.3. This software filter also serves to make the trigger efficiency for Monte Carlo and real data as close as possible.

4.6 Centrality selection in $d + \text{Au}$ data

To measure the centrality in $d + \text{Au}$ collisions we use the correlation between the impact parameter of the collision and the charged track multiplicity in the forward direction. This correlation was established from a Monte Carlo Glauber simulation [19, 62] using, as an input, the Woods-Saxon nuclear matter density for the gold ion [63] and the Hulthén wave function of the deuteron [64]. In this simulation, the inelastic cross section of an individual nucleon-nucleon collision was taken to be $\sigma_{\text{inel}}^{NN} = 42 \text{ mb}$. The produced particles were then propagated through a full GEANT simulation of the STAR detector and the charged track multiplicity was recorded, together with the number of nucleon-nucleon collisions simulated by the event generator.

For the event-by-event centrality determination we measured the multiplicity N_{FTPC} of tracks reconstructed in the FTPC-East acceptance (in the Au beam direction), following the centrality binning scheme used in other STAR publications [15, 65]. The following quality cuts were applied to the reconstructed tracks: (i) at least 6 hits are required on the track; (ii) $p_T < 3 \text{ GeV}/c$ to guarantee that the track is fully contained in the FTPC acceptance and (iii) distance of closest approach (DCA) to the vertex should be less than 3 cm. The multiplicity distributions obtained from the $d + \text{Au}$ dataset are shown in Figure 4.7 for the MinBias, HighTower-1 and HighTower-2 triggers.

Based on the measured multiplicity the events were separated into three centrality classes: 0–20% most central, 20–40% mid central and 40–100% most peripheral, as illustrated by the vertical lines in Figure 4.7.

Table 4.2 lists the N_{FTPC} ranges which defined the centrality classes, and the corresponding mean number of binary collisions $\langle N_{\text{coll}} \rangle$ in each class, obtained from the Glauber model. In the table are also listed the systematic uncertainties on $\langle N_{\text{coll}} \rangle$ which are estimated by varying the Glauber model parameters.

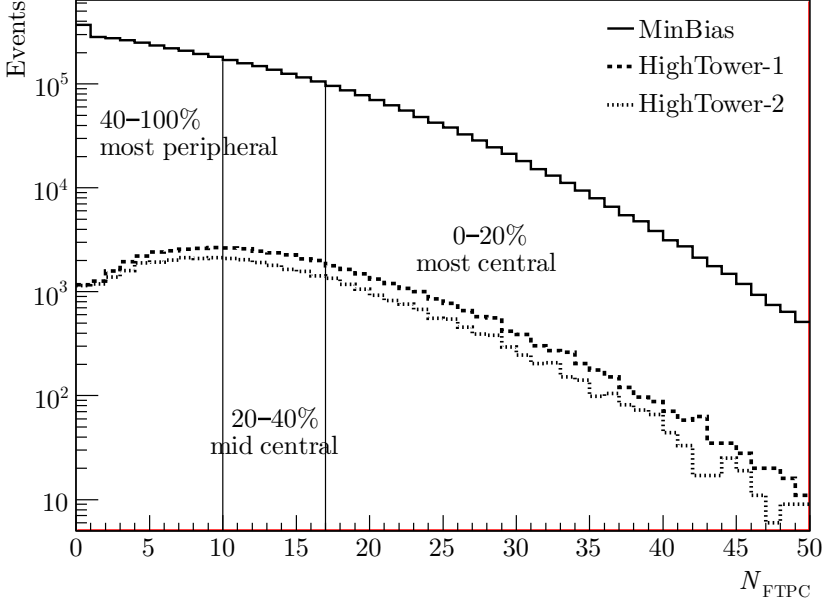


Figure 4.7: Centrality selection in $d + \text{Au}$ data, based on the FTPC multiplicity. Three centrality classes are defined, containing 0-20% most central, 20-40% mid central and 40-100% most peripheral events.

Table 4.2: Centrality classes defined for the $d + \text{Au}$ data and the corresponding $\langle N_{\text{coll}} \rangle$ values [65, 15]. The errors given for $\langle N_{\text{coll}} \rangle$ indicate the systematic uncertainty.

Centrality class	N_{FTPC} range	$\langle N_{\text{coll}} \rangle$
$d + \text{Au}$ minimum bias	—	7.5 ± 0.4
0-20% most central	< 10	15.0 ± 1.1
20-40% mid central	10-16	10.2 ± 1.0
40-100% most peripheral	≥ 17	4.0 ± 0.3
$p + p$	—	1

Chapter 5

Neutral meson reconstruction

The aim of this analysis is to measure π^0 and η production in $d + \text{Au}$ and $p + p$ collisions. The π^0 and η are identified by their decay

$$\pi^0 \rightarrow \gamma\gamma \quad \text{and} \quad \eta \rightarrow \gamma\gamma.$$

These decay modes have a branching ratio of 0.988 and 0.392, respectively [66]. The BEMC is used to detect the decay photons as will be described in the next sections. The lifetime of the π^0 is $\tau = 8.4 \times 10^{-17}$ s which corresponds to a decay length $c\tau = 0.025 \mu\text{m}$. The lifetime of the η is even shorter (7×10^{-19} s). Therefore we can assume that the decay photons originate from the primary vertex. For each event the invariant mass

$$M_{\gamma\gamma} = \sqrt{E_1 E_2 (1 - \cos \psi)} \quad (5.1)$$

is calculated for all pairs of photons detected in the BEMC. Here E_1 and E_2 are the energies of the decay photons and ψ is the opening angle between them, as measured in the laboratory system.

The reconstructed masses are accumulated in invariant mass spectra where the π^0 and the η show up as peaks around their nominal masses. These peaks are superimposed on a broad distribution of combinatorial background which originates from photon pairs that are not produced by the decay of a single parent particle.

In Table 5.1 we list the number of events in all datasets used in the analysis after the event selection procedures described in section 4.5 were applied.

Table 5.1: Statistics used in the analysis after the event selection.

Dataset	Number of events		
	MinBias	HighTower-1	HighTower-2
$d + \text{Au}$	164 608	53 154	40 974
0–20% most central	21 382	12 567	8 744
40–100% most peripheral	108 904	33 201	24 658
$p + p$	4 433 817	920 567	872 811

5.1 BEMC clustering

The first step in the invariant mass reconstruction is to find clusters of energy deposits in the calorimeter. The purpose of the cluster finding algorithm is to group adjacent hits that are likely to have originated from a single incident photon. The algorithm is applied to the BEMC tower and preshower signals as well as to the signals from each of the two SMD layers.

The clustering algorithm starts by accumulating a list of cluster seeds which contains all hits in a module with an energy deposit above a certain threshold E_{seed} . Starting from the most energetic seed in the list, an energy ordered list of module hits is searched for those adjacent to the present cluster. When such a hit is found, then, provided that it is above a second threshold E_{add} , it is added to the cluster and removed from the list. The clustering stops when either a pre-defined maximum cluster size N_{max} is reached or no more adjacent hits are found. The clustering algorithm then proceeds to process the next most energetic seed. At the end, clusters with total energy below the third threshold E_{min} are discarded. Note that, by construction, the clusters are confined within a module and cannot be shared by adjacent modules. However, the likelihood of cluster sharing between modules is considered to be low since the modules are physically separated by about 12 mm air gaps. In Table 5.2 we list the threshold values used in the clustering algorithm for all four detectors.

In Figure 5.1 we show the assignments made by the algorithm on several possible one-dimensional cluster topologies. Note that the rightmost hit pattern in this figure shows a double-peak structure which is splitted into two adjacent clusters by the algorithm. However, statistical fluctuations in single photon signals may also be the cause of a double-peak structure. In such a case, the cluster splitting by the algorithm becomes a source of background as will be discussed in Section 5.5.

The readout of the SMD η and ϕ planes is one-dimensional so that there

Table 5.2: Cluster finder threshold values used in the analysis.

Detector	E_{seed} [GeV]	E_{add} [GeV]	E_{min} [GeV]	N_{max}
Towers	0.35	0.035	0.02	4
Preshower	0.35	0.035	0.02	4
SMD- η	0.2	0.0005	0.1	5
SMD- ϕ	0.2	0.0005	0.1	5

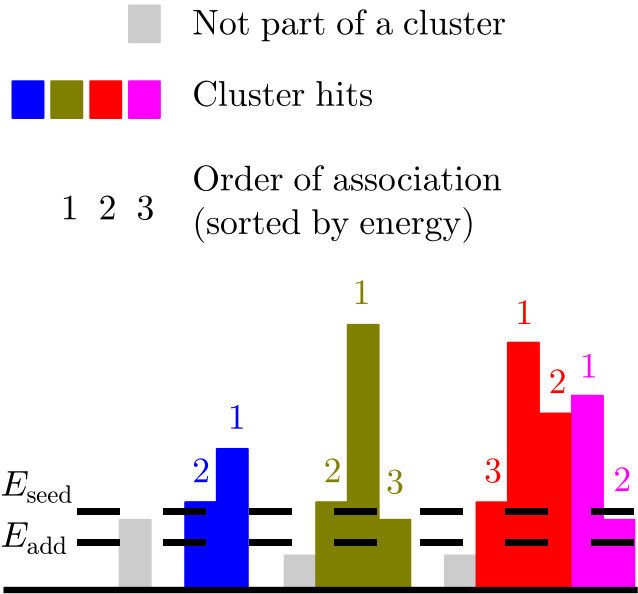


Figure 5.1: Schematic view of hit topologies in the BEMC and the assignment of hits to clusters by the algorithm described in the text.

is no ambiguity in what is considered to be an adjacent hit. The calorimeter tower readout is two-dimensional and two hits are considered to be adjacent when they share a side and not when they share only a corner.

The cluster position in the η and ϕ coordinates is calculated as the energy weighted mean position of the participating hits. In this calculation the geometrical center of the detector element is taken as the hit position.

After the tower, preshower and SMD clusters are found, the next step is to combine them into so-called BEMC points that should correspond as closely as possible to the impact point and energy deposit of a photon that traversed the calorimeter. This procedure treats 2×2 tower patches corresponding to the SMD- ϕ segmentation as shown by the top diagram in Figure 5.2.

It is required that every reconstructed BEMC point contains a tower cluster since the energy deposit of the incident particle is measured in the BEMC towers. Adding information from the SMD leads to a variety of combinations as shown schematically by the diagrams (a)–(c) in Figure 5.2. In the following paragraphs we describe how each case leads to the reconstruction of a BEMC point.

Tower, SMD- η and SMD- ϕ clusters The algorithm calculates for all combinations of SMD- η and SMD- ϕ clusters in a patch the energy asymmetry

$$\Delta = |E_\eta - E_\phi| / (E_\eta + E_\phi),$$

where E_η and E_ϕ are, respectively, the energy deposits measured in the SMD- η and SMD- ϕ planes.

The cluster assignment constitutes a well known problem in combinatorics (Assignment problem [67]) which we solve by a call to the CERN library routine **ASSNDX** [68] which combines objects into pairs in a way that minimizes the total cost. In the present algorithm the cost function is defined as energy asymmetry Δ between clusters.

Each associated SMD pair is matched to the tower cluster closest in η and ϕ . The total tower energy in a patch (including unassociated) is shared between points weighted by their average SMD energy, that is, each i -th pair will produce a point with energy

$$E_i = E_t^{\text{total}} \times \frac{E_{\text{SMD}, i}^{\text{assoc}}}{\sum_j E_{\text{SMD}, j}^{\text{assoc}}},$$

where $E_{\text{SMD}, i}^{\text{assoc}} = (E_{\eta, i} + E_{\phi, i})/2$. The η and ϕ coordinates are that of the SMD clusters.

This procedure works well, provided that the occupancies of the 2×2 tower patches are low. Indeed, the number of tower or SMD clusters reconstructed

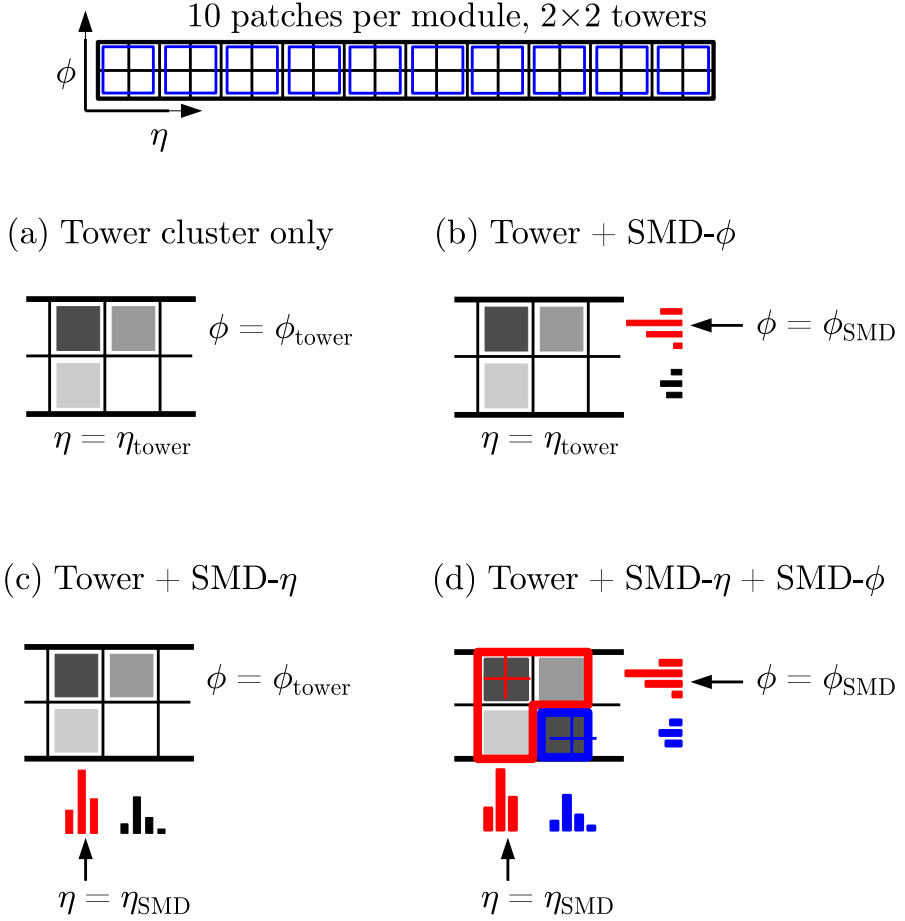


Figure 5.2: Combining tower and SMD clusters into BEMC points.

even in the most central $d + \text{Au}$ events is below 30 in the complete half-barrel, corresponding to a mean number of 12 clusters per event and an average occupancy of 2% per patch.

Tower and SMD- η clusters In this case the tower and SMD- η clusters are associated by the same algorithm as used above, except that here the cost function is defined by the energy asymmetry

$$\Delta = |E_t - E_\eta| / (E_t + E_\eta),$$

where E_t is the energy deposit in a tower and E_η is the energy deposit measured in the SMD- η plane. The total energy of tower clusters in a patch is shared between associated pairs weighted by their tower energy:

$$E_i = E_t^{\text{total}} \times \frac{E_{t,i}^{\text{assoc}}}{\sum_j E_{t,j}^{\text{assoc}}}.$$

The η coordinate associated to the BEMC point is taken directly from the SMD- η cluster while the ϕ coordinate is taken from the tower cluster.

Tower and SMD- ϕ clusters This case is treated as described above. The resulting BEMC points will have the ϕ coordinate from the SMD- ϕ clusters and the η coordinate from the tower clusters.

Tower clusters only If there are no SMD clusters in a patch that contains the tower cluster position, the energy and coordinates of the BEMC point are taken to be that of the tower cluster.

The relative occurrences of these four cases are approximately in proportion of 70 : 5 : 5 : 20 % for clusters with energy above 4 GeV, and 25 : 10 : 10 : 55 % at the lower energies.

The information about the shower shape in the SMD is in principle available but not used in the present clustering algorithm.

5.2 BEMC cluster cuts

After clustering only the BEMC points containing tower and both SMD- η and SMD- ϕ clusters were kept to be used in the further analysis of the HighTower-triggered data. In the analysis of MinBias data all reconstructed BEMC points

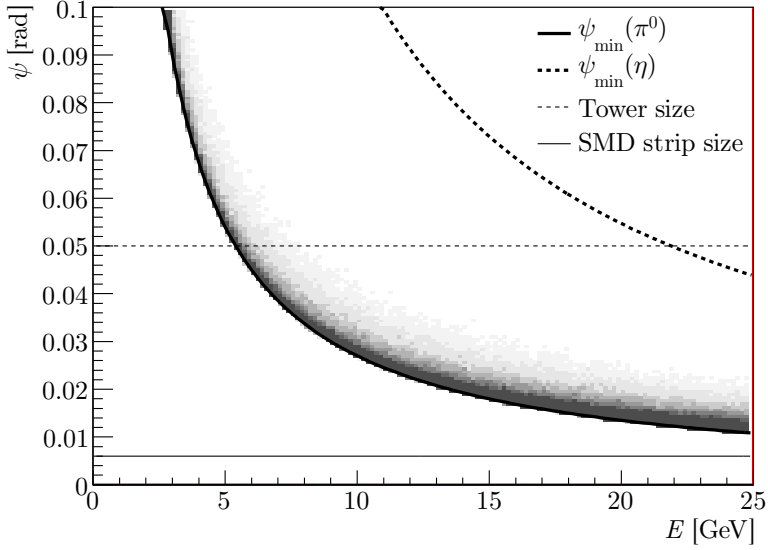


Figure 5.3: The minimal opening angle between π^0 and η decay photons compared to the tower and SMD strip size. Also shown is the actual distribution of the opening angles.

were used, even when they do not contain SMD clusters. From the decay kinematics in the laboratory it follows that the opening angle between the photons is smallest when these photons equally share the energy of the parent. In Figure 5.3 is shown this minimal opening angle versus the energy of the parent π^0 or η and compared to the tower and SMD strip size. It is seen that the spatial resolution of better than a calorimeter tower is needed to resolve the decay photons of neutral pions with momenta larger than 5 GeV/c. For this reason the SMD information is essential in this analysis.

It is seen from beam tests [53] that the SMD efficiency decreases rapidly with energy of the traversing particle and is smaller than 50% at $E < 2$ GeV/c. The energy resolution $\delta E/E = 12\% \oplus 86\%/\sqrt{E}$ is also poor at low energy, so that significant fluctuations in the strip readout are expected. Therefore, an SMD cluster is required to contain signals from at least two strips in order to be accepted in the HighTower-1 data. This cut rejects a large fraction of the distorted and falsely split SMD clusters, and reduces a possible effect of poor SMD response simulation at low energies.

It has been found that the tower calibration is less reliable at the edges of the calorimeter acceptance. For this reason we only keep the reconstructed clusters in the range $0.1 < \eta < 0.9$ for the further analysis, excluding two tower η -rings at each side of the calorimeter half barrel.

A charged particle veto (CPV) cut is applied to reject the charged hadrons that are detected in the calorimeter. These charged hadrons can be recognized as BEMC clusters with a pointing TPC track. The cluster was rejected if the distance D between the BEMC point and the closest TPC track was smaller than 0.04 in the η - ϕ coordinates:

$$D = \sqrt{\Delta\eta^2 + \Delta\phi^2} < 0.04.$$

The BEMC points remaining after this cut are considered to be photon candidates which are combined into pairs defining the set of π^0 candidates.

The asymmetry of the two-body decay of neutral mesons is defined as

$$\Delta = \frac{|E_1 - E_2|}{E_1 + E_2},$$

where E_1 and E_2 are the energies of the decay photons. From the decay kinematics it follows that this energy asymmetry is uniformly distributed between 0 and 1 [69]. In Figure 5.4 we show the distribution of the asymmetry of photon pairs reconstructed in $p + p$ data. In the MinBias data the distribution is not flat because of the acceptance effects — photons from the asymmetric decay have a large opening angle and there is a large probability that one of them escapes the barrel. It is also seen that the HighTower energy threshold biases the asymmetry to the higher values because it is easier for an asymmetric decay to pass the trigger. In this analysis the π^0 candidates were only accepted if the asymmetry was less than 0.7, in order to reject very asymmetric decays where one of the BEMC points has low energy, and to reject a significant part of the low mass background (this background will be described in the following sections). It turns out that the asymmetry cut improves the signal to background ratio by approximately a factor of 1.5.

Finally, for the HighTower-triggered data the requirement is made that at least one of the reconstructed decay photons alone satisfies this trigger. This requirement is made to guarantee that the trigger efficiency is the same in both real and simulated data, as was already mentioned in section 4.5.3.

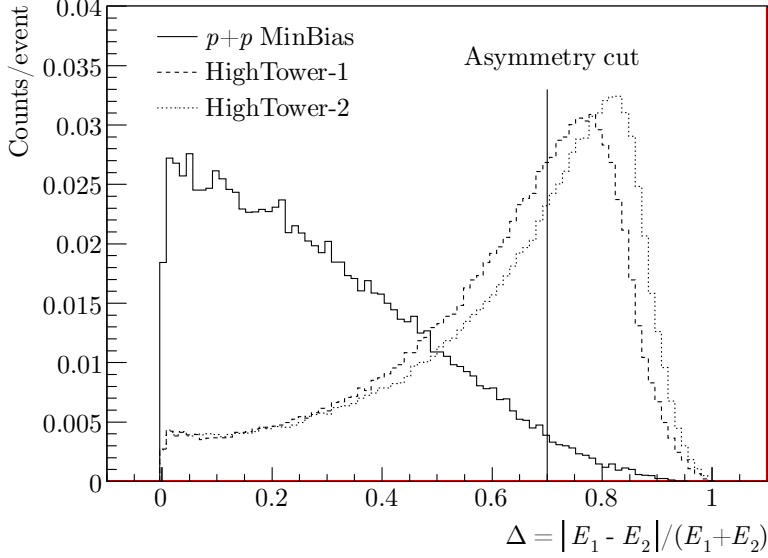


Figure 5.4: The energy asymmetry of the photon pairs reconstructed in $p + p$ data.

5.3 Invariant mass distribution

After cuts, the pairs of BEMC points are turned into 4-vectors by assuming that the decay photons originate from the reconstructed main vertex. For each π^0 candidate the pseudorapidity η , the azimuth ϕ , the transverse momentum p_T and the invariant mass $M_{\gamma\gamma}$ (Eq. 5.1) are calculated. In Figure 5.5 we show the η , ϕ , p_T and $M_{\gamma\gamma}$ distributions of the π^0 candidates in the $p + p$ dataset. For the $d + \text{Au}$ data these distributions look similar as those shown for $p + p$.

The η distribution shows the decrease of the calorimeter acceptance at the edges because there it is likely that one of the decay photons escapes the calorimeter. The asymmetry is due to the fact that the calorimeter half-barrel is positioned asymmetrically with respect to the interaction point. The structure seen in the ϕ distribution reflects the azimuthal dependence of the calorimeter acceptance caused by failing SMD modules.

In Figure 5.5(c) is shown the p_T distribution of the photon pairs separately for the MinBias and HighTower datasets. It is seen that the HighTower triggers significantly increase the rate of pion candidates at large p_T . The p_T -integrated

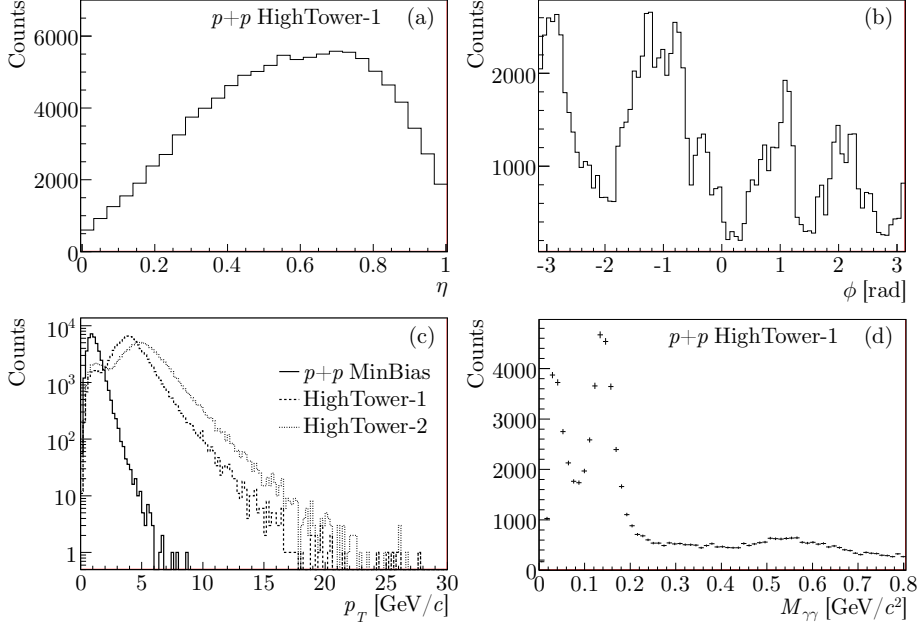


Figure 5.5: Distribution of π^0 candidates as a function of η and ϕ (top), p_T and $M_{\gamma\gamma}$ (bottom) obtained from the $p + p$ data.

invariant mass distribution in Figure 5.5(d) clearly shows the π^0 and η peaks superimposed on a broad background distribution. This background has a combinatorial and a low mass component. In the next two sections we will discuss each background component in detail.

5.4 Combinatorial background

The combinatorial background in the invariant mass distribution originates from pairs of photon clusters that are not produced in a single π^0 decay. To describe the shape of the combinatorial background we use the event mixing technique where photon clusters from two different events are combined. To mix only similar event topologies the data were subdivided into different mixing classes based on the vertex position, BEMC multiplicity and trigger type (MinBias, HighTower-1 and HighTower-2). In Figure 5.6 we show the $p + p$ vertex and

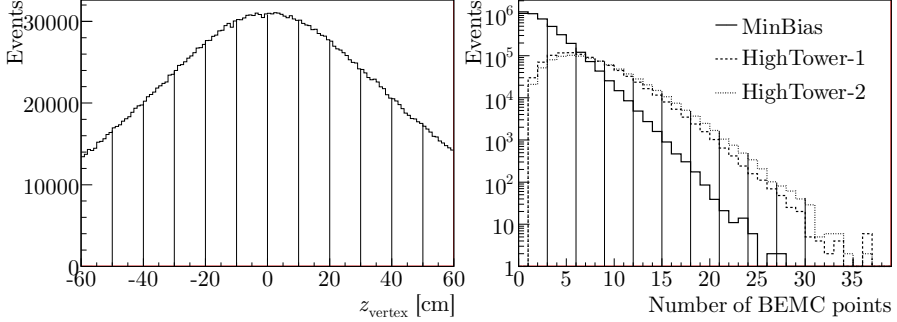


Figure 5.6: Distributions of the number of events as a function of vertex z (left) and number of BEMC points (right) obtained from the $p + p$ dataset. In both figures are shown the intervals used to define the event mixing classes.

multiplicity distributions and the bins defining the mixing classes.

Figure 5.7 shows an example of an invariant mass distribution in the $4 < p_T < 5$ GeV/ c bin, obtained from the HighTower-1 $p + p$ data, together with the combinatorial background obtained from the event mixing. The mixed event background distribution is normalized to the same-event distribution in the invariant mass region $0.9 < M_{\gamma\gamma} < 1.2$ GeV/ c^2 . In the bottom panel of this figure the background subtracted distribution is shown.

It can be seen that there is still some residual background in the interval $0.2 < M_{\gamma\gamma} < 0.4$ GeV/ c^2 which could be caused by the fact that the mixing procedure does not fully take into account the correlation structure of the event. For example, an important source of particle correlations is the jet structure which is not present in the sample of mixed events. In order to preserve jet-induced correlations the jet axes in both events are aligned before mixing, as described below.

To determine the (η, ϕ) position of the most energetic jet in every event, the standard STAR jet finding algorithm [70] was used. The mixed pion candidates were constructed by taking two photons from different events, where one of the events was displaced in η and ϕ by $\Delta\eta = \eta_2 - \eta_1$ and $\Delta\phi = \phi_2 - \phi_1$, respectively. Here $\eta_{1,2}$ and $\phi_{1,2}$ are the jet orientations in the two events.

In Figure 5.8 we show a schematic view of two superimposed events where the jet axes are aligned. In order to minimize acceptance distortions, the events were divided into mixing classes in the jet η coordinate. By mixing only events in the same class the shift $\Delta\eta$ was kept smaller than 0.1. Because the calorimeter

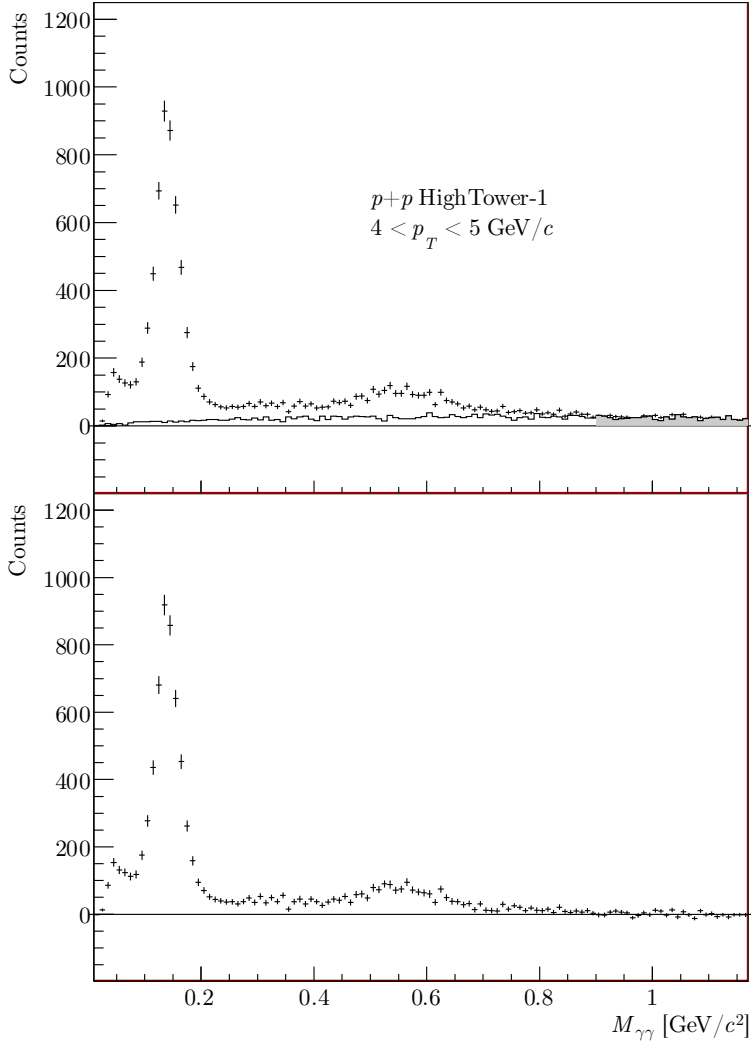


Figure 5.7: The same-event invariant mass distribution and the combinatorial background obtained from the random event mixing (top) and the background subtracted distribution (bottom). The shaded area in the top plot indicates the region where the mixed event background is normalized to the data.

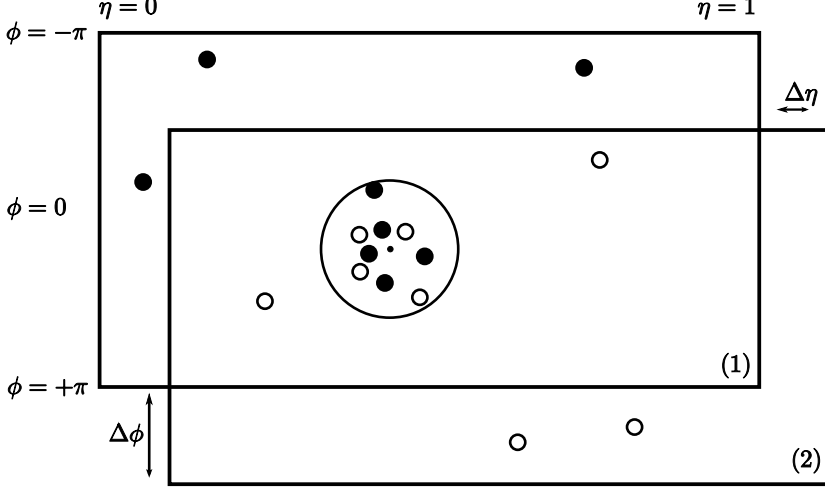


Figure 5.8: A schematic view of two superimposed events where the jet axes are aligned.

has a cylindrical shape, the shift in ϕ does not induce any significant acceptance distortion.

However, a side effect of this procedure is that correlations are induced if there is no real jet structure since the jet finding algorithm will then simply pick the most energetic track in the event. To reduce possible bias introduced by such correlations we assume that a jet structure is associated with large p_T pions but not with low p_T pions. The combinatorial background is then taken as a p_T -dependent linear combination of the distributions obtained by random mixing and jet-aligned mixing

$$B(M, p_T) = A(p_T) B_J(M, p_T) + (1 - A(p_T)) B_R(M, p_T).$$

Here $B_J(M, p_T)$ and $B_R(M, p_T)$ are the background spectra from, respectively, the jet-aligned and random event mixing in a given p_T bin. The interpolation coefficient $A(p_T)$ is given by

$$A(p_T) = \begin{cases} ap_T + b & \text{for } p_T < 10 \text{ GeV}/c \\ 1 & \text{otherwise,} \end{cases} \quad (5.2)$$

where the coefficients are $a = 0.097 \text{ (GeV}/c)^{-1}$ and $b = -0.117$. We assign a systematic uncertainty of 10% to A , which propagates into a systematic uncertainty of 5% on the π^0 and 1% on the η yields.

In Figure 5.9 we plot the same invariant mass spectrum as that shown in Figure 5.7 with the background estimated by the combined random and jet-aligned event mixing. The mixed event background is normalized to same-event distribution in the ranges $0.3 < M_{\gamma\gamma} < 0.4$ and $0.8 < M_{\gamma\gamma} < 1.6$ GeV/ c . By changing the subtracted background within the normalization uncertainty we obtained a systematic error on the π^0 and η yields. This error was found to increase with p_T from 0.5 to 3% for the π^0 and from 10 to 50% for the η yield.

In the bottom panel of Figure 5.9 the background subtracted spectrum is plotted which still shows a residual background component at low invariant mass. The origin of this background is described in the next section.

5.5 Low-mass background

In Figure 5.1 we have shown a double peaked hit pattern which will be reconstructed by the clustering algorithm as two separate adjacent clusters. However, it is possible that random fluctuations will accidentally generate such a two peak structure so that the clustering algorithm will incorrectly split the cluster. These random fluctuations enhance the yield of pairs with minimal angular separation and thus contribute to the lowest di-photon invariant mass region, as can be seen in Figure 5.9. However, at a given small opening angle the invariant mass increases with increasing energy of the photons so that the low mass background spectrum will extend to larger values of $M_{\gamma\gamma}$ with increasing p_T of the parent particle.

The shape of the low mass background was obtained from a simulation as follows. Single photons were generated with flat distributions in ϕ , $-0.2 < \eta < 1.2$ and $0 < p_T < 25$ GeV/ c . These photons were tracked through a detailed description of the STAR geometry with the GEANT program [71]. A detailed simulation of the electromagnetic shower development in the calorimeter was used to generate realistic signals in the towers and the SMD. The simulated signals were processed by the same reconstruction chain as the real data. Photons with more than one reconstructed cluster were observed and the invariant mass and p_T of such cluster pairs were calculated. The invariant masses were histogrammed with each entry weighted by the p_T spectrum of photons in the real data, corrected for the photon detection efficiency.

In the top plot of Figure 5.10 we show the low mass background distributions in three bins of the reconstructed pair p_T . It is seen that the distributions indeed move to larger invariant masses with increasing p_T and extend far into the pion window at large p_T . For this reason it is not possible to estimate this background

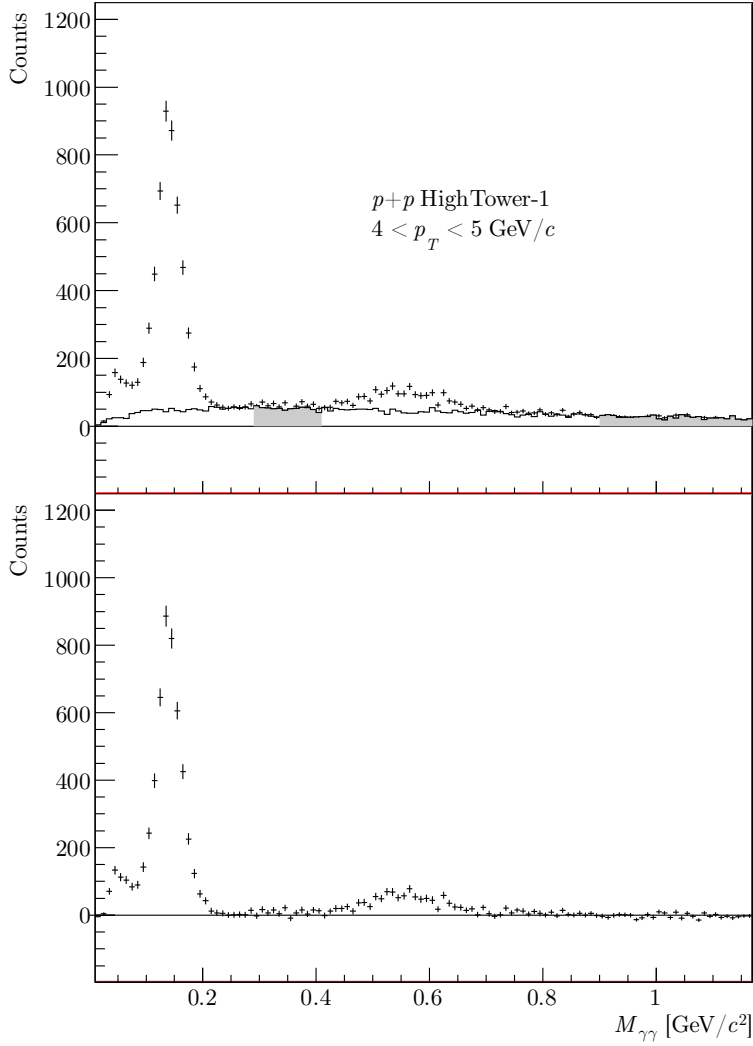


Figure 5.9: The same-event invariant mass distribution and the combinatorial background obtained from the jet-aligned event mixing (top) and the background subtracted distribution (bottom). The shaded regions in the top plot indicate where the mixed event background is normalized to the data.

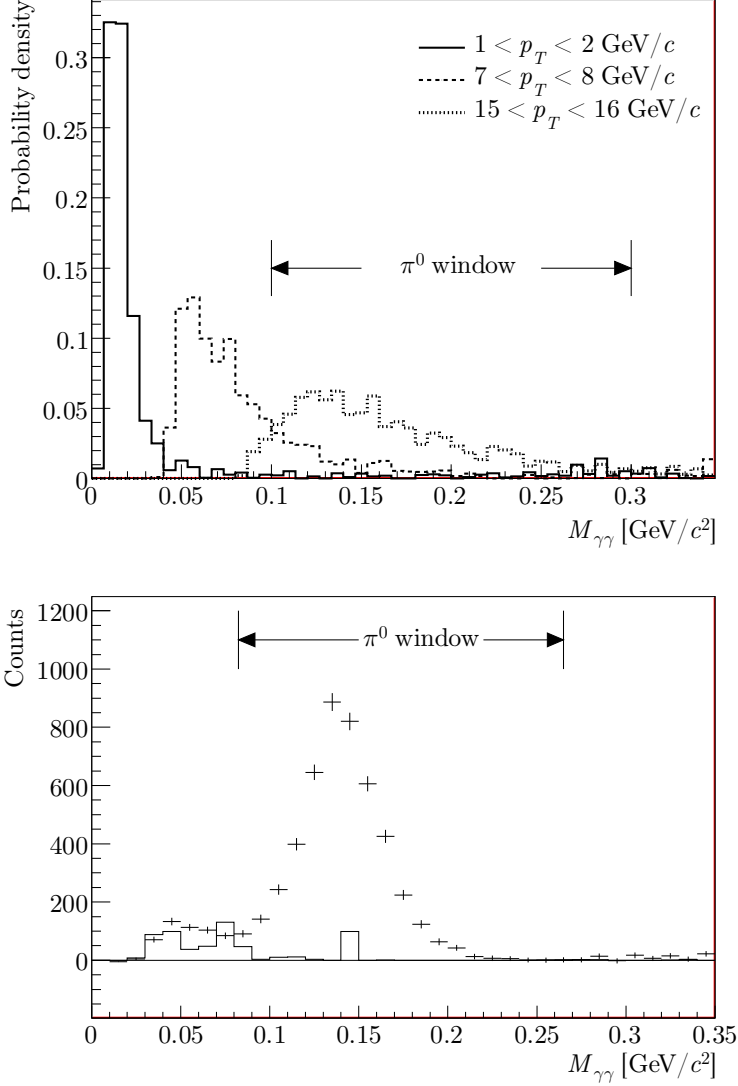


Figure 5.10: The low mass background distributions from erroneous splitting of single photons in three bins of the reconstructed pair p_T (top). The distributions extend to larger invariant masses with increasing p_T . The low mass background component in the invariant mass distribution obtained from $p + p$ data (bottom).

from a phenomenological fit to the data so that we have to rely on the Monte Carlo simulation to subtract the low mass background.

The second significant source of neutral clusters in the calorimeter are the neutral hadrons produced in the collision, mostly antineutrons. As a first attempt to account for the additional low mass background from these hadrons, simulations of antineutrons were performed in the same way as photons and the reconstructed invariant mass distribution was added according to the realistic proportion $\bar{n}/\gamma = \bar{n}/2\pi^0$. The ratio \bar{n}/π^0 was taken to be equal to the average value of \bar{p}/π^- from the STAR measurement [28] in the p_T range covered by each of MinBias and HighTower datasets. In the bottom plot of Figure 5.10 we compare the simulated low mass background (histogram) to the data.

In Figure 5.11 we show the invariant mass spectra and the low mass background component (top) together with the final background subtracted spectrum (bottom).

5.6 Yield extraction

The complete set of invariant mass spectra for all p_T bins, triggers and datasets are shown in Figures 5.12–5.17. For display purposes the spectra are normalized to the bin content in the π^0 peak. The shaded areas in the figures indicate the π^0 and η peak regions where the yields are calculated simply by adding-up the bin contents.

The left border of the π^0 peak region was taken to be a linear function of p_T , common for all datasets and triggers. It was adjusted in a way that most of the yield is captured while the low mass background and its associated uncertainty is avoided as much as possible. The right border also linearly increases with p_T in order to cover the asymmetric right tail of the peak. Similarly, the η peak region is a p_T -dependent window that captures most of the signal. For completeness we give below the parametrization of the π^0 and η windows:

$$\begin{aligned} 75 + 1.7p_T < M_{\pi^0} < 250 + 3.3p_T & \text{ MeV}/c^2, \\ 350 + 3.3p_T < M_{\eta} < 750 & \text{ MeV}/c^2. \end{aligned}$$

The stability of the yields was determined by varying the vertex position cut, the energy asymmetry cut and the yield integration window. From the observed variations, a point-to-point systematic error of 5% was assigned to the yields.

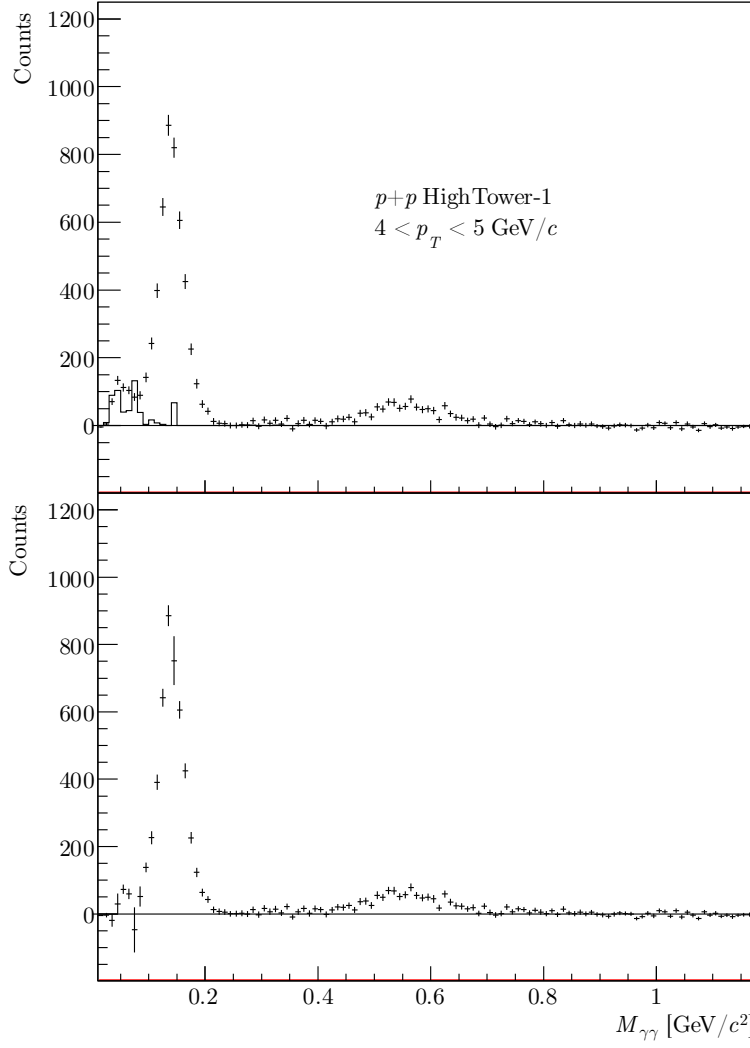


Figure 5.11: The invariant mass distribution before (top) and after the low mass background subtraction (bottom).

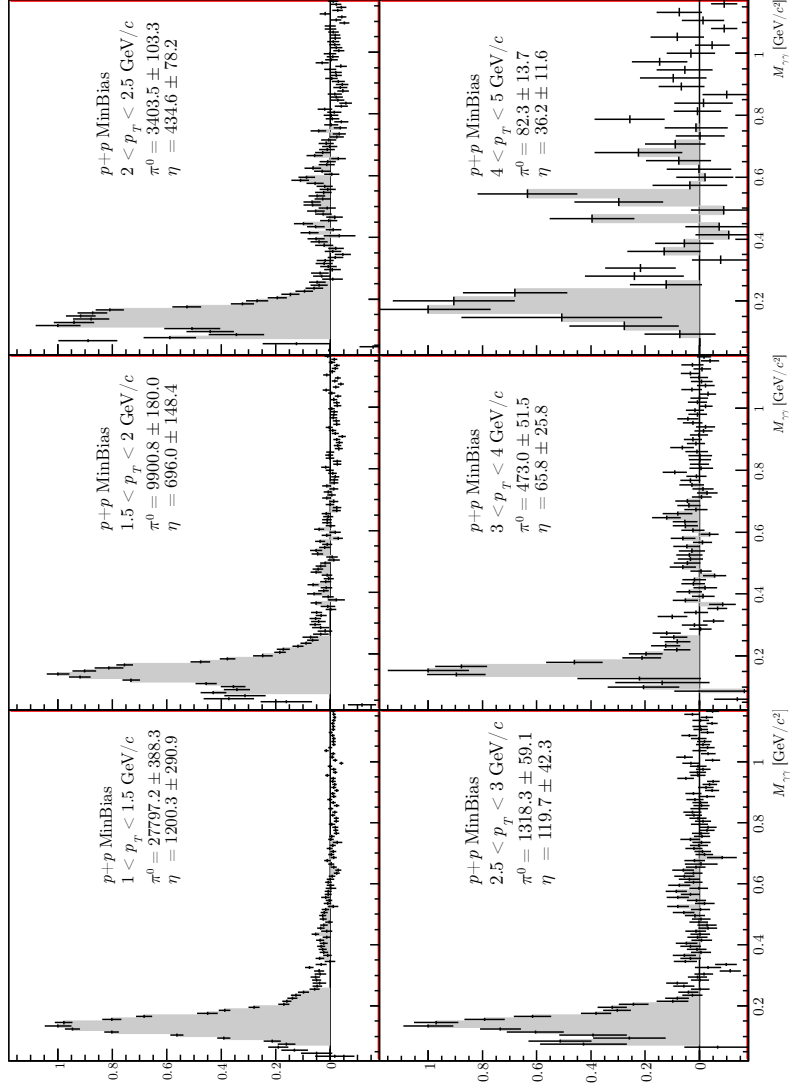


Figure 5.12: Invariant mass distributions in all p_T bins, $p + p$ MinBias data. The spectra are normalized to the bin content in the π^0 peak.

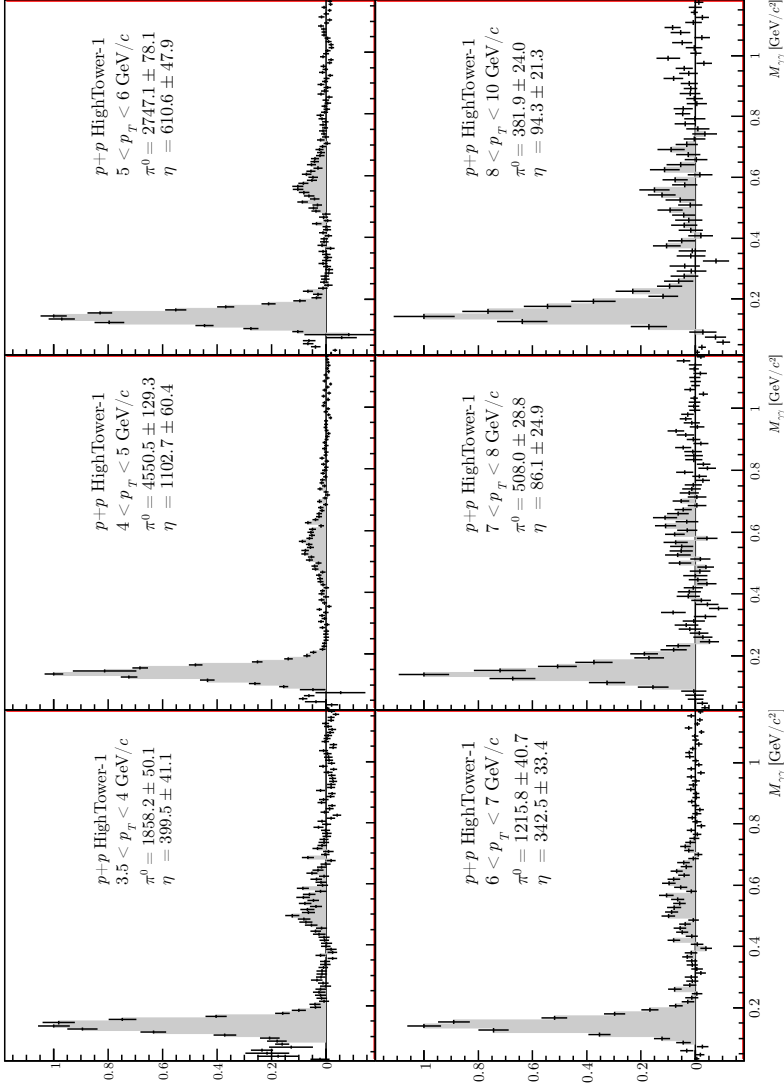


Figure 5.13: Invariant mass distributions in all p_T bins, $p + p$ HighTower-1 data. The spectra are normalized to the bin content in the π^0 peak.

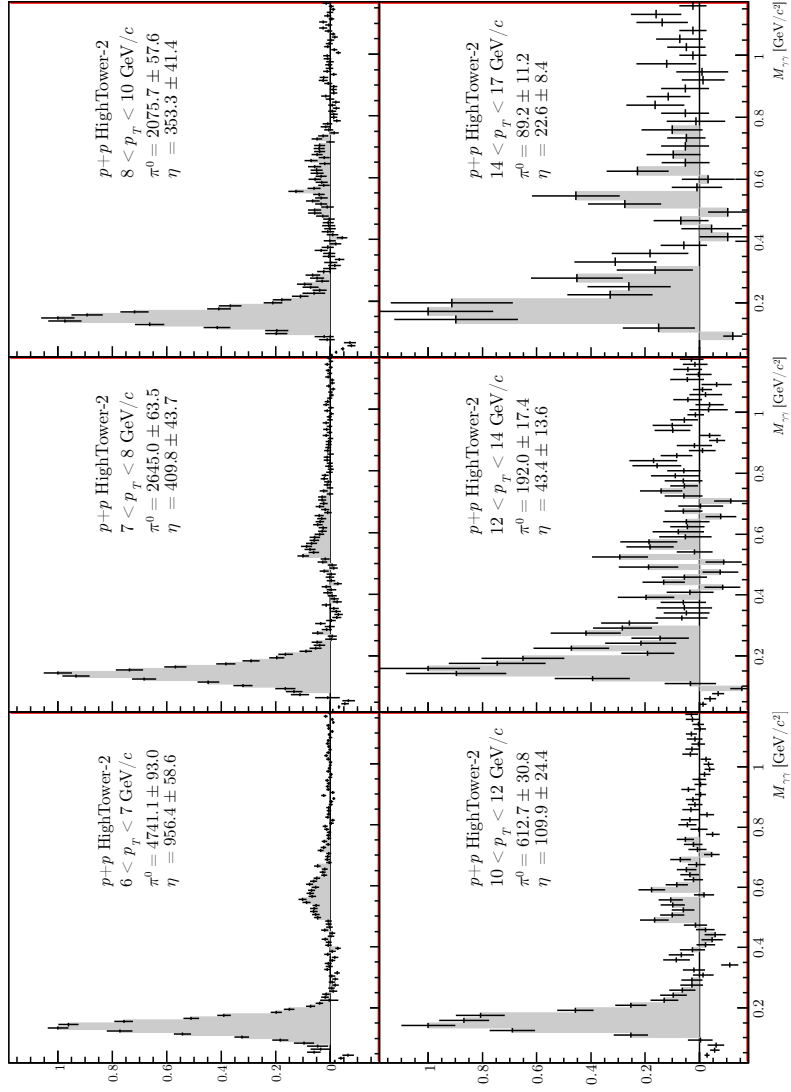


Figure 5.14: Invariant mass distributions in all p_T bins, $p + p$ HighTower-2 data. The spectra are normalized to the bin content in the π^0 peak.

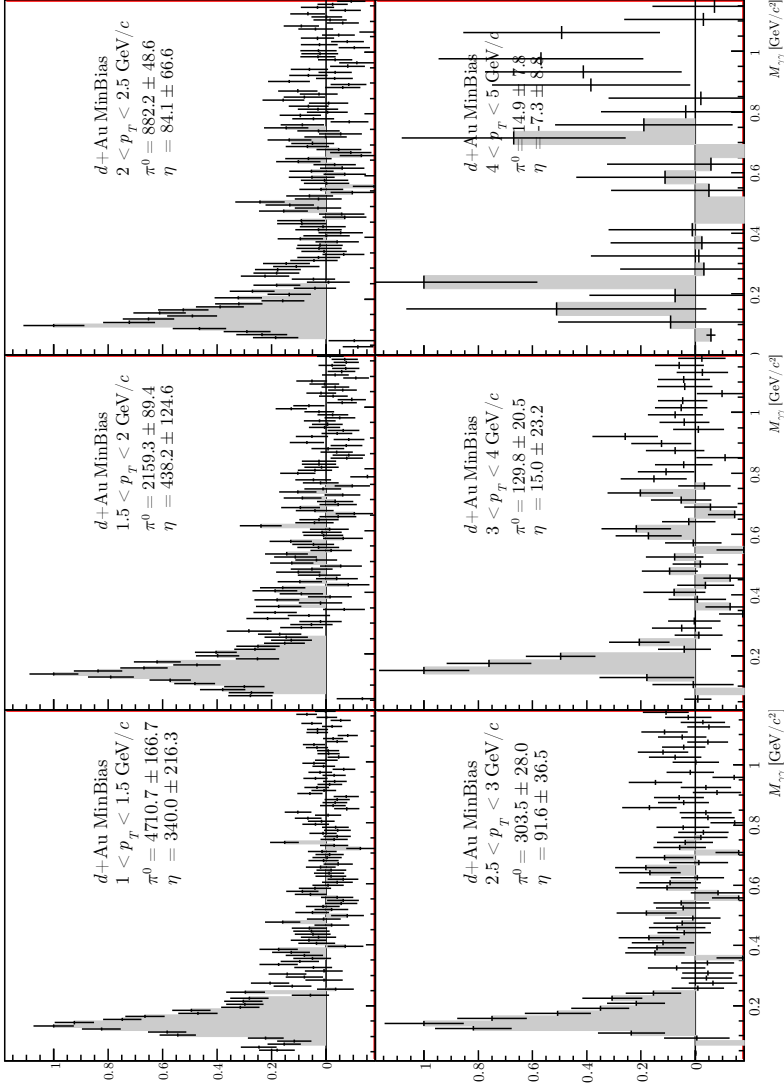


Figure 5.15: Invariant mass distributions in all p_T bins, $d + \text{Au}$ MinBias data. The spectra are normalized to the bin content in the π^0 peak.

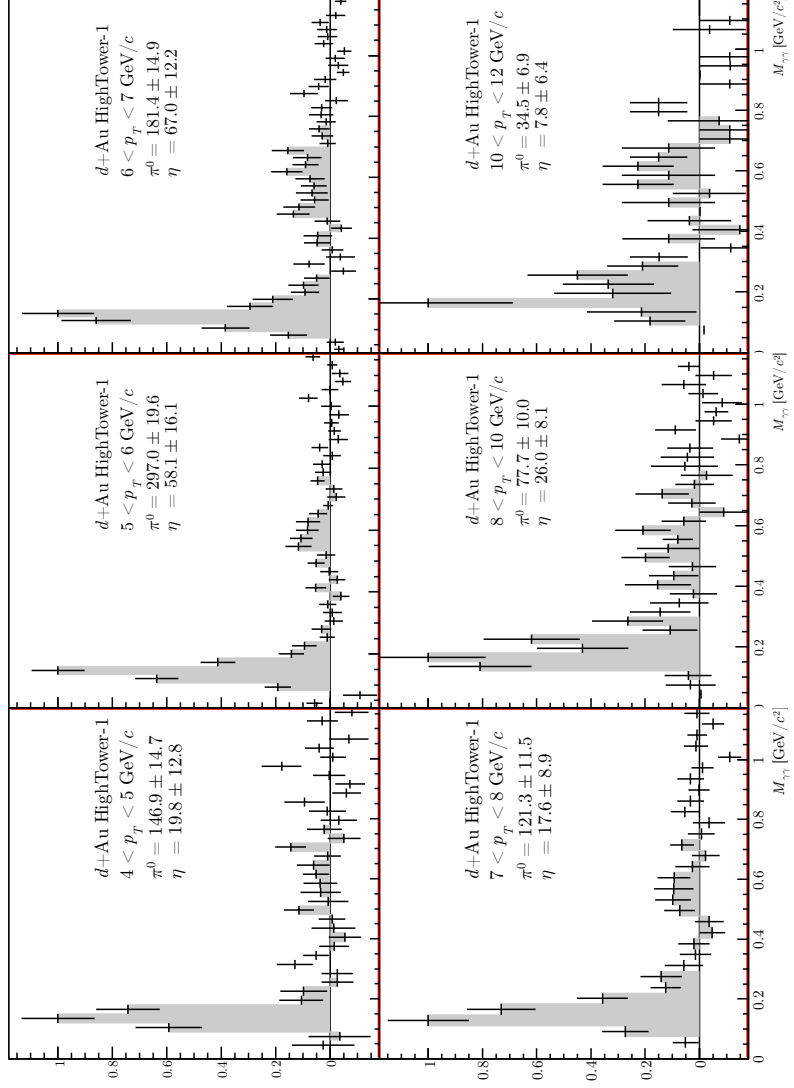


Figure 5.16: Invariant mass distributions in all p_T bins, $d+Au$ HighTower-1 data. The spectra are normalized to the bin content in the π^0 peak.

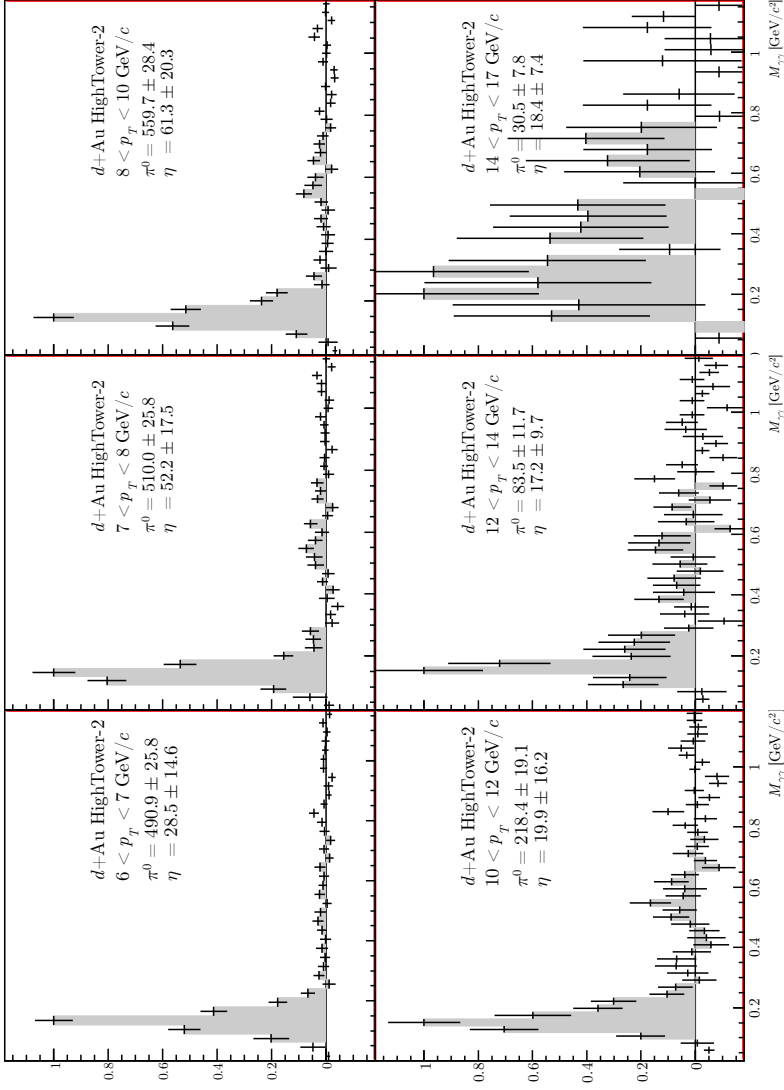


Figure 5.17: Invariant mass distributions in all p_T bins, $d+Au$ HighTower-2 data. The spectra are normalized to the bin content in the π^0 peak.

Chapter 6

Invariant yield calculation

The invariant yield of the neutral pions and η mesons per one minimum bias collision as a function of the transverse momentum p_T is given by

$$E \frac{d^3N}{d\mathbf{p}^3} = \frac{d^3N}{p_T dp_T dy d\phi} = \frac{d^2N}{2\pi p_T dp_T dy}, \quad (6.1)$$

where in the last equation isotropic production in azimuth is assumed. Using the experimentally measured quantities the invariant yield is calculated as

$$E \frac{d^3N}{d\mathbf{p}^3} = \frac{1}{2\pi p_T} \frac{\varepsilon_{\text{vertex}}}{N_{\text{trig}} K_{\text{trig}} (1 - \varepsilon_{\text{beam}})} \frac{\Delta Y}{\Delta p_T \Delta y} \frac{1}{\varepsilon_{\text{acc}}} \frac{1}{\varepsilon_{\text{cpv}}} \frac{1}{\Gamma_{\gamma\gamma}/\Gamma}, \quad (6.2)$$

where:

- ΔY is the raw yield measured in the bin $\Delta p_T \Delta y$;
- N_{trig} is the number of triggers recorded;
- K_{trig} is the trigger prescale factor which is unity for the MinBias events and larger than unity for the HighTower data. The product $N_{\text{trig}} K_{\text{trig}}$ then gives the equivalent number of minimum bias events that produced the yield ΔY ;
- $\varepsilon_{\text{vertex}}$ is the vertex finding efficiency in minimum bias events;
- $\varepsilon_{\text{beam}}$ is the beam background contamination in minimum bias events;
- Δp_T is the p_T bin for which the yield is calculated;

- Δy is the rapidity range of the measurements, in this analysis $\Delta y = 1$;
- ε_{acc} is the BEMC acceptance and efficiency correction factor;
- ε_{cpv} is a correction for random vetoes;
- $\Gamma_{\gamma\gamma}/\Gamma$ is the branching ratio of the di-photon decay channel, equal to 0.988 for π^0 and 0.392 for η [66].

Each of these corrections are described in detail in the following sections.

6.1 Acceptance and efficiency correction

To calculate the acceptance and efficiency correction factor ε_{acc} , a Monte Carlo simulation of the detector was used where neutral pions and their decay photons were tracked through the STAR detector geometry using GEANT [71]. The simulated signals were passed through the same analysis chain as the real data.

The pions were generated in the pseudorapidity region $-0.3 < \eta < +1.3$ which is sufficiently large to account for edge effects caused by the calorimeter acceptance limits of $0 < \eta < 1$, the azimuth was generated flat in $-\pi < \phi < +\pi$. The p_T distribution was taken to be flat between zero and 25 GeV/c which amply covers the measured pion p_T range of up to 17 GeV/c. The vertex distribution of the generated pions was taken to be Gaussian in z with a spread of $\sigma = 60$ cm and centered at $z = 0$.

The generated pions were allowed to decay into $\pi^0 \rightarrow \gamma\gamma$. The GEANT simulation accounts for all interaction of the decay photons with the detector, such as pair conversion into e^+e^- and showering in the calorimeter or in the material in front.

To reproduce a realistic energy resolution of the calorimeter, an additional smearing has to be applied to the energy deposit generated by GEANT in the towers. The effect of this can be seen in Figure 6.1 where the simulated π^0 invariant mass peak is shown in comparison to the $p + p$ data with and without smearing. An additional spread of 5% was used to reproduce the $p + p$ data and 10% for the $d + \text{Au}$ data.

To reproduce the p_T spectrum of pions in the data, each Monte Carlo event was weighted by a p_T -dependent function. Such weighting technique allows to sample the whole p_T range with good statistical power while, at the same time, the bin migration effect caused by the finite detector energy resolution is reproduced. A next-to-leading order QCD calculation [72] provided the initial weight

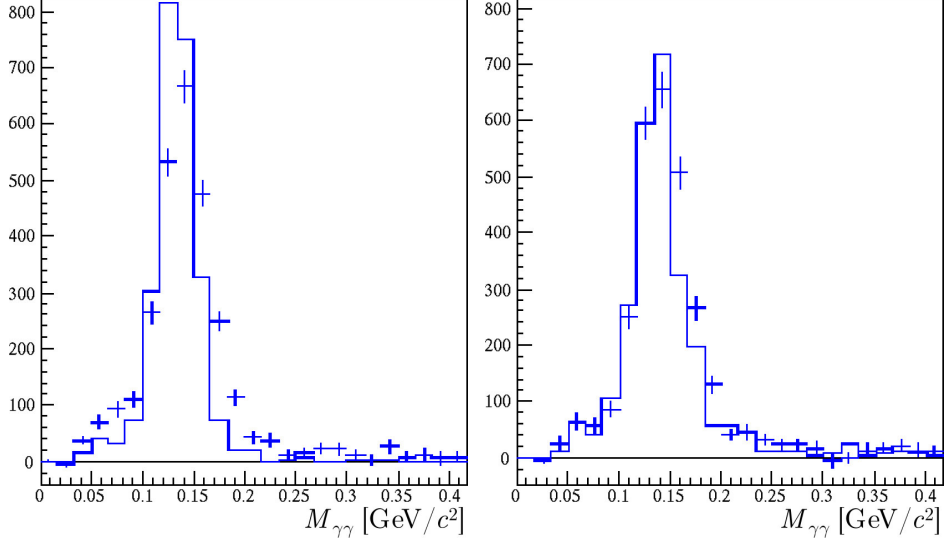


Figure 6.1: The invariant mass distribution in the real $p+p$ data (crosses) and in the simulation (histogram). The Monte Carlo produces a narrower π^0 peak (left) than is observed in the data so that an additional energy smearing was introduced to reproduce the calorimeter resolution (right).

function, parametrized as described in Section 7.1, which was subsequently adjusted in an iterative procedure.

As mentioned in Section 4.3, the time dependence of the calorimeter acceptance is stored in data tables which are fed into the analysis. In order to reproduce this time dependence in the Monte Carlo, the simulated events were assigned time stamps that follow the timeline of the real data taking. In Figure 6.2 is shown, separately for MinBias and HighTower data, the accumulated real data statistics per day (histogram) together with the time distribution of the simulated events (full circles). In this way, the geometrical calorimeter acceptance (fraction of good towers) was reproduced in the Monte Carlo with a precision of better than 0.5%.

In the real data analysis, we use vertices reconstructed from the TPC tracks with a sub-millimeter resolution as well as vertices derived from the BBC time of flight measurement with a precision of about 40 cm. To account for this poor resolution, a fraction of the simulated pions had their point of origin artificially smeared in the z direction. This fraction was taken to be 35% of the generated

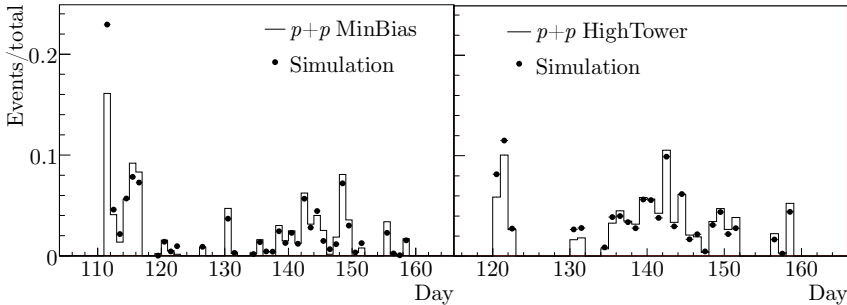


Figure 6.2: Statistics accumulated per day (histogram) and simulated in the Monte Carlo (full circles), for $p + p$ MinBias (left) and HighTower data (right).

pions in case of the $p + p$ MinBias analysis and taken to be zero for all the other datasets since no BBC vertex was used in these sets (see Chapter 4).

In Figure 6.3 we show the η and ϕ distributions of the reconstructed Monte Carlo pions in comparison to the $p + p$ data. The agreement is satisfactory indicating that the calorimeter acceptance is well reproduced in the simulation. In Figure 6.4 the reconstructed p_T of simulated pions is compared to that of pion candidates from the $p + p$ data. It is seen that the HighTower trigger threshold effects are reasonably well reproduced.

In Figure 6.5(a) the background subtracted invariant mass distribution is shown in the region $4 < p_T < 5$ GeV/c obtained from the $p + p$ HighTower-1 data, together with the corresponding distribution from the Monte Carlo. In order to compare the real and simulated invariant mass distributions for all bins in p_T and for all datasets we have estimated the position and width of the peaks by Gaussian fits in the peak region. In Figure 6.5(b) are shown the peak positions obtained from the fit to the $p + p$ data. It is seen that the peak position shifts towards higher masses with increasing p_T . This shift is a manifestation of bin migration effects which originate from statistical fluctuations in the calorimeter response. Due to the steeply falling p_T spectrum the energy resolution will cause a net migration towards larger p_T . Since larger values of p_T imply larger values of $M_{\gamma\gamma}$ the migration effect will bias the invariant mass peak towards larger values. The good agreement between the data and Monte Carlo indicates that such resolution and migration effects are well reproduced.

In Figure 6.5(c) is shown the comparison of the π^0 peak width in data and simulation. The peak width is well reproduced in simulation, which is not surprising since additional smearing was introduced to improve the comparison

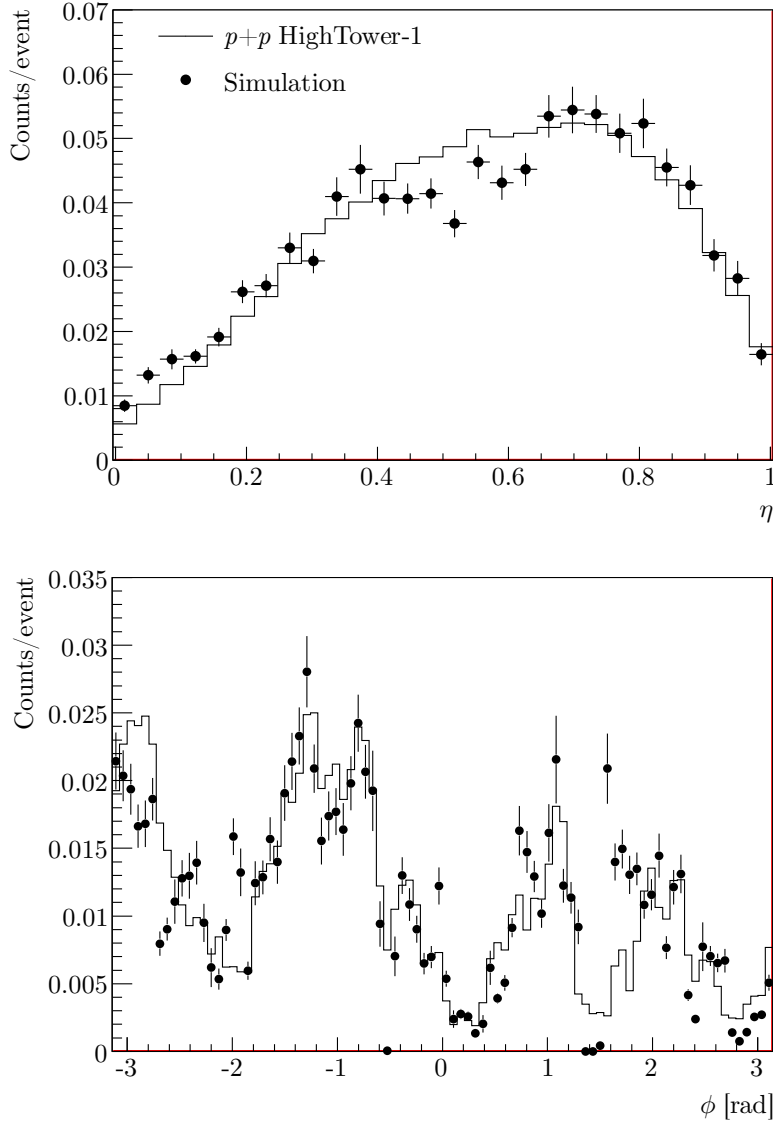


Figure 6.3: Distributions of η (top) and ϕ (bottom) coordinates of the reconstructed Monte Carlo pions, compared to the pion candidates in the $p+p$ HighTower-1 data. The structure seen in the ϕ distribution reflects the azimuthal dependence of the calorimeter acceptance caused by failing SMD modules. This structure is well reproduced in the simulations.

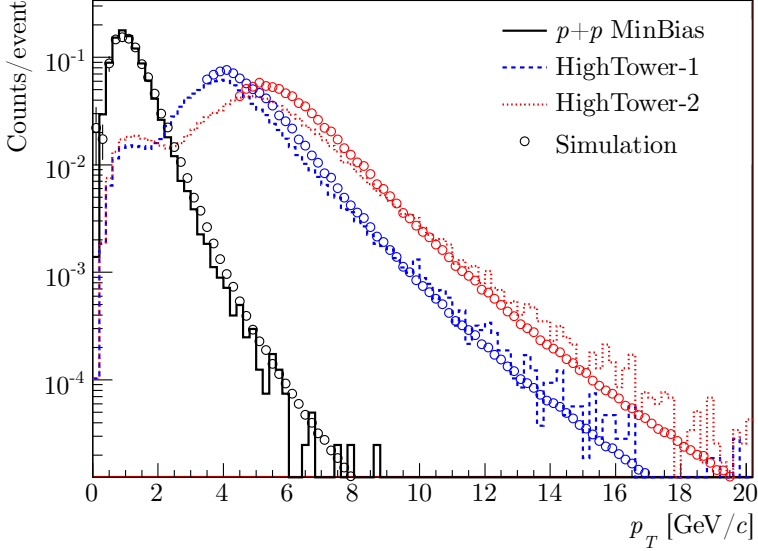


Figure 6.4: Distributions of the reconstructed p_T of the Monte Carlo MinBias, HighTower-1 and HighTower-2 pions, compared to the $p + p$ data.

between data and Monte Carlo, see Figure 6.1.

The acceptance and efficiency correction factor was calculated from the Monte Carlo simulation as the ratio of the raw yield of neutral pions reconstructed in a p_T bin, to the number of simulated pions with the true p_T in that bin. This was done separately for each trigger using the same pion reconstruction cuts as was done in the real data analysis. In particular, the reconstructed value of pseudorapidity was required to fall in the range $0 < \eta < 1$ in both the data and the Monte Carlo while in the latter the generated value of η was also required to fall in this range.

In Figure 6.6 are shown the π^0 and η correction factors for all datasets and triggers used in this analysis.

The large difference between the MinBias and HighTower correction factors is caused by the SMD requirement in the HighTower data, while in the MinBias data we accept all reconstructed BEMC points. The absence of the SMD information also reduces the π^0 reconstruction efficiency at $p_T > 3$ GeV/c, when the decay photons are separated by less than two towers. The η reconstruction starts being affected at larger values of p_T .

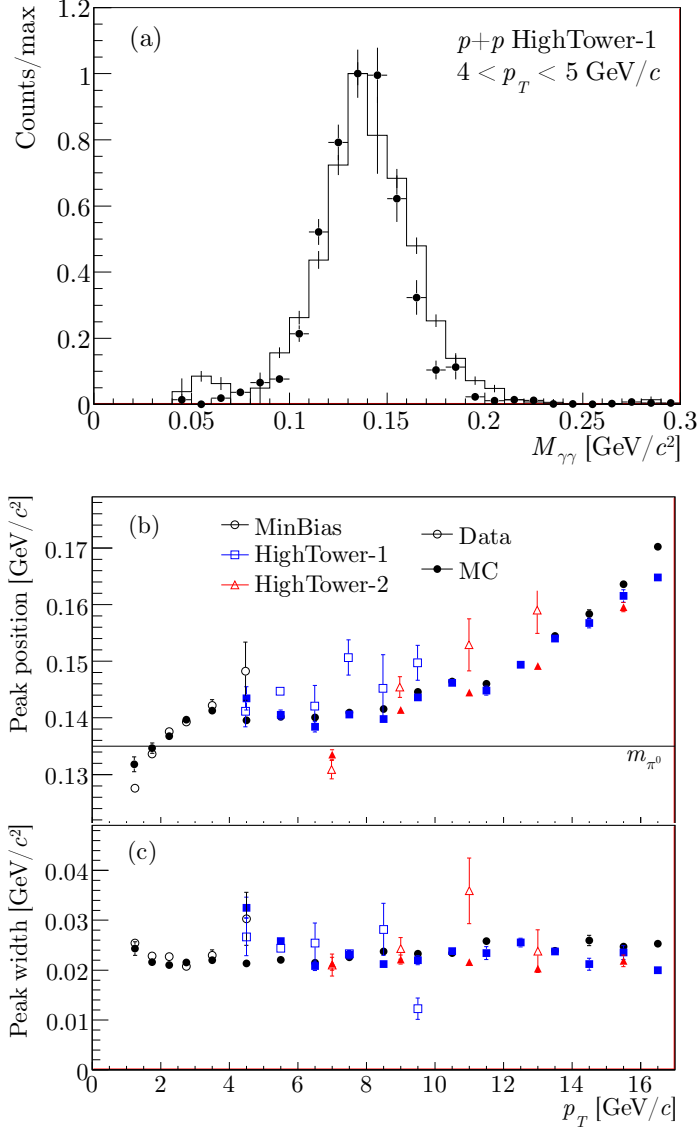


Figure 6.5: Invariant mass spectrum reconstructed in the simulation in comparison to the $p + p$ HighTower-1 data in $4 < p_T < 5 \text{ GeV}/c$ bin (top). Peak position (middle) and width (bottom) in the real data and MC simulation.

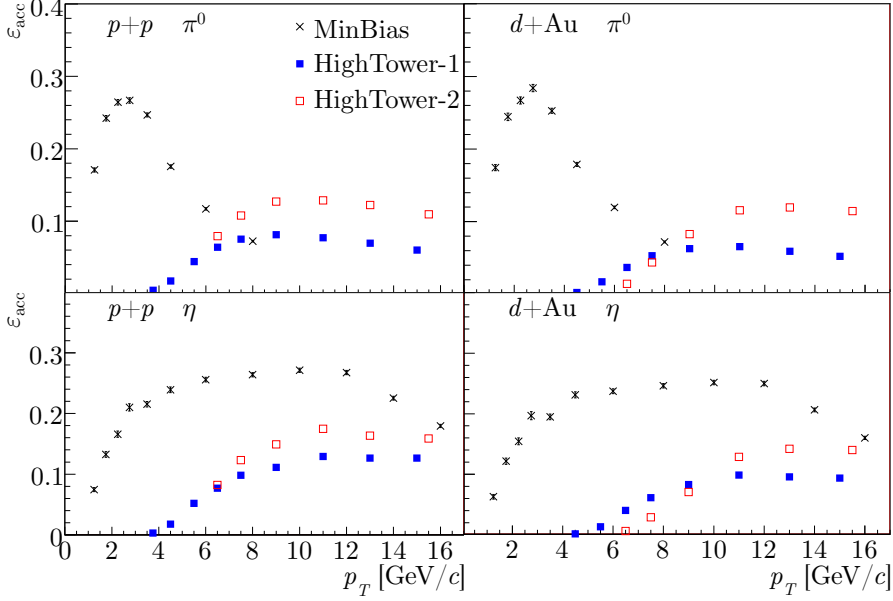


Figure 6.6: Acceptance and efficiency factor ε_{acc} calculated from the Monte Carlo simulation for the $p+p$ (left-hand plots) and $d+\text{Au}$ datasets (right-hand plots). The π^0 and η efficiencies are shown separately in the top and bottom plots, respectively.

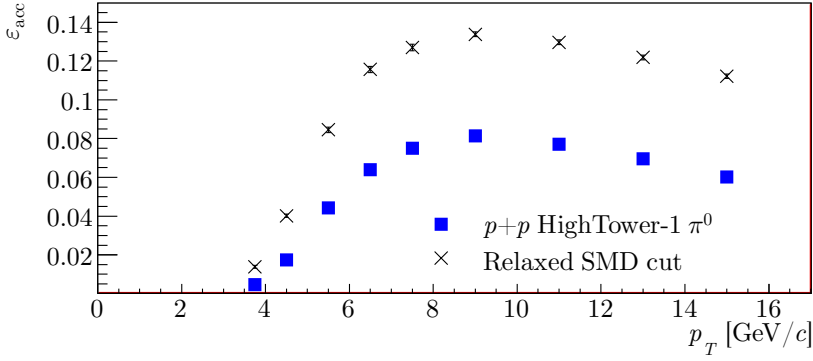


Figure 6.7: Acceptance and efficiency correction for the $p+p$ HighTower-1 data, with standard set of cuts and with SMD quality cut removed.

We have checked the effect of the SMD quality requirement (at least two adjacent strips in a cluster) on the correction factor for HighTower triggered data. In Figure 6.7 is shown the correction factor calculated for the $p + p$ HighTower-1 dataset with (full squares) and without (crosses) the SMD quality requirement. It is seen that this requirement reduces the number of accepted π^0 candidates by about 45%. This explains the difference between the HighTower-1 and HighTower-2 (no SMD quality cut) correction factors at large p_T seen in Figure 6.6.

To verify a possible dependence of the acceptance correction on the track multiplicity and thus on the centrality we have analyzed a sample of generated neutral pions embedded in real $d + \text{Au}$ data. These embedded data are centrally produced by the STAR offline group and are used by several analyses in STAR [73]. No significant centrality dependence was found so that same correction factors were applied to the different centrality classes in the $d + \text{Au}$ data.

6.2 Corrections for random vetoes

This analysis uses the TPC as a veto detector to reject charged particles, which introduces false rejection of photon clusters if an unrelated charged particle happens to hit the calorimeter nearby the cluster. In Figure 6.8 we plot the distribution of distances between the BEMC point and the closest charged track in the event. In this plot one easily distinguishes the peak of real charged particles at small distances, superimposed on a random component which shows up as a shoulder at larger distances. Assuming that the charged tracks are uniformly distributed in η and ϕ around the BEMC point it follows that the radial distribution is given by

$$f(D) = D e^{-D\tau}, \quad (6.3)$$

where the parameter τ has the meaning of the local track density in the region where the photon probes it. This parameter is obtained from a simultaneous fit to the data in all bins of the event multiplicity M , assuming its linear dependence on the multiplicity $\tau = a + bM$. The parametrization (6.3) well describes the random component as shown by the full curve in Figure 6.8. The relative amount of random coincidences is then obtained by integrating the fitted curve up to the distance cut and weighting with the multiplicity distribution observed in each p_T bin. Separate sets of correction factors were calculated for the different triggers in the $p + p$ and $d + \text{Au}$ data. The results are shown in Figure 6.9 as a function of p_T . We have applied a correction factor of $\varepsilon_{\text{cpv}} = 0.94 \pm 0.02$ to

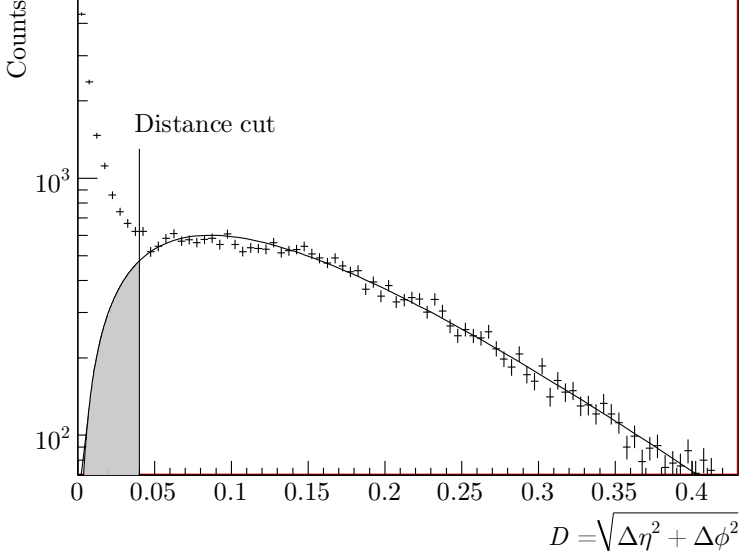


Figure 6.8: Distribution of the distance between BEMC points and the closest track, obtained from $p + p$ HighTower-1 data in the bin $4 < p_T < 5$ GeV/c. The curve shows a fit to Eq. (6.3) and the vertical line indicates the CPV cut.

the $p + p$ datasets and of $\varepsilon_{\text{cpv}} = 0.89 \pm 0.02$ to the $d + \text{Au}$ datasets. The errors assigned to these corrections contribute to a p_T independent systematic error on the corrected π^0 and η yields.

6.3 HighTower trigger scale factors

We have shown in Figure 5.5(c) the p_T distribution of π^0 candidates for the $p + p$ MinBias, HighTower-1 and HighTower-2 data. To match the HighTower spectra to those of the MinBias a p_T -independent scale factor was applied. These scale factors were estimated as the ratio K_{trig} of observed MinBias to HighTower event rates

$$K_{\text{trig}} = \frac{\sum N_{\text{MB}} S_{\text{MB}}}{\sum N_{\text{HT}} S_{\text{HT}}}. \quad (6.4)$$

Here N_{MB} and N_{HT} are the numbers of MinBias and HighTower triggers which pass the event selection cuts described in Chapter 4. The factors S_{MB} and S_{HT}

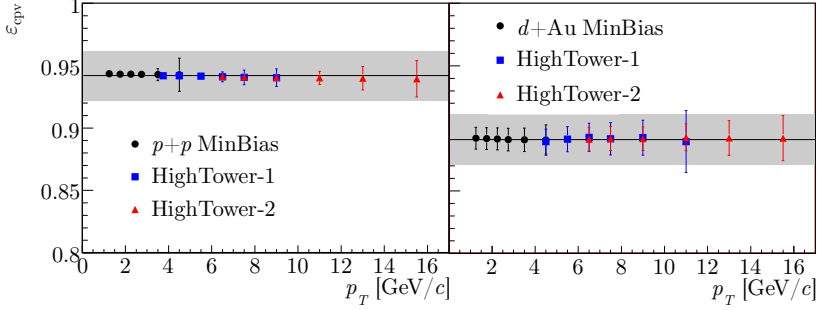


Figure 6.9: Charged particle veto correction in $p + p$ (left) and $d + \text{Au}$ (right) data. The horizontal line indicates the correction factor ε_{cpv} applied to the data while the shaded band corresponds to the systematic uncertainty assigned to the correction factors.

are the hardware prescale factors adjusted on a run-by-run basis to accommodate the DAQ bandwidth. In Eq. (6.4), the sums are taken over all runs where both the MinBias and HighTower triggers were active.

To check the results, the scale factors were also estimated using another method. Here the HighTower software filter (see section 4.5.3) was applied to the minimum bias data. The scale factors were then obtained as the ratio of the total number of MinBias events to the number of those which passed the filter. To obtain a more precise HighTower-1/HighTower-2 relative scale factor, the software filter was applied to the HighTower-1 dataset.

The results from the two methods agree within 3% for HighTower-1 data and within 5% for HighTower-2 data. This is taken as the systematic uncertainties on the trigger scale factors.

6.4 Vertex finding efficiency

In the π^0 reconstruction it is assumed that the decay photons originate from the vertex. It is therefore required that each event entering the analysis has a reconstructed vertex. In the $p + p$ dataset this requirement is always fulfilled because we use the BBC timing information in case the TPC vertex reconstruction fails (this happens in about 35% of the minimum bias events).

In the $d + \text{Au}$ HighTower data, the charged track multiplicities are large enough to always have a reconstructed TPC vertex. However, a TPC vertex is missing in about 7% of the minimum bias events and cannot be recovered

from BBC information because the BBC is not included in the $d + \text{Au}$ minimum bias trigger. Minimum bias events without vertex have low charged track multiplicity and the contribution from these very soft events to the π^0 yield above 1 GeV is assumed to be negligible [74]. Therefore the correction for vertex inefficiency is applied as a constant normalization factor to the yield and its uncertainty contributes to the total normalization uncertainty of the measured cross sections.

The vertex efficiencies were determined to be 0.93 ± 0.01 from a full simulation of $d + \text{Au}$ minimum bias events as described in [74]. However, this efficiency depends on the centrality and we assume that central events are 100% efficient. Scaling the above efficiency by the ratio of peripheral to total number of $d + \text{Au}$ events we obtain an efficiency correction factor of 0.88 ± 0.02 for the sample of peripheral events.

Note that the difference between vertex finding efficiencies in MinBias and HighTower data is effectively absorbed in the scale factor K_{trig} defined in the previous section. The vertex finding efficiency correction is therefore applied to the minimum bias data as well as to the scaled HighTower trigger data.

6.5 Residual beam background contamination

The beam background contamination in the $d + \text{Au}$ minimum bias trigger has been estimated from an analysis of the RHIC empty bunches to be $5 \pm 1\%$ [75]. In our analysis the beam background in $d + \text{Au}$ events is rejected when the energy deposit in the calorimeter is much larger than the total energy of all charged tracks reconstructed in the TPC, see Section 4.5. To estimate the residual beam background in our data we have analysed a sample of 3×10^5 minimum bias triggers from unpaired RHIC bunches. These events were passed through the same analysis cuts and reconstruction procedure as the real data. We observed that about 10% of the fake triggers passed all cuts and that none of these contained a reconstructed π^0 . The residual beam background contamination is thus estimated to be $0.1 \times 5 = 0.5\%$ which is considered to be negligible.

In the $p + p$ data the beam background contamination to the minimum bias trigger rate is also estimated to be negligible due to the BBC coincidence requirement in the trigger and the cut on the BBC vertex position.

6.6 Bin centering scale factors

To assign a value of p_T to the yield measured in a p_T bin the procedure from [76] was applied. Here the measured yield, initially plotted at the bin centers, is approximated by a power law function of the form

$$f(p_T) = \frac{A}{(1 + p_T/p_0)^n}. \quad (6.5)$$

To each bin a momentum p_T^* was assigned as calculated from the equation

$$f(p_T^*) = \frac{1}{\Delta p_T} \int_{\Delta p_T} f(x) dx. \quad (6.6)$$

The function (6.5) is then re-fitted taking p_T^* as the abscissa. This procedure was re-iterated until the values of p_T^* were stable (typically after three iterations). Final fitted curves are shown in Figures 6.11 and 6.12.

For convenience of comparing results from the various datasets the yields were scaled to the p_T bin centers by the ratio K

$$K = \frac{f(p_T^*)}{f(p_T)}, \quad (6.7)$$

where p_T is the center of the bin. The statistical and systematic errors were also scaled by the same factor.

6.7 Jacobian correction

All calculations in this analysis were performed in the defined pseudorapidity region $0 < \eta < 1$ which corresponds to the rapidity region $0 < y < y_0$, where the rapidity limit y_0 is well approximated by pseudorapidity for a particle with momentum much larger than its mass.

The correction was applied to account for the rapidity limit y_0 being not equal to pseudorapidity $\eta = 1$, as shown in Figure 6.10. This correction is smaller than 10% for the η data points at $p_T < 3$ GeV/c, and is negligible for the other data points.

6.8 Fully corrected yields

The fully corrected π^0 invariant yields per minimum bias event in $p + p$ and $d + \text{Au}$ collisions were calculated from Eq. (6.2) and are shown in the top plots

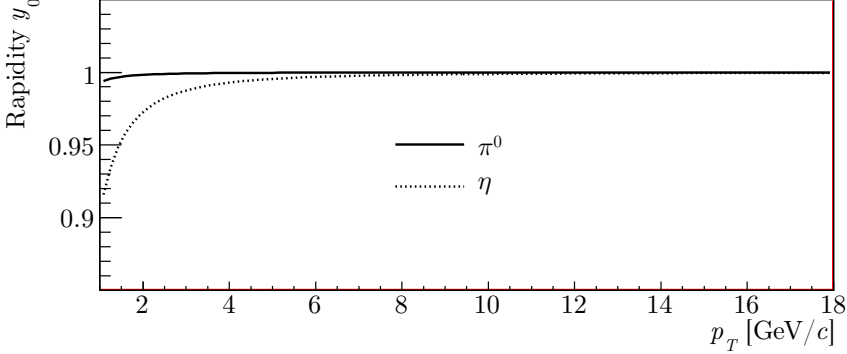


Figure 6.10: Jacobian correction that accounts for the rapidity limit y_0 being not equal to pseudorapidity $\eta = 1$.

of Figure 6.11 and Figure 6.12. The curves in these figures represent a fit of Eq. (6.5) to the data. In the bottom plots are shown the ratios between the data and the fit. From these plots it is seen that the agreement between the datasets taken with the different triggers is satisfactory.

For the calculation of the final cross section results and cross section ratios, the data from three triggers were merged together and only one data point was chosen in each overlapping p_T bin. The HighTower-1 points were preferred over MinBias and HighTower-2 over HighTower-1 because at high p_T data samples are highly correlated while HighTower datasets typically have smaller statistical error.

The systematic uncertainty due to the calorimeter calibration was estimated from

$$\delta f(p_T) = \left| \frac{df}{dp_T} \right| \delta p_T,$$

where δp_T was taken to be 5% in the $d + \text{Au}$ and $p + p$ data (see Section 4.4), and where the derivative was calculated from the fitted function, Eq. (6.5). This p_T -dependent systematic uncertainty is, on average, 38% in the $p + p$ data and 44% in the $d + \text{Au}$ data.

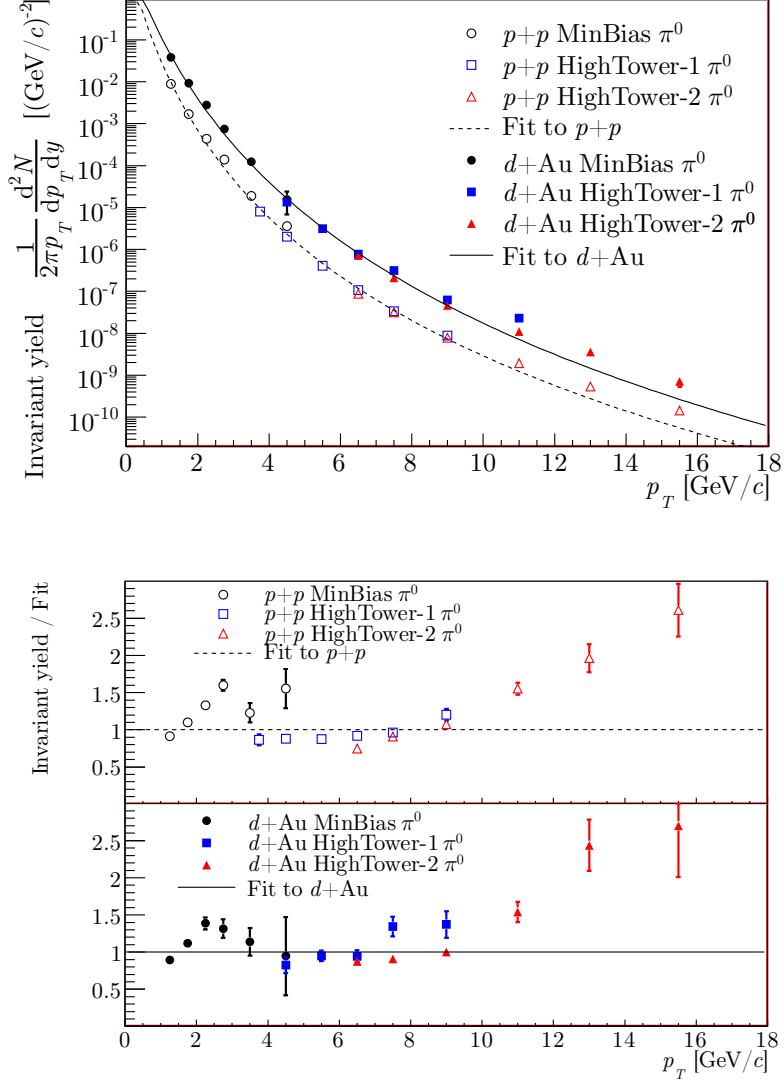


Figure 6.11: Invariant yield of π^0 per minimum bias event in $p+p$ and $d+Au$ collisions (top). Curves are the power law fits given in the text. Invariant yield divided by the fit to the $p+p$ (middle) and $d+Au$ (bottom) data. The errors shown are statistical only.

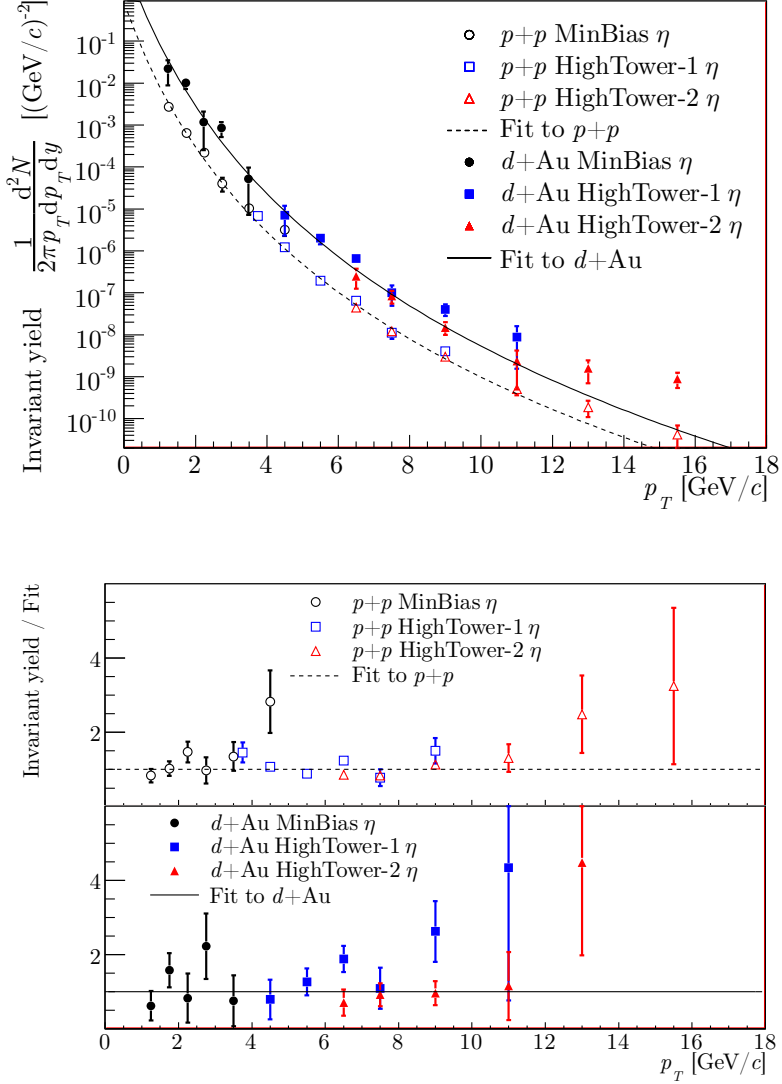


Figure 6.12: Invariant yield of η meson per minimum bias event in $p+p$ and $d+Au$ collisions (top). Invariant yield divided by the fit to the $p+p$ (middle) and $d+Au$ (bottom) data. The errors shown are statistical only.

All systematic error contributions mentioned in this and the previous sections are summarized in Table 6.1, classified into the following categories:

- A point-by-point systematic uncertainty;
- B point-by-point p_T -correlated systematic uncertainty, but uncorrelated between datasets;
- C point-by-point p_T -correlated systematic uncertainty, also correlated between datasets;
- N normalization uncertainty, uncorrelated between datasets.

Table 6.1: Systematic error contributions. The classifications A, B, C and N are defined in the text. The error contributions to the cross section, the η/π^0 ratio, R_{CP} and R_{dA} are indicated in the respective columns. The last column refers to the section where each source of systematic error is described.

Source	Type	$E \, d^3\sigma/d\mathbf{p}^3$	η/π^0	R_{CP}	R_{dA}	Section
Combinatorial background	A	+	+	+	+	5.4
Mixed-event background	C	+	+			5.4
Random vetoes	N	+		+	+	6.2
HighTower scale factors	B	+		+	+	6.3
Analysis cuts	A	+	+	+	+	5.6
Energy scale	B	+			+	6.8
Vertex finding efficiency	N	+		+	+	6.4
Min. bias cross section	N	+			+	4.1
Glauber model N_{coll}	N			+	+	4.6

Chapter 7

Results and discussion

7.1 Cross section

The invariant differential cross section of π^0 and η production in inelastic $p + p$ interactions is given by

$$E \frac{d^3 \sigma_{\text{inel}}^{p+p}}{d\mathbf{p}^3} = E \frac{d^3 \sigma_{\text{NSD}}^{p+p}}{d\mathbf{p}^3} = \sigma_{\text{NSD}}^{p+p} \frac{d^2 N}{2\pi p_T d p_T dy}. \quad (7.1)$$

It has been shown that the singly diffractive (SD) contribution to the inelastic cross section is negligible at $p_T > 1$ GeV/ c [77] so that we can assume that the differential inelastic cross section is equal to the differential NSD cross section in our p_T range. The total NSD cross section in $p + p$ collisions was taken to be $\sigma_{\text{NSD}}^{p+p} = 30.0 \pm 3.5$ mb, as described in Section 4.1. The total hadronic cross section in $d + \text{Au}$ collisions was taken to be $\sigma_{\text{hadr}}^{d+\text{Au}} = 2.21 \pm 0.09$ b [15].

In tables 7.1 and 7.2 we list the cross sections calculated from Eq. (7.1) for the $p + p$ and $d + \text{Au}$ datasets. In the third column of these tables are given the statistical errors while in the remaining columns the quadratic sum of the systematic errors are given separately for each group defined in Table 6.1. In addition to these p_T -dependent systematic errors the quadratic sum of the normalization uncertainties is found to be 12.2% for the $p + p$ and 5.6% for the $d + \text{Au}$ data.

Table 7.1: Invariant cross section of π^0 production measured in $p + p$ collisions. Systematic errors classification given in Section 6.8. Normalization uncertainty of 12.2% is not included.

p_T [GeV/c]	$E \, d^3\sigma/dp^3$ [mb GeV $^{-2}$ c 3]	Statistical error	Systematic errors		
			A	B	C
1.25	2.646×10^{-1}	5.973×10^{-3}	1.336×10^{-2}	9.835×10^{-2}	1.323×10^{-2}
1.75	5.095×10^{-2}	1.217×10^{-3}	2.579×10^{-3}	1.898×10^{-2}	2.548×10^{-3}
2.25	1.314×10^{-2}	4.349×10^{-4}	6.669×10^{-4}	4.902×10^{-3}	6.569×10^{-4}
2.75	4.154×10^{-3}	1.948×10^{-4}	2.115×10^{-4}	1.553×10^{-3}	2.077×10^{-4}
3.50	5.724×10^{-4}	6.062×10^{-5}	2.928×10^{-5}	2.146×10^{-4}	2.862×10^{-5}
4.50	6.076×10^{-5}	2.717×10^{-6}	3.131×10^{-6}	2.293×10^{-5}	3.038×10^{-6}
5.50	1.223×10^{-5}	4.403×10^{-7}	6.353×10^{-7}	4.632×10^{-6}	6.113×10^{-7}
6.50	3.246×10^{-6}	1.248×10^{-7}	1.702×10^{-7}	1.234×10^{-6}	1.623×10^{-7}
7.50	9.592×10^{-7}	2.638×10^{-8}	5.081×10^{-8}	3.681×10^{-7}	4.796×10^{-8}
9.00	2.362×10^{-7}	6.919×10^{-9}	1.272×10^{-8}	9.114×10^{-8}	1.181×10^{-8}
11.00	5.797×10^{-8}	3.029×10^{-9}	3.198×10^{-9}	2.253×10^{-8}	2.898×10^{-9}
13.00	1.632×10^{-8}	1.564×10^{-9}	9.250×10^{-10}	6.389×10^{-9}	8.162×10^{-10}
15.50	4.357×10^{-9}	5.918×10^{-10}	2.559×10^{-10}	1.720×10^{-9}	2.178×10^{-10}

Table 7.2: Invariant cross section of π^0 production measured in $d + \text{Au}$ collisions. Systematic errors classification given in Section 6.8. Normalization uncertainty of 5.6% is not included.

p_T [GeV/c]	$E \, d^3\sigma/dp^3$ [mb GeV $^{-2}$ c 3]	Statistical error	Systematic errors		
			A	B	C
1.25	8.487×10^1	3.716×10^0	4.286×10^0	3.133×10^1	4.244×10^0
1.75	2.052×10^1	9.744×10^{-1}	1.039×10^0	7.648×10^0	1.026×10^0
2.25	6.116×10^0	3.602×10^{-1}	3.104×10^{-1}	2.302×10^0	3.058×10^{-1}
2.75	1.643×10^0	1.556×10^{-1}	8.365×10^{-2}	6.245×10^{-1}	8.215×10^{-2}
3.50	2.709×10^{-1}	4.373×10^{-2}	1.386×10^{-2}	1.044×10^{-1}	1.354×10^{-2}
4.50	3.000×10^{-2}	3.898×10^{-3}	1.546×10^{-3}	1.182×10^{-2}	1.500×10^{-3}
5.50	6.924×10^{-3}	5.282×10^{-4}	3.598×10^{-4}	2.778×10^{-3}	3.462×10^{-4}
6.50	1.573×10^{-3}	1.002×10^{-4}	8.249×10^{-5}	6.457×10^{-4}	7.864×10^{-5}
7.50	4.717×10^{-4}	2.663×10^{-5}	2.499×10^{-5}	1.971×10^{-4}	2.359×10^{-5}
9.00	1.014×10^{-4}	5.453×10^{-6}	5.462×10^{-6}	4.347×10^{-5}	5.071×10^{-6}
11.00	2.439×10^{-5}	2.172×10^{-6}	1.346×10^{-6}	1.081×10^{-5}	1.220×10^{-6}
13.00	7.896×10^{-6}	1.118×10^{-6}	4.475×10^{-7}	3.614×10^{-6}	3.948×10^{-7}
15.50	1.585×10^{-6}	4.056×10^{-7}	9.311×10^{-8}	7.542×10^{-7}	7.926×10^{-8}

To parametrize the p_T dependence, the measured π^0 cross sections were fitted to the power law function from Eq. (6.5), resulting in the following parameters:

Dataset	A [mb GeV ⁻² c ³]	p_0 [GeV/c]	n
$p + p$	7.53×10^2	0.95	9.31
$d + \text{Au}$	4.10×10^4	1.60	10.43

The measured cross sections of π^0 production in $p + p$ collisions are shown in Figure 7.1, compared to the NLO pQCD calculation from Ref. [78]. Input to this calculation are the CTEQ6M parton densities [31] and the KKP fragmentation functions [33]. The factorization scale μ was set equal to p_T and was varied by a factor of two to estimate the scale uncertainty, as indicated by the shaded band in the bottom plot of Figure 7.1 which shows the ratio of the measured cross sections to the QCD prediction.

The errors shown in the plot are the statistical and point-to-point systematic uncertainties added in quadrature excluding the uncertainty due to the energy calibration of the calorimeter. This additional uncertainty is shown by the outer lines around the data points on the lower plot. The normalization uncertainty is indicated by shaded band around unity on the right hand side of the plot.

The π^0 cross section measured in $d + \text{Au}$ collisions is shown in Figure 7.2 and compared to the NLO pQCD calculations of [72]. Here were used the KKP fragmentation functions, the CTEQ6M parton distributions for deuterium and the nuclear parton distributions for Au [79, 80, 81]. The errors shown in the plot are defined in the same way as in Figure 7.1 for $p + p$.

It is seen that the measured π^0 cross section in both the $p + p$ and $d + \text{Au}$ collisions is well described by the pQCD calculation in the full p_T range. The possible excess relative to the theory seen in the $d + \text{Au}$ data at low p_T may be an indication of the Cronin effect which was not included in the pQCD calculations.

In Figure 7.3 we compare the π^0 measurement in $p + p$ and $d + \text{Au}$ with previous measurements of charged pions by STAR [28]. For ease of comparison, the π^\pm data points are divided by the π^0 pQCD curves. Note, that the normalization uncertainty shown by the grey bands in the figure are largely correlated between the π^0 and the π^\pm data points. It is seen that the neutral and charged pion spectra agree with each other very well in both $p + p$ and $d + \text{Au}$ datasets.

In Figure 7.4 we compare the present π^0 measurements with the neutral pion results from PHENIX [78, 20]. This comparison indicates a good agreement, within errors, between the results of the two experiments.

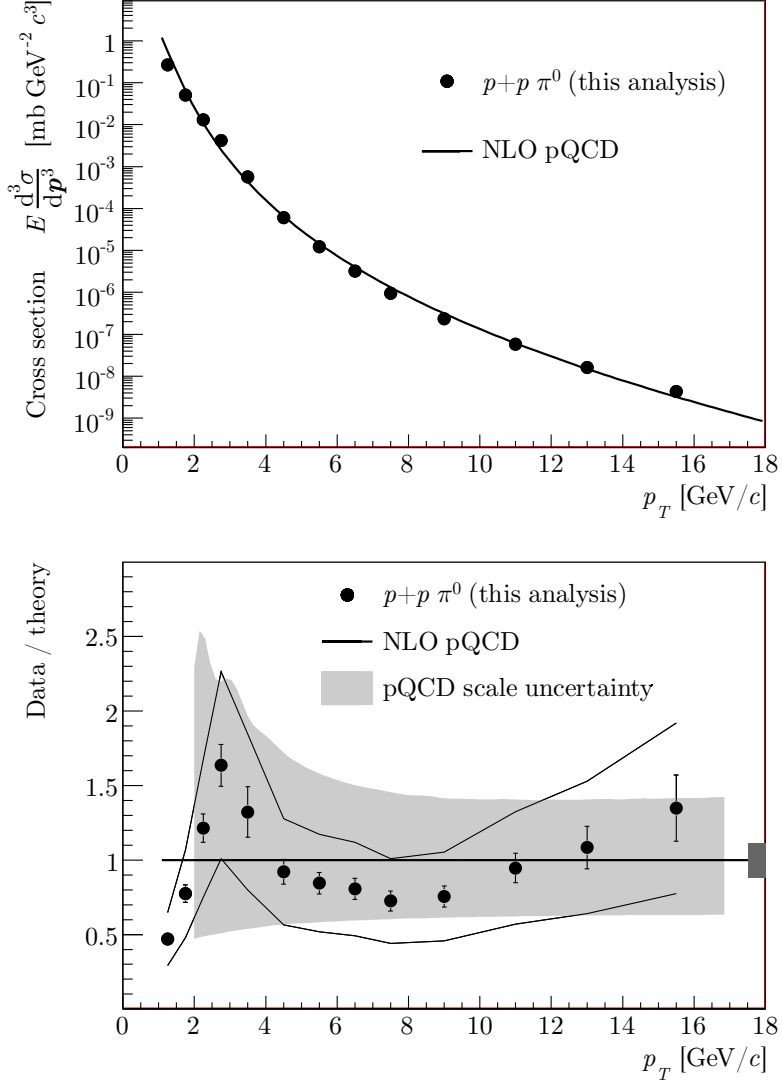


Figure 7.1: Cross section of the neutral pion production in $p + p$ collisions (top), divided by the pQCD calculation (bottom). The errors are statistical and point-to-point systematic, excluding the energy calibration uncertainty shown as the outer lines (bottom). Normalization uncertainty is indicated by a shaded band around unity (bottom).

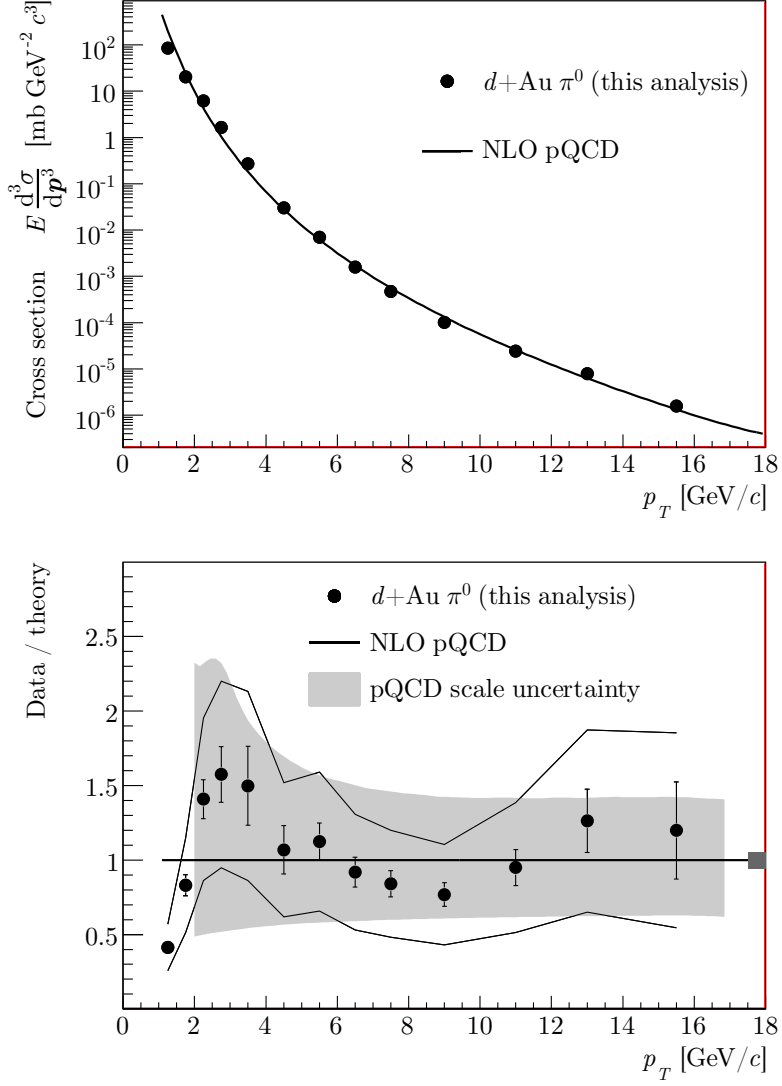


Figure 7.2: Cross section of the neutral pion production in $d + \text{Au}$ collisions (top), divided by the pQCD calculation (bottom). The errors are statistical and point-to-point systematic, excluding the energy calibration uncertainty shown as the outer lines (bottom). Normalization uncertainty is indicated by a shaded band around unity (bottom).

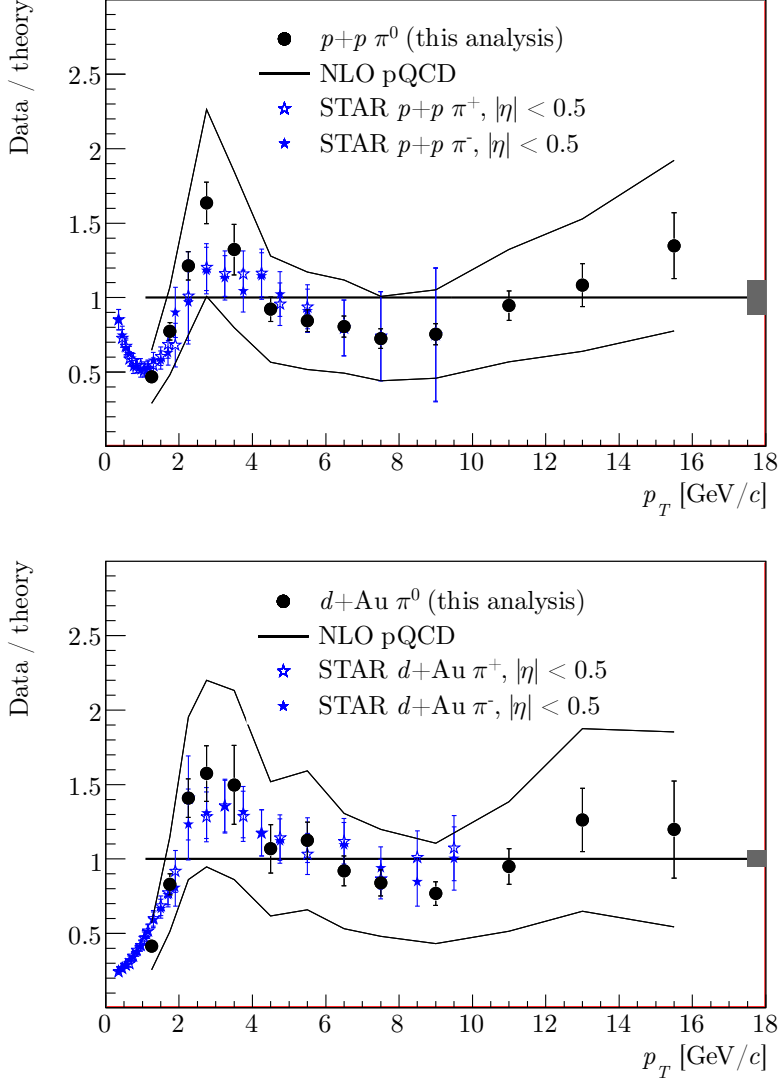


Figure 7.3: Cross section of the neutral pion production in $p + p$ (top) and $d + \text{Au}$ (bottom) collisions divided by the pQCD calculation, compared to the STAR π^\pm [28]. The errors are statistical and point-to-point systematic, excluding the calorimeter energy calibration uncertainty shown as the outer lines. Common normalization uncertainty is indicated by a shaded band around unity.

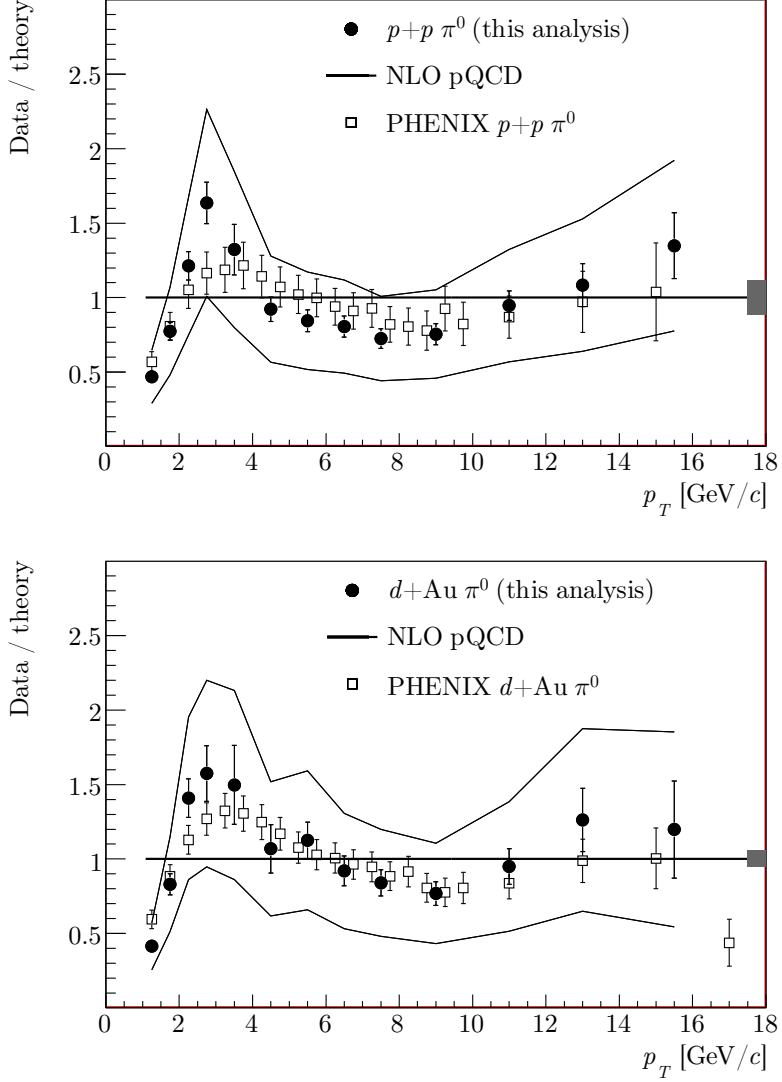


Figure 7.4: Cross section of the neutral pion production in $p+p$ (top) and $d+Au$ (bottom) collisions divided by the pQCD calculation, compared to the PHENIX π^0 measurements in $p+p$ [78] and $d+Au$ [20]. The errors are statistical and point-to-point systematic, excluding the energy calibration uncertainty shown as the outer lines. Normalization uncertainty is indicated by a shaded band around unity.

Table 7.3: η/π^0 ratio measured in $p+p$ collisions. Systematic errors classification given in Section 6.8.

p_T [GeV/c]	η/π^0	Statistical error	Systematic errors A C	
1.25	0.308	0.069	0.045	0.012
1.75	0.380	0.075	0.059	0.015
2.25	0.503	0.097	0.084	0.020
2.75	0.292	0.107	0.052	0.012
3.50	0.545	0.166	0.107	0.022
4.50	0.599	0.054	0.131	0.024
5.50	0.477	0.045	0.116	0.019
6.50	0.593	0.064	0.158	0.024
7.50	0.378	0.038	0.110	0.015
9.00	0.381	0.044	0.125	0.015
11.00	0.263	0.076	0.099	0.011
13.00	0.343	0.147	0.146	0.014
15.50	0.285	0.188	0.139	0.011

7.2 Eta to pion ratio

The η measurement is presented here as the ratio of η to π^0 invariant yields, which allows many systematic uncertainties to cancel, see Table 6.1 in Section 6.8. The η/π^0 ratios measured in $p+p$ and $d+Au$ collisions are listed in Tables 7.3 and 7.4 and are shown in Figure 7.5. The error definitions in the tables and in the plot are the same as described above for the differential cross sections. The present measurement agrees very well with previous PHENIX results [82] as shown by the open squares in the plot. The full curves in Figure 7.5 show the asymptotic ratio $R_{\eta/\pi^0}^\infty = 0.5$ consistent with the world η/π^0 measurements. The constant fit to our data at $p_T > 4$ GeV/c gives $R_{\eta/\pi^0}^{p+p} = 0.42 \pm 0.05$ and $R_{\eta/\pi^0}^{d+Au} = 0.37 \pm 0.08$. The dotted curves in Figure 7.5 show the prediction based on empirical m_T -scaling observation [83] that the hadron production cross sections have the same shape as a function of the transverse mass of the produced particle $m_T = \sqrt{m^2 + p_T^2}$. It is seen that the data are consistent with such scaling behaviour.

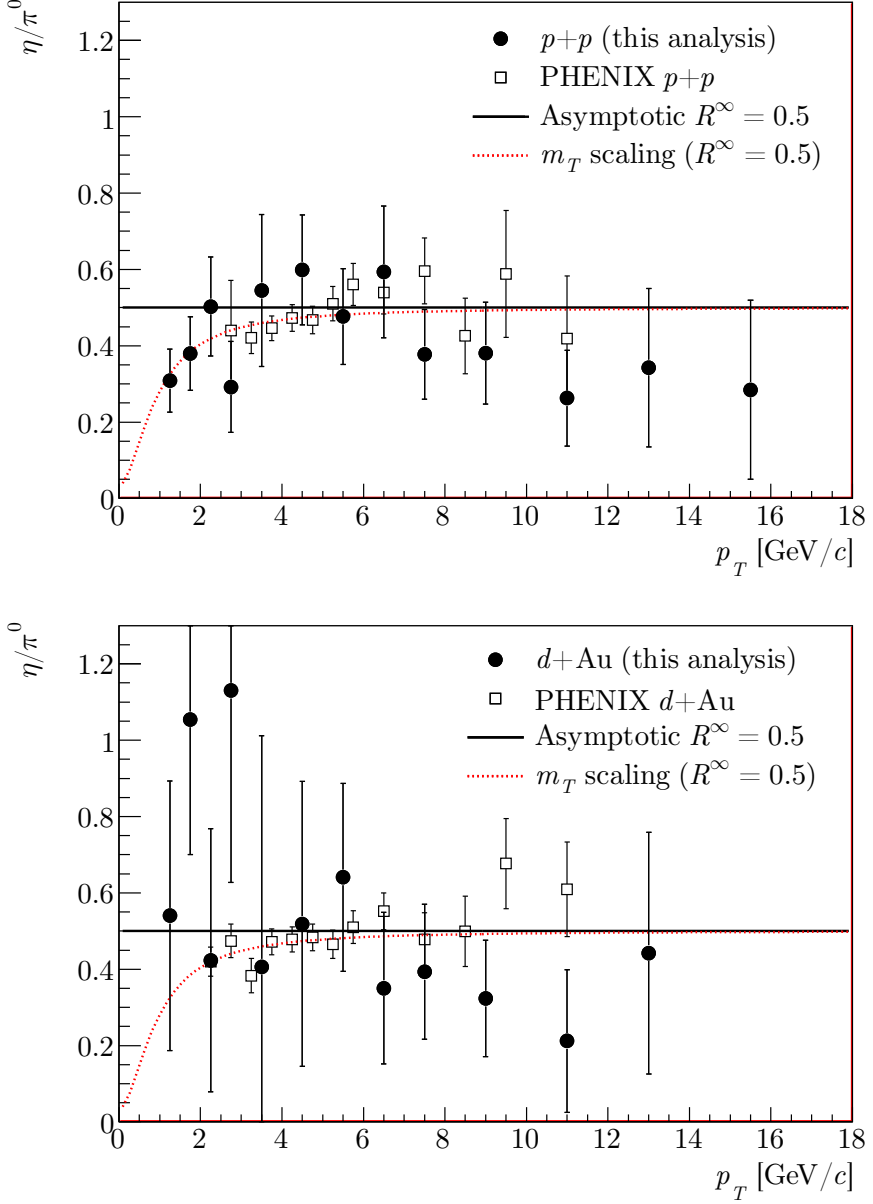


Figure 7.5: η/π^0 ratio measured in $p+p$ (top) and $d+Au$ (bottom) collisions, compared to the PHENIX measurements [82]. Errors are statistical and systematic combined.

Table 7.4: η/π^0 ratio measured in $d + \text{Au}$ collisions. Systematic errors classification given in Section 6.8.

p_T [GeV/c]	η/π^0	Statistical error	Systematic errors A C	
1.25	0.540	0.344	0.078	0.022
1.75	1.054	0.310	0.164	0.042
2.25	0.423	0.337	0.071	0.017
2.75	1.130	0.459	0.202	0.045
3.50	0.406	0.601	0.079	0.016
4.50	0.519	0.355	0.114	0.021
5.50	0.641	0.189	0.156	0.026
6.50	0.350	0.175	0.093	0.014
7.50	0.393	0.134	0.114	0.016
9.00	0.323	0.109	0.106	0.013
11.00	0.212	0.168	0.080	0.008
13.00	0.442	0.254	0.188	0.018

7.3 Nuclear modification factor

We calculate the R_{dA} ratio defined by Eq. (1.9) and (1.10) as

$$R_{dA} = \frac{\sigma_{\text{inel}}^{NN} d^2 N_{dA}/dp_T dy}{\langle N_{\text{coll}} \rangle d^2 \sigma^{p+p}/dp_T dy}, \quad (7.2)$$

where the nucleon-nucleon inelastic cross section $\sigma_{\text{inel}}^{NN}$ is taken to be 42 mb and $\langle N_{\text{coll}} \rangle = 7.5 \pm 0.4$ is calculated from the Glauber model as described in Section 4.6.

The nuclear modification factors for π^0 and η are listed in Tables 7.5 and 7.6 and shown in Figure 7.6.

Again, the definition of the errors is as given for the differential cross sections in Section 6.8. Also shown in Figure 7.6 are the results of R_{dA} for charged pions measured by STAR [28]. A good agreement between STAR neutral and charged pions is observed.

In Figure 7.7 we compare the R_{dA} ratio for π^0 (top panel) and η (bottom panel) to the corresponding PHENIX measurements [82, 84]. Our data agree reasonably well with PHENIX, except at $p_T < 8$ GeV/c where the present results seem to be systematically higher by about 30%.

Table 7.5: Nuclear modification factor R_{dA} for π^0 . Systematic errors classification given in Section 6.8. Normalization uncertainty of 14.5% is not included.

p_T [GeV/c]	R_{dA}	Statistical error	Systematic errors	
			A	B
1.25	0.817	0.040	0.058	0.462
1.75	1.025	0.055	0.073	0.580
2.25	1.185	0.080	0.085	0.670
2.75	1.007	0.106	0.072	0.570
3.50	1.205	0.233	0.087	0.681
4.50	1.257	0.173	0.091	0.713
5.50	1.442	0.122	0.105	0.818
6.50	1.512	0.104	0.111	0.862
7.50	1.252	0.079	0.093	0.714
9.00	1.093	0.067	0.082	0.623
11.00	1.071	0.111	0.083	0.611
13.00	1.232	0.211	0.098	0.702
15.50	0.926	0.268	0.076	0.528

Table 7.6: Nuclear modification factor R_{dA} for η . Systematic errors classification given in Section 6.8. Normalization uncertainty of 14.5% is not included.

p_T [GeV/c]	R_{dA}	Statistical error	Systematic errors	
			A	B
2.75	3.896	2.088	0.840	2.204
3.50	0.898	1.345	0.218	0.508
4.50	1.088	0.736	0.303	0.617
5.50	1.939	0.578	0.612	1.100
6.50	1.053	0.525	0.371	0.600
7.50	1.302	0.456	0.507	0.742
9.00	0.927	0.325	0.413	0.529

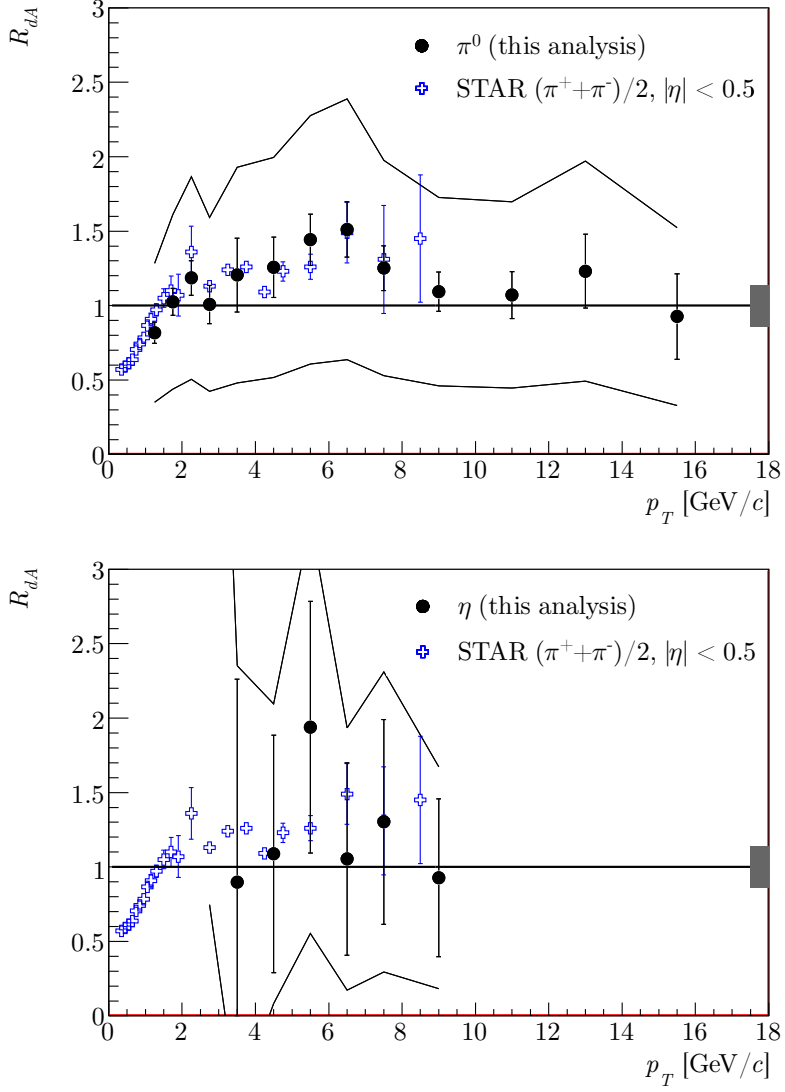


Figure 7.6: R_{dA} ratio for π^0 (top) and η meson (bottom), compared to the STAR π^\pm [28]. Errors are statistical and point-to-point systematic, excluding the calorimeter energy calibration uncertainty shown as the outer lines. Common normalization uncertainty is indicated by a shaded band around unity.

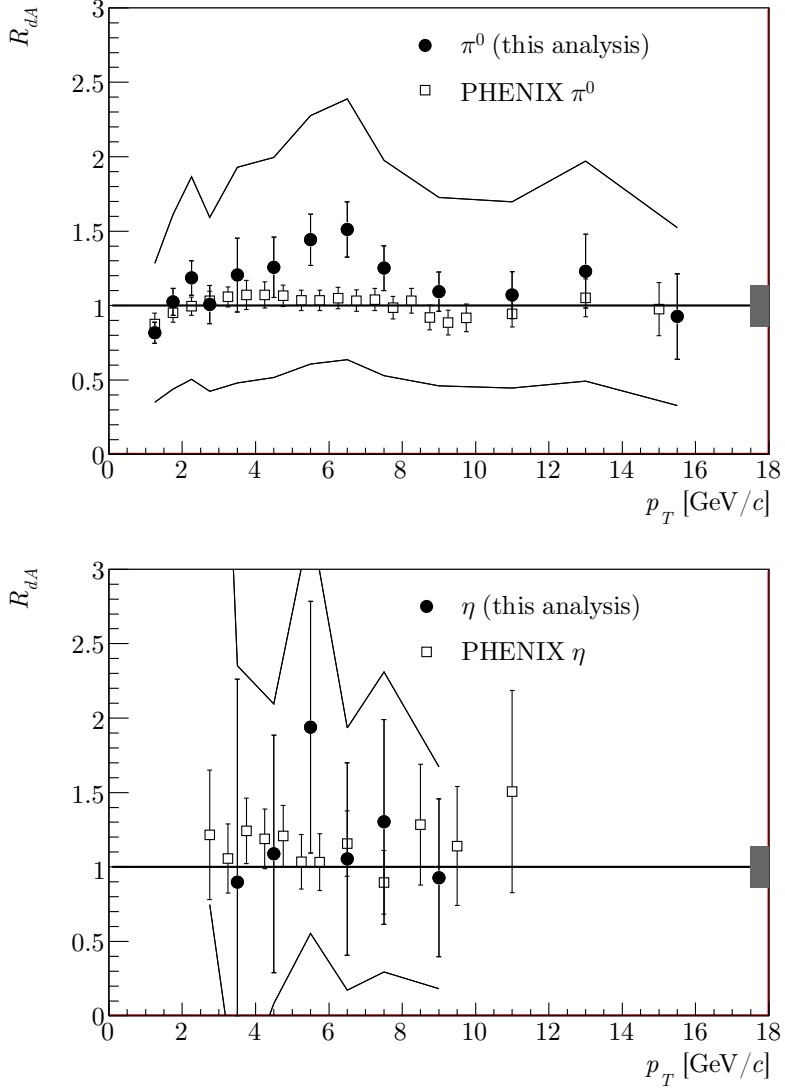


Figure 7.7: R_{dA} ratio for π^0 (top) and η meson (bottom), compared to the PHENIX measurements [82, 84]. Errors are statistical and point-to-point systematic, excluding the energy calibration uncertainty shown as the outer lines. Normalization uncertainty is indicated by a shaded band around unity.

Table 7.7: Nuclear modification factor R_{CP} for π^0 . Systematic errors classification given in Section 6.8. Normalization uncertainty of 11.1% is not included.

p_T [GeV/c]	R_{CP}	Statistical error	Systematic errors	
			A	B
1.25	1.032	0.094	0.073	0.000
1.75	1.177	0.111	0.084	0.000
2.25	1.265	0.164	0.090	0.000
2.75	1.059	0.238	0.076	0.000
3.50	1.211	0.610	0.087	0.000
4.50	1.428	0.236	0.103	0.061
5.50	1.153	0.151	0.084	0.049
6.50	0.859	0.149	0.063	0.036
7.50	1.119	0.106	0.083	0.079
9.00	0.913	0.085	0.069	0.065
11.00	1.095	0.169	0.085	0.077
13.00	0.840	0.211	0.067	0.059
15.50	1.021	0.335	0.084	0.072

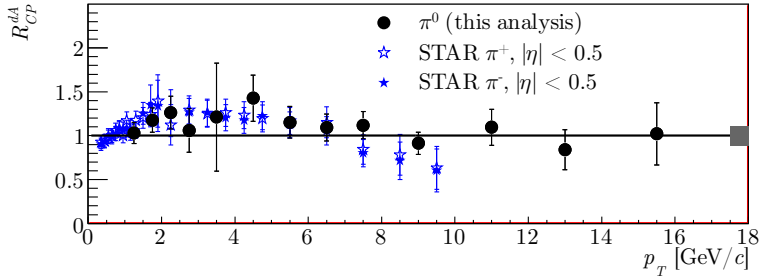


Figure 7.8: R_{CP} ratio measured in $d + \text{Au}$ collisions, compared to STAR charged pions [28]. Errors are statistical and point-to-point systematic. Common normalization uncertainty is indicated by a shaded band around unity.

The R_{CP} ratio for π^0 is listed in Table 7.7 and shown in Figure 7.8 compared to the STAR charged pions [28]. It is seen that the agreement between the neutral and charged pion measurements in STAR is very good. The ratio stays constant at a value consistent with unity beyond $p_T = 8 \text{ GeV}/c$, the indication of a decrease from the charged pion data is not supported by this measurement.

7.4 Conclusions and outlook

There is a good agreement between the π^0 cross sections in $p + p$ and $d + \text{Au}$ collisions and nuclear modification factors measured in the present analysis and the charged pions previously measured in STAR at $p_T < 10 \text{ GeV}/c$. This demonstrates a consistency between the charged and neutral pion results in spite of very different analysis methods and detectors (BEMC versus TPC) used for the measurements. This analysis extends the p_T range of identified hadron measurements in STAR up to $17 \text{ GeV}/c$. There is also a good agreement with the corresponding π^0 cross sections measured by the PHENIX experiment and with those calculated in NLO pQCD.

From the measurement of the nuclear modification factor R_{dA} , no suppression of the π^0 production is seen in the $d + \text{Au}$ collisions compared to $p + p$ collisions. This is in line with the observation made elsewhere [15] that the large suppression seen in the central Au+Au collisions is due to the final state effects.

This analysis presents the first η meson measurement in STAR. The cross section, presented as an η/π^0 ratio, is in agreement with the PHENIX measurement and with the m_T -scaling assumption.

There are several important and unique features in the present analysis. First, the technique of estimating the low invariant mass background using the single photon simulation allows to remove the π^0 contamination at high p_T where this kind of background is indistinguishable from the signal. A possible further improvement would require a better handle on the SMD response simulation. Second, the jet-aligned event mixing method very well reproduces the combinatorial background in the π^0 and η peak region, so that no residual background subtraction is necessary. This eliminates the systematic uncertainty usually related to a residual background parametrization.

It is seen that the experimental uncertainties can be significantly reduced by improving the calorimeter energy calibration. Better measurement in the low p_T region would also require improvements in the simulation of the SMD response. Furthermore, calorimeter-based measurements using data taken since 2006 will benefit from the full $|\eta| < 1$ BEMC acceptance coverage.

In summary, these $p + p$ and $d + \text{Au}$ results provide a baseline measurement for the future Au + Au measurements. These measurements are interesting to shed light on quark number scaling in particle production at intermediate p_T and to study the origin of suppression phenomena at large p_T .

Appendix A

BEMC electronics operation

The tower phototubes are powered by Cockcroft-Walton (CW) bases that are able to keep the high voltage up to a high precision. The bases are programmed through the serial line from a dedicated computer in the Control Room. The analog signals from the phototubes are routed to the tower digitizer crates mounted on the outer side of the magnet.

The tower digitizer crate contains five boards that take 32 analog PMT inputs each and digitize it to 12 bit on each RHIC bunch crossing, storing in the digital pipeline until a level-0 trigger arrives. The crate controller board then sends the data packets to the Tower Data Collector on the platform that feeds it to the DAQ. The crate controller is also responsible for the slow control communication.

The STAR level-0 trigger uses the BEMC data in the form of trigger primitives calculated by the tower digitizer boards, instead of the full tower data. Two trigger primitives are calculated for each tower patch of 0.2×0.2 in $\eta \times \phi$ (4×4 towers) using pedestal subtracted tower ADC:

- *High Tower* - single largest tower signal in a patch
- *Patch Sum* - sum of all 16 towers signal in a patch

In the process of calculating those primitives the on-board FPGA algorithm performs the following operations, as illustrated on Figure A.1:

1. Drop the last 2 bits of the tower ADC, it becomes a 10 bit signal.
2. Subtract the stored pedestal PED from the ADC, mask the channel out if necessary. The pedestals are calculated in a special way as described below.
3. For the High Tower: convert 10 bits into 6 using one of four methods (HT6 selector), then select the largest value of all 16 towers as output.
4. For the Patch Sum: drop the last 2 bits to make it an 8 bit value, then sum those from all 16 channels into a 12 bit value and transform it into the 6 bit output value. The transformation function has a special shape which is described in details later. Internally it uses a lookup table (LUT); the 6 bit number stored in the LUT is the output. The PatchSum trigger sensitivity is therefore fixed:

$$\text{ADC}_{\text{trigger}}^{\text{PatchSum}} = 16 \times \text{ADC}_{\text{tower}}.$$

Finally, two 6 bit numbers are sent to the trigger Data Storage and Manipulation (DSM) boards upon receiving a trigger signal.

The following HT6 methods are available to select 6 of 10 bits for the High Tower output with varying degree of sensitivity, almost equivalent to selecting a constant attenuation factor:

- (0) Select 6 lowest bits, combine five highest bits by logical “and” into the highest bit of the result. This is the most sensitive trigger setting, one HighTower trigger ADC count is equal to 4 raw tower ADC counts.
- (1) Select 6 lower bits starting from 1, combine four highest bits by logical “and” into the highest bit of the result: $\text{ADC}_{\text{trigger}}^{\text{HighTower}} = 8 \times \text{ADC}_{\text{tower}}$
- (2) Select 6 lower bits starting from 2, combine three highest bits by logical “and” into the highest bit of the result: $\text{ADC}_{\text{trigger}}^{\text{HighTower}} = 16 \times \text{ADC}_{\text{tower}}$
- (3) Select 6 lower bits starting from 3, combine two highest bits by logical “and” into the highest bit of the result. This is the least sensitive trigger setting, one HighTower trigger ADC count is equal to 32 raw tower ADC counts.

The tower pedestals and masks, the HT6 selectors and the LUT arrays are prepared and uploaded into the on-board registers via the slow control program.

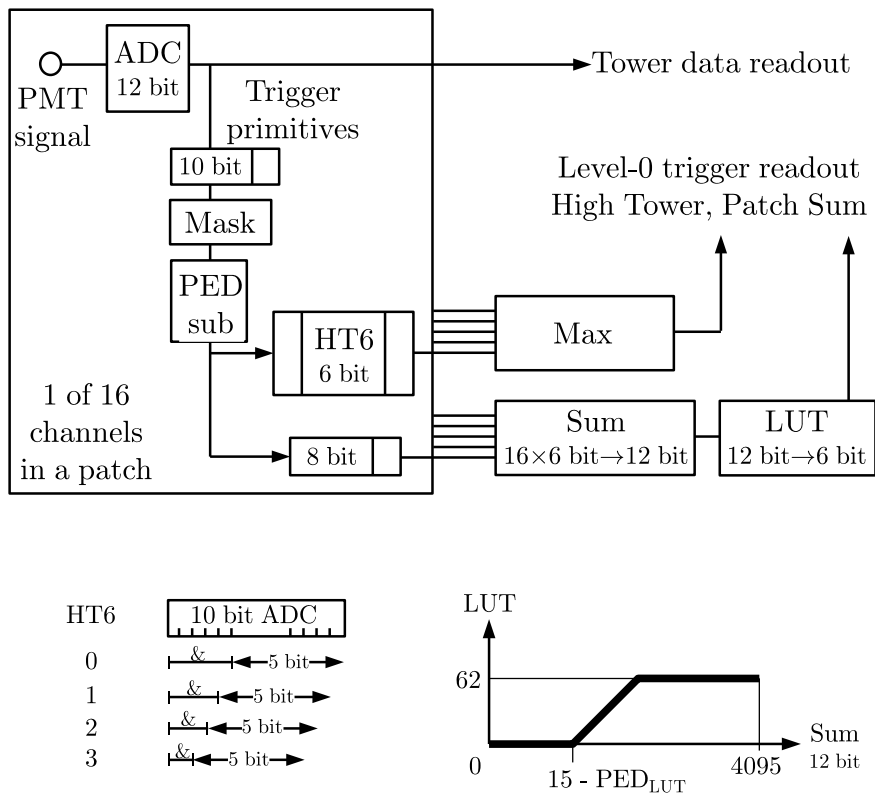


Figure A.1: The digital processing in the tower digitizer boards.

The tower pedestals are being specially prepared in a way that puts the 6 bit High Tower and Patch Sum pedestals at 1 (not zero) to be observed during the run. For each tower the calculation starts from the exact value of the pedestal, which is measured by issuing the software triggers to FEE via slow control in a periods between data taking when there is no beam in the machine. The global “pedestal shift” variable $\text{Pedestal}^{0.5}\text{Shift}$ gets subtracted from the tower pedestal, in order to center the pedestal-subtracted tower signal around $\text{Pedestal}^{0.5}\text{Shift}$. Finally the pedestal gets rounded to the nearest multiple of four and two last bits are removed. If last four bits of the result are used, together with the sign, to fill the 5 bit pedestal register PED in the FEE.

During 2003 data taking run the pedestal subtraction scheme was not yet implemented in the FEE and the HighTower sensitivity was chosen to be $\text{HT6} = 3$. For the 2005 data the settings were $\text{Pedestal}^{0.5}\text{Shift} = 24$ and $\text{HT6} = 2$, which defined $\text{ADC}_{\text{trigger}}^{\text{HighTower}} = \text{ADC}_{\text{trigger}}^{\text{PatchSum}} = 16 \times \text{ADC}_{\text{tower}}$ and thus aligned the HighTower and PatchSum readings around the center of bin 1 in the absense of tower physics signal.

The LUT arrays are prepared in a way that gives a linear response to the patch sum in the range from 0 to 62, to allow diagnosing the broken cables by observing “all ones” bit pattern 63 during the run. With the nominal setting of $\text{Pedestal}^{0.5}\text{Shift} = 24$ each tower contributes a pedestal value $24/16 = 1$ to the sum, so the LUT is constructed from the following three pieces:

- *Zero*, if the sum of 16 towers is below 16

$$\text{LUT}(s) = 0, \quad 0 \leq s < 16$$
- *Linear rise* in response to the sum in the 6 bit range, excluding 63

$$\text{LUT}(s) = s - 15, \quad 16 \leq s < 16 + 63$$
- *Saturation* at 62

$$\text{LUT}(s) = 62, \quad s \geq 16 + 63$$

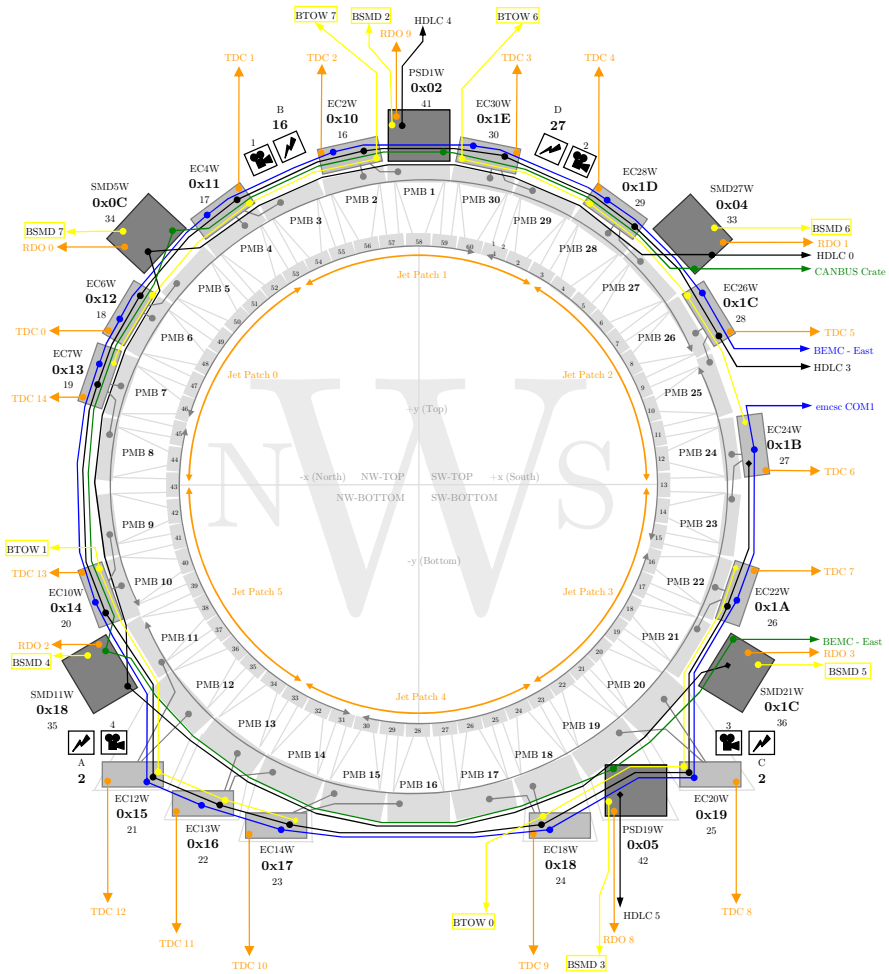
If a tower is masked out of the PatchSum trigger the LUT is modified to accomodate the loss of its pedestal, in this case it starts rising one count earlier than the nominal 16. Therefore the so-called LUT pedestal (PED_{LUT}) is equal to the number of masked towers in a patch.

The SMD electronics (FEE) board is mounted on the $|\eta| = 1$ side of each module. At the FEE board the amplified cathode strip signals are buffered in a switched capacitor array (SCA) before being delivered to external digitizer boards outside of the STAR magnet.

The signals from the pads of the SMD are amplified and stored in an analog pipeline composed of switched capacitor arrays to await the level-0 trigger. Upon level-0 trigger, the SMD analog signals are queued with multiplexing ratio of 80 : 1 to the 10-bit SMD digitizers. SMD digitized signals are first available in STAR level-2 trigger processors in $200\ \mu\text{s}$, still well ahead of digital information from the TPC.

The digitizing electronic boards and crates for preshower detector are identical to the ones used in the SMD.

STAR Barrel Electromagnetic Calorimeter West Side (as seen from +z)



Appendix B

STAR Collaboration

B.I. Abelev,⁹ M.M. Aggarwal,³¹ Z. Ahammed,⁴⁶ B.D. Anderson,²⁰ D. Arkhipkin,¹³ G.S. Averichev,¹² Y. Bai,²⁹ J. Balewski,¹⁷ O. Barannikova,⁹ L.S. Barnby,² J. Baudot,¹⁸ S. Baumgart,⁵¹ V.V. Belaga,¹² A. Bellingeri-Laurikainen,⁴¹ R. Bellwied,⁴⁹ F. Benedosso,²⁹ R.R. Betts,⁹ S. Bhardwaj,³⁶ A. Bhasin,¹⁹ A.K. Bhati,³¹ H. Bichsel,⁴⁸ J. Biecik,⁵¹ J. Bielcikova,⁵¹ L.C. Bland,³ S.L. Blyth,²³ M. Bombara,² B.E. Bonner,³⁷ M. Botje,²⁹ J. Bouchet,⁴¹ A.V. Brandin,²⁷ T.P. Burton,² M. Bystersky,¹¹ X.Z. Cai,⁴⁰ H. Caines,⁵¹ M. Calderón de la Barca Sánchez,⁶ J. Callner,⁹ O. Catu,⁵¹ D. Cebra,⁶ M.C. Cervantes,⁴² Z. Chajecki,³⁰ P. Chaloupka,¹¹ S. Chattopadhyay,⁴⁶ H.F. Chen,³⁹ J.H. Chen,⁴⁰ J.Y. Chen,⁵⁰ J. Cheng,⁴⁴ M. Cherney,¹⁰ A. Chikanian,⁵¹ W. Christie,³ S.U. Chung,³ R.F. Clarke,⁴² M.J.M. Codrington,⁴² J.P. Coffin,¹⁸ T.M. Cormier,⁴⁹ M.R. Cosentino,³⁸ J.G. Cramer,⁴⁸ H.J. Crawford,⁵ D. Das,⁴⁶ S. Dash,¹⁵ M. Daugherty,⁴³ M.M. de Moura,³⁸ T.G. Dedovich,¹² M. DePhillips,³ A.A. Derevschikov,³³ L. Didenko,³ T. Dietel,¹⁴ P. Djawotho,¹⁷ S.M. Dogra,¹⁹ X. Dong,²³ J.L. Drachenberg,⁴² J.E. Draper,⁶ F. Du,⁵¹ V.B. Dunin,¹² J.C. Dunlop,³ M.R. Dutta Mazumdar,⁴⁶ W.R. Edwards,²³ L.G. Efimov,¹² E. Elballili,² V. Emelianov,²⁷ J. Engelage,⁵ G. Eppley,³⁷ B. Erasmus,⁴¹ M. Estienne,¹⁸ P. Fachini,³ R. Fatemi,²¹ J. Fedorisin,¹² A. Feng,⁵⁰ P. Filip,¹³ E. Finch,⁵¹ V. Fine,³ Y. Fisyak,³ J. Fu,⁵⁰ C.A. Gagliardi,⁴² L. Gaillard,² M.S. Ganti,⁴⁶ E. Garcia-Solis,⁹ V. Ghazikhanian,⁷ P. Ghosh,⁴⁶ Y.N. Gorbunov,¹⁰ H. Gos,⁴⁷ O. Grebenyuk,²⁹ D. Grosnick,⁴⁵ B. Grube,³⁵ S.M. Guertin,⁷ K.S.F.F. Guimaraes,³⁸ A. Gupta,¹⁹ N. Gupta,¹⁹ B. Haag,⁶ T.J. Hallman,³ A. Hamed,⁴² J.W. Harris,⁵¹ W. He,¹⁷ M. Heinz,⁵¹ T.W. Henry,⁴² S. Heppelmann,³² B. Hippolyte,¹⁸ A. Hirsch,³⁴ E. Hjort,²³ A.M. Hoffman,²⁴ G.W. Hoffmann,⁴³ D.J. Hofman,⁹ R.S. Hollis,⁹ M.J. Horner,²³ H.Z. Huang,⁷ E.W. Hughes,⁴ T.J. Humanic,³⁰ G. Igo,⁷ A. Iordanova,⁹ P. Jacobs,²³ W.W. Jacobs,¹⁷ P. Jakl,¹¹ P.G. Jones,² E.G. Judd,³ S. Kabana,⁴¹ K. Kang,⁴⁴ J. Kapitan,¹¹ M. Kaplan,⁸ D. Keane,²⁰ A. Kechediyani,¹² D. Kettler,⁴⁸ V. Yu. Khodyrev,³³ J. Kiryluk,²³ A. Kisel,³⁰ E.M. Kislou,¹² S.R. Klein,²³ A.G. Knospe,⁵¹ A. Kocoloski,²⁴ D.D. Koetke,⁴⁵ T. Kollegger,¹⁴ M. Kopytine,²⁰ L. Kotchenda,²⁷ V. Kouchpil,¹¹ K.L. Kowalik,²³ P. Kravtsov,²⁷ V.I. Kravtsov,³³ K. Krueger,¹ C. Kuhn,¹⁸ A.I. Kulikov,¹² A. Kumar,³¹ P. Kurnadi,⁷ A.A. Kuznetsov,¹² M.A.C. Lamont,³ J.M. Landgraf,³ S. Lange,¹⁴ S. LaPointe,⁴⁹ F. Laue,³ J. Lauret,³ A. Lebedev,³ R. Lednicky,¹³ C-H. Lee,³⁵ S. Lehoda,¹² M.J. LeVine,³ C. Li,³⁹ Q. Li,⁴⁹ Y. Li,⁴⁴ G. Lin,⁵¹ X. Lin,⁵⁰ S.J. Lindenbaum,²⁸ M.A. Lisa,³⁰ F. Liu,⁵⁰ H. Liu,³⁹ J. Liu,³⁷ L. Liu,⁵⁰ T. Ljubicic,³ W.-J. Llope,³⁷ R.S. Longacre,³ W.A. Love,³ Y. Lu,⁵⁰ T. Ludlam,³ D. Lynn,³ G.L. Ma,⁴⁰ J.G. Ma,⁷ Y.G. Ma,⁴⁰ D.P. Mahapatra,¹⁵ R. Majka,⁵¹ L.K. Mangotra,¹⁹ R. Manweiler,⁴⁵ S. Margetis,²⁰ C. Markert,⁴³ L. Martin,⁴¹ H.S. Matis,²³ Yu.A. Matulenko,³³ T.S. McShane,¹⁰ A. Meschanin,³³ J. Millane,²⁴ M.L. Miller,²⁴ N.G. Minaev,³³ S. Mioduszewski,⁴² A. Mischke,²⁹ J. Mitchell,³⁷ B. Mohanty,⁴⁶ D.A. Morozov,³³ M.G. Munhoz,³⁸ B.K. Nandi,⁴⁶ C. Nattrass,⁵¹ T.K. Nayak,⁴⁶ J.M. Nelson,² C. Nepali,²⁰ P.K. Netrakanti,³⁴ L.V. Nogach,³³ S.B. Nurushiev,³³ G. Odyniec,²³ A. Ogawa,²³ V. Okorokov,²⁷ D. Olson,²³ M. Pachr,¹¹ S.K. Pal,⁴⁶ Y. Panebratsev,¹² A.I. Pavlinov,⁴⁹ T. Pawlak,⁴⁷ T. Peitzmann,²⁹ V. Perevoztchikov,³ C. Perkins,⁵ W. Peryt,⁴⁷ S.C. Phatak,¹⁵ M. Planinic,⁵² J. Pluta,⁴⁷ N. Poljak,⁵² N. Porile,³⁴ A.M. Poskanzer,²³ M. Potekhin,³ E. Potrebniakova,¹² B.V.K.S. Potukuchi,¹⁹ D. Prindle,⁴⁸ C. Pruneau,⁴⁹ N.K. Pruthi,³¹ J. Putschke,²³ I.A. Qattan,¹⁷ R. Raniwala,³⁶ S. Raniwala,³⁶ R.L. Ray,⁴³

D. Relyea,⁴ A. Ridiger,²⁷ H.G. Ritter,²³ J.B. Roberts,³⁷ O.V. Rogachevskiy,¹² J.L. Romero,⁶ A. Rose,²³ C. Roy,⁴¹ L. Ruan,³ M.J. Russcher,²⁹ R. Sahoo,¹⁵ I. Sakrejda,²³ T. Sakuma,²⁴ S. Salur,⁵¹ J. Sandweiss,⁵¹ M. Sarsour,⁴² P.S. Sazhin,¹² J. Schambach,⁴³ R.P. Scharenberg,³⁴ N. Schmitz,²⁵ J. Seger,¹⁰ I. Selyuzhenkov,⁴⁹ P. Seyboth,²⁵ A. Shabetai,¹⁸ E. Shalaliev,¹² M. Shao,³⁹ M. Sharma,³¹ W.Q. Shen,⁴⁰ S.S. Shimanskiy,¹² E.P. Sichtermann,²³ F. Simon,²⁴ R.N. Singaraju,⁴⁶ M.J. Skoby,³⁴ N. Smirnov,⁵¹ R. Shellings,²⁹ P. Sorensen,³ J. Sowinski,¹⁷ J. Speltz,¹⁸ H.M. Spinka,¹ B. Srivastava,³⁴ A. Stadnik,¹² T.D.S. Stanislaus,⁴⁵ D. Staszak,⁷ R. Stock,¹⁴ M. Strikhanov,²⁷ B. Stringfellow,³⁴ A.A.P. Suaide,³⁸ M.C. Suarez,⁹ N.L. Subba,²⁰ M. Sumner,¹¹ X.M. Sun,²³ Z. Sun,²² B. Surrow,²⁴ T.J.M. Symons,²³ A. Szanto de Toledo,³⁸ J. Takahashi,³⁸ A.H. Tang,³ T. Tarnowsky,³⁴ J.H. Thomas,²³ A.R. Timmins,² S. Timoshenko,²⁷ M. Tokarev,¹² T.A. Trainor,⁴⁸ V.N. Tram,²³ S. Trentalange,⁷ R.E. Tribble,⁴² O.D. Tsai,⁷ J. Ulery,³⁴ T. Ullrich,³ D.G. Underwood,¹ G. Van Buren,³ N. van der Kolk,²⁹ M. van Leeuwen,²³ A.M. Vander Molen,²⁶ R. Varma,¹⁶ I.M. Vasilievski,¹³ A.N. Vasiliev,³³ R. Vernet,¹⁸ S.E. Vigdor,¹⁷ Y.P. Viyogi,¹⁵ S. Vokal,¹² S.A. Voloshin,⁴⁹ M. Wada,¹⁰ W.T. Waggoner,¹⁰ F. Wang,³⁴ G. Wang,⁷ J.S. Wang,²² X.L. Wang,³⁹ Y. Wang,⁴⁴ J.C. Webb,⁴⁵ G.D. Westfall,²⁰ C. Whitten Jr.,⁷ H. Wieman,²³ S.W. Wissink,¹⁷ R. Witt,⁵¹ J. Wu,³⁹ Y. Wu,⁵⁰ N. Xu,²³ Q.H. Xu,²³ Z. Xu,³ P. Yepes,³⁷ I-K. Yoo,³⁵ Q. Yue,⁴⁴ V.I. Yurevich,¹² M. Zawisza,⁴⁷ W. Zhan,²² H. Zhang,³ W.M. Zhang,³⁰ Y. Zhang,³⁹ Z.P. Zhang,³⁹ Y. Zhao,³⁹ C. Zhong,⁴⁰ J. Zhou,³⁷ R. Zoulkarniev,¹³ Y. Zoulkarnieva,¹³ A.N. Zubarev,¹² and J.X. Zhu⁴⁰

(STAR Collaboration)

- ¹Argonne National Laboratory, Argonne, Illinois 60439
²University of Birmingham, Birmingham, United Kingdom
³Brookhaven National Laboratory, Upton, New York 11973
⁴California Institute of Technology, Pasadena, California 91125
⁵University of California, Berkeley, California 94720
⁶University of California, Davis, California 95616
⁷University of California, Los Angeles, California 90095
⁸Carnegie Mellon University, Pittsburgh, Pennsylvania 15213
⁹University of Illinois at Chicago, Chicago, Illinois 60607
¹⁰Creighton University, Omaha, Nebraska 68178
¹¹Nuclear Physics Institute AS CR, 250 68 Řež/Prague, Czech Republic
¹²Laboratory for High Energy (JINR), Dubna, Russia
¹³Particle Physics Laboratory (JINR), Dubna, Russia
¹⁴University of Frankfurt, Frankfurt, Germany
¹⁵Institute of Physics, Bhubaneswar 751005, India
¹⁶Indian Institute of Technology, Mumbai, India
¹⁷Indiana University, Bloomington, Indiana 47408
¹⁸Institut de Recherches Subatomiques, Strasbourg, France
¹⁹University of Jammu, Jammu 180001, India
²⁰Kent State University, Kent, Ohio 44242
²¹University of Kentucky, Lexington, Kentucky, 40506-0055
²²Institute of Modern Physics, Lanzhou, China
²³Lawrence Berkeley National Laboratory, Berkeley, California 94720
²⁴Massachusetts Institute of Technology, Cambridge, MA 02139-4307
²⁵Max-Planck-Institut für Physik, Munich, Germany
²⁶Michigan State University, East Lansing, Michigan 48824
²⁷Moscow Engineering Physics Institute, Moscow Russia
²⁸City College of New York, New York City, New York 10031
²⁹NIKHEF and Utrecht University, Amsterdam, The Netherlands
³⁰Ohio State University, Columbus, Ohio 43210
³¹Punjab University, Chandigarh 160014, India
³²Pennsylvania State University, University Park, Pennsylvania 16802
³³Institute of High Energy Physics, Protvino, Russia
³⁴Purdue University, West Lafayette, Indiana 47907
³⁵Pusan National University, Pusan, Republic of Korea
³⁶University of Rajasthan, Jaipur 302004, India
³⁷Rice University, Houston, Texas 77251
³⁸Universidade de São Paulo, São Paulo, Brazil
³⁹University of Science & Technology of China, Hefei 230026, China
⁴⁰Shanghai Institute of Applied Physics, Shanghai 201800, China
⁴¹SUBATECH, Nantes, France
⁴²Texas A&M University, College Station, Texas 77843
⁴³University of Texas, Austin, Texas 78712
⁴⁴Tsinghua University, Beijing 100084, China
⁴⁵Valparaiso University, Valparaiso, Indiana 46383
⁴⁶Variable Energy Cyclotron Centre, Kolkata 700064, India
⁴⁷Warsaw University of Technology, Warsaw, Poland
⁴⁸University of Washington, Seattle, Washington 98195
⁴⁹Wayne State University, Detroit, Michigan 48201
⁵⁰Institute of Particle Physics, CCNU (HZNU), Wuhan 430079, China
⁵¹Yale University, New Haven, Connecticut 06520
⁵²University of Zagreb, Zagreb, HR-10002, Croatia
(Dated: October 10, 2007)

Bibliography

- [1] CTEQ Coll. Handbook on perturbative QCD. *Rev. Mod. Phys.*, 67:157–248, 1995.
- [2] J. Bjorken and S. Drell. *Relativistic Quantum Mechanics*. McGraw-Hill, 1964.
- [3] J. Cleymans, R. Gavai, and E. Suhonen. Quarks and gluons at high temperatures and densities. *Phys. Rep.*, 130:217, 1986.
- [4] F. Karsch and E. Laermann. Thermodynamics and in-medium hadron properties from lattice QCD. 2003. in Quark Gluon Plasma ed. R. Hwa, hep-lat/0305025.
- [5] D. Rischke. The Quark-Gluon Plasma in equilibrium. *Prog. Part. Nucl. Phys.*, 52:197–296, 2004.
- [6] P. D. B. Collins and A. D. Martin. *Hadron Interactions*. Adam Hilger Ltd, 1984.
- [7] R. Glauber and G. Matthiae. High-energy scattering of protons by nuclei. *Nucl. Phys.*, B21:135, 1970.
- [8] Xin-Nian Wang and Miklos Gyulassy. A systematic study of particle production in $p + p$ (\bar{p}) collisions via the HIJING model. *Phys. Rev. D*, 45:844–856, 1992.
- [9] H. Hahn et al. The RHIC design overview. *Nucl. Instr. and Meth.*, A499:245–263, 2003.
- [10] T. Ludlam. Overview of experiments and detectors at RHIC. *Nucl. Instr. and Meth.*, A499:428–432, 2003.

- [11] A. Franz. Five years of tracking heavy ion collisions at RHIC. *Nucl. Instr. and Meth.*, A566, 2006.
- [12] W. Fischer. Run overview of the Relativistic Heavy Ion Collider. <http://www.agsrhichome.bnl.gov/RHIC/Runs/>.
- [13] J. Bjorken. Highly relativistic nucleus-nucleus collisions: The central rapidity region. *Phys. Rev. D*, 27:140–151, 1983.
- [14] K. Adcox et al. Measurement of the mid-rapidity transverse energy distribution from $\sqrt{s_{NN}} = 130$ GeV Au + Au collisions at RHIC. *Phys. Rev. Lett.*, 87(052301), 2001.
- [15] J. Adams et al. Evidence from $d + \text{Au}$ measurements for final-state suppression of high- p_T hadrons in Au + Au collisions at RHIC. *Phys. Rev. Lett.*, 91(072304), 2003.
- [16] J. Cronin et al. Production of hadrons with large transverse momentum at 200 GeV, 300 GeV and 400 GeV. *Phys. Rev. D*, 11:3105, 1975.
- [17] J. Adams et al. Transverse momentum and collision energy dependence of high- p_T hadron suppression in Au + Au collisions at ultrarelativistic energies. *Phys. Rev. Lett.*, 91(172302), 2003.
- [18] K. Adcox et al. Suppression of hadrons with large transverse momentum in central Au + Au collisions at $\sqrt{s_{NN}} = 130$ GeV. *Phys. Rev. Lett.*, 88(022301), 2002.
- [19] C. Adler et al. Centrality dependence of high- p_T hadron suppression in Au + Au collisions at $\sqrt{s_{NN}} = 130$ GeV. *Phys. Rev. Lett.*, 89(202301), 2002.
- [20] S. Adler et al. Absence of suppression in particle production at large transverse momentum in $\sqrt{s_{NN}} = 200$ GeV $d + \text{Au}$ collisions. *Phys. Rev. Lett.*, 91(072303), 2003.
- [21] J. Adams et al. Experimental and theoretical challenges in the search for the quark gluon plasma: The STAR collaboration’s critical assessment of the evidence from RHIC collisions. *Nucl. Phys.*, A757:102, 2005.
- [22] S. A. Voloshin. Aisotropic flow. *Nucl. Phys.*, A715:379c, 2003.

- [23] D. Molnár and S. A. Voloshin. Elliptic flow at large transverse momenta from quark coalescence. *Phys. Rev. Lett.*, 91(092301), 2003.
- [24] R. J. Fries, B. Müller, C. Nonaka, and S. A. Bass. Hadronization in heavy-ion collisions: Recombination and fragmentation of partons. *Phys. Rev. Lett.*, 90(202303), 2003.
- [25] V. Greco, C. M. Ko, and P. Lévai. Parton coalescence and the antiproton/pion anomaly at RHIC. *Phys. Rev. Lett.*, 90(202302), 2003.
- [26] Z. W. Lin and C. M. Ko. Flavor ordering of elliptic flows at high transverse momentum. *Phys. Rev. Lett.*, 89(202302), 2002.
- [27] Z. W. Lin and D. Molnár. Quark coalescence and elliptic flow of charm hadrons. *Phys. Rev. C*, 68(044901), 2003.
- [28] J. Adams et al. Identified hadron spectra at large transverse momentum in $p+p$ and $d+Au$ collisions at $\sqrt{s_{NN}} = 200$ GeV. *Phys. Lett. B*, 637:161–169, 2006.
- [29] A. Mischke. Neutral pion production in $d + Au$ collisions at $\sqrt{s_{NN}} = 200$ GeV. *Eur. Phys. J.*, C43:311, 2005.
- [30] O. Grebenyuk, A. Mischke, and A. Stolpovsky. High transverse momentum inclusive neutral pion production in $d + Au$ collisions at RHIC. *Rom. Rep. Phys.*, 58:25–30, 2006.
- [31] J. Pumplin et al. New generation of parton distributions with uncertainties from global QCD analysis. *J. High Energy Phys.*, 0207:012, 2002.
- [32] A. Martin, R. Roberts, W. Stirling, and R. Thorne. MRST2001: partons and α_s from precise deep inelastic scattering and Tevatron jet data. *Eur. Phys. J.*, C23:73–87, 2002.
- [33] B. Kniehl, G. Kramer, and B. Pötter. Testing the universality of fragmentation functions. *Nucl. Phys.*, B852:514, 2000.
- [34] J. Binnewies, B. Kniehl, and G. Kramer. Pion and kaon production in e^+e^- and ep collisions at next-to-leading order. *Phys. Rev. D*, 52:4947, 1995.
- [35] L. Bourhis, M. Fontannas, J. Guillet, and M. Werlen. Next-to-leading order determination of fragmentation functions. *Eur. Phys. J.*, C19:89, 2001.

- [36] S. Kretzer. Fragmentation functions from flavor-inclusive and flavor-tagged e^+e^- annihilations. *Phys. Rev. D*, 62(054001), 2000.
- [37] K. Eskola, V. Kolhinen, and C. Salgado. The scale dependent nuclear effects in parton distributions for practical applications. *Eur. Phys. J.*, C9:61–68, 1999.
- [38] D. de Florian and R. Sassot. Nuclear parton distributions at next to leading order. *Phys. Rev. D*, 69, 2004.
- [39] S. Y. Li and Xin-Nian Wang. Gluon shadowing and hadron production at rhic. *Phys. Lett. B*, 527:85, 2002.
- [40] Xin-Nian Wang. Private communication.
- [41] K. Ackermann et al. STAR detector overview. *Nucl. Instr. and Meth.*, A499:624–632, 2003.
- [42] K. Adcox et al. PHENIX detector overview. *Nucl. Instr. and Meth.*, A499:469–479, 2003.
- [43] B. Back et al. The PHOBOS detector at RHIC. *Nucl. Instr. and Meth.*, A499:603–623, 2003.
- [44] M. Adamczyk et al. The BRAHMS experiment at RHIC. *Nucl. Instr. and Meth.*, A499:437–468, 2003.
- [45] M. Beddo et al. The STAR barrel electromagnetic calorimeter. *Nucl. Instr. and Meth.*, A499:725–739, 2003.
- [46] C. Allgower et al. The STAR endcap electromagnetic calorimeter. *Nucl. Instr. and Meth.*, A499:740–750, 2003.
- [47] M. Anderson et al. The STAR time projection chamber: A unique tool for studying high multiplicity events at RHIC. *Nucl. Instr. and Meth.*, A499:659–678, 2003.
- [48] K. Ackermann et al. The Forward Time Projection Chamber (FTPC) in STAR. *Nucl. Instr. and Meth.*, A499:713, 2003.
- [49] C. Adler et al. The RHIC Zero-Degree Calorimeters. *Nucl. Instr. and Meth.*, A470:488, 2001.

- [50] M. Bai et al. RHIC beam instrumentation. *Nucl. Instr. and Meth.*, A499, 2003.
- [51] J. Kiryluk. Relative luminosity measurement in STAR and implications for spin asymmetry determination. *AIP Conf. Proc.*, 675:424, 2003.
- [52] J. Kiryluk. Local polarimetry for proton beams with the STAR Beam Beam Counters. *16th International Spin Physics Symposium Proc.*, 2004. arXiv:hep-ex/0501072.
- [53] S. Bennett et al. The EMC and SMD performance in 1997 testbeam run at BNL. Note 351, STAR, 1997.
- [54] J. Landgraf et al. An overview of the STAR DAQ system. *Nucl. Instr. and Meth.*, A499:762–765, 2003.
- [55] F. Bieser et al. The STAR trigger. *Nucl. Instr. and Meth.*, A499:766–777, 2003.
- [56] A. Drees and Z. Xu. Results from the luminosity scans during the RHIC 2000 run. *Proceedings of the Particle Accelerator Conference*, page 3120, 2001.
- [57] D. Liko. Track fitting in the STAR detector using the Kalman filter method. Note 87, STAR, 1992.
- [58] P. Yepes. A fast track pattern recognition. *Nucl. Instr. and Meth.*, A380:582–585, 1996.
- [59] R. Brun and F. Rademakers. ROOT — an object oriented data analysis framework. *Nucl. Instr. and Meth.*, A389:81–86, 1997. <http://root.cern.ch/>.
- [60] A. Suaide. BEMC calibration in 2003 $d + \text{Au}$ run. STAR, unpublished.
- [61] B. Abelev et al. Measurement of transverse single-spin asymmetries for di-jet production in proton-proton collisions at $\sqrt{s_{NN}} = 200$ GeV. arXiv:hep-ex/0705.4629v1.
- [62] B. Choi. *High p_T inclusive charged hadron distributions in Au + Au collisions at $\sqrt{s_{NN}} = 130$ GeV at RHIC*. PhD thesis, University of Texas, 2003.
- [63] D. Kharzeev, E. Levin, and M. Nardi. QCD saturation and deuteron-nucleus collisions. *Nucl. Phys.*, A730:448–459, 2004.

- [64] L. Hulthén and M. Sugawara. *in Handbuch der Physik*, volume 39. Springer-Verlag, Berlin, 1957.
- [65] M. Miller. *Measurement of jets and jet quenching at RHIC*. PhD thesis, Yale University, 2004.
- [66] Particle Data Group. Review of particle physics. *Eur. Phys. J.*, 3, 1998.
- [67] R. Silver. An algorithm for the assignment problem. *Comm. ACM*, 3:605–606, 1960.
- [68] CERN Program Library. <http://cernlib.web.cern.ch/cernlib/>.
- [69] A. Stolpovsky. *Neutral pion production at $p + p$ and $d + \text{Au}$ collisions at RHIC*. PhD thesis, Wayne State University, 2005.
- [70] B. Abelev et al. Longitudinal double-spin asymmetry and cross section for inclusive jet production in polarized proton collisions at $\sqrt{s_{NN}} = 200$ GeV. *Phys. Rev. Lett.*, 97(252001), 2006.
- [71] R. Brun, R. Hagelberg, M. Hansroul, and J. Lassalle. GEANT: Simulation program for particle physics experiments. user guide and reference manual. Technical Report CERN-DD-78-2-REV, CERN, 1978.
- [72] W. Vogelsang, 2004. Private communication.
- [73] F. Simon. *Production of Λ hyperons at forward rapidity in $d + \text{Au}$ collisions at $\sqrt{s_{NN}} = 200$ GeV*. PhD thesis, Max-Planck-Institut für Physik, Munich, 2005.
- [74] J. Adams et al. Identified particle distributions in $p + p$ and $\text{Au} + \text{Au}$ collisions at $\sqrt{s_{NN}} = 200$ GeV. *Phys. Rev. Lett.*, 92(112301), 2004.
- [75] B. Abelev et al. Rapidity and species dependence of particle production at large transverse momentum for $d + \text{Au}$ collisions at $\sqrt{s_{NN}} = 200$ GeV. arXiv:nucl-ex/0609021.
- [76] G. D. Lafferty and T. R. Wyatt. Where to stick your data points. *Nucl. Instr. and Meth.*, A355:541–547, 1995.
- [77] J. Adams et al. Pion, kaon, proton and anti-proton transverse momentum distributions from $p + p$ and $d + \text{Au}$ collisions at $\sqrt{s_{NN}} = 200$ GeV. *Phys. Lett. B*, 616:8, 2005.

- [78] S. Adler et al. Midrapidity neutral-pion production in proton-proton collisions at $\sqrt{s_{NN}} = 200$ GeV. *Phys. Rev. Lett.*, 91(241803), 2003.
- [79] L. Frankfurt and M. Strikman. Diffraction at HERA, color opacity and nuclear shadowing in DIS off nuclei. *Eur. Phys. J.*, A5:293, 1999.
- [80] L. Frankfurt, V. Guzey, M. McDermott, and M. Strikman. Nuclear shadowing in deep inelastic scattering on nuclei: leading twist versus eikonal approaches. *J. High Energy Phys.*, 0202:027, 2002.
- [81] L. Frankfurt, V. Guzey, and M. Strikman. Leading twist nuclear shadowing: Uncertainties, comparison to experiments, and higher twist effects. *Phys. Rev. D*, 71(054001), 2005. arXiv: hep-ph/0303022.
- [82] S. Adler et al. High transverse momentum η meson production in $p+p$, $d+Au$ and $Au+Au$ collisions at $\sqrt{s_{NN}} = 200$ GeV. *Phys. Rev. C*, 75(024909), 2007.
- [83] M. Bourquin and J.-M. Gaillard. A simple phenomenological description of hadron production. *Nucl. Phys.*, B114:334, 1976.
- [84] S. Adler et al. Centrality dependence of π^0 and η production at large transverse momentum in $\sqrt{s_{NN}} = 200$ GeV $d+Au$ collisions. *Phys. Rev. Lett.*, 98(172302), 2007.

Summary

This thesis presents a measurement of neutral pion and eta meson production in $p + p$ and $d + \text{Au}$ collisions at a center-of-mass energy of $\sqrt{s_{NN}} = 200 \text{ GeV}$, measured with STAR detector at Relativistic Heavy Ion Collider (RHIC) in Brookhaven National Laboratory (BNL, USA).

The present neutral pion spectrum complements that of the charged pions measured in STAR in the transverse momentum range $0.35 < p_T < 10 \text{ GeV}/c$ and extends up to $p_T = 17 \text{ GeV}/c$. There is a good agreement between the neutral and charged pion cross sections in STAR, in spite of very different methods and detectors used in the analysis. The neutral pion cross section also agrees well with the measurements of PHENIX, another large detector at RHIC, and with the theoretical NLO pQCD calculations.

This thesis also presents the first measurements by STAR of eta meson production, which are in agreement with the PHENIX measurements and with the m_T -scaling assumption.

Possible medium-induced modifications of particle production in a nucleus-nucleus collision, compared with an incoherent superposition of nucleon-nucleon collisions, can be observed by measuring the so-called nuclear modification factor R . This thesis presents the measurements of R_{dA} , where the neutral pion production in $d + \text{Au}$ collisions is compared to that in the $p + p$, and R_{CP} , the comparison between central and peripheral $d + \text{Au}$ collisions. Both results are in a good agreement with the charged pion measurements previously done by STAR.

The $p + p$ and $d + \text{Au}$ results presented here provide a baseline measurement for the future $\text{Au} + \text{Au}$ measurements. These measurements are interesting to shed light on quark number scaling in particle production at intermediate p_T and to study the origin of suppression phenomena at large p_T .

Samenvatting

Dit proefschrift beschrijft metingen van neutrale pion en eta meson productie in $p+p$ en $d+Au$ botsingen bij een zwaartepuntsenergie van $\sqrt{s_{NN}} = 200$ GeV, gemeten met de STAR detector bij de Relativistic Heavy Ion Collider (RHIC) in Brookhaven National Laboratory (BNL, USA).

Het neutrale pion spectrum is complementair aan dat van de geladen pionen gemeten met STAR in het transversale impuls gebied $0.35 < p_T < 10$ GeV/ c en loopt door tot $p_T = 17$ GeV/ c . Er is een goede overeenstemming tussen de neutrale en geladen werkzame doorsnede in STAR, ondanks de zeer verschillende methoden en detectoren die gebruikt zijn in de analyse. De gemeten werkzame doorsnede van de π^0 stemt ook goed overeen met de metingen van PHENIX, een andere detector bij RHIC, en met NLO pQCD berekeningen.

Dit proefschrift beschrijft ook de eerste metingen met STAR van eta meson productie, die in overeenstemming zijn met de PHENIX metingen en met de m_T -schaling aanname.

De door het medium geïnduceerde verandering van deeltjes productie in een kern-kern botsing, vergeleken met incoherente superpositie van individuele nucleon-nucleon botsingen, kan waargenomen worden door de zogenaamde “nuclear modification factor” R te meten. Dit proefschrift beschrijft de metingen van R_{dA} , waar π^0 productie in $d+Au$ botsingen vergeleken worden met die in $p+p$ botsingen, en R_{CP} , de vergelijking tussen centrale en perifere $d+Au$ botsingen. Beide resultaten zijn in goede overeenstemming met eerdere metingen aan geladen pionen met STAR.

De $p+p$ en $d+Au$ resultaten die hier gepresenteerd worden zijn een referentie voor toekomstige Au + Au metingen. Deze metingen zijn interessant omdat ze licht werpen op de schaling met het aantal quarks in deeltjes productie bij intermediaire p_T en voor de studie naar de oorsprong van onderdrukkingsfenomenen bij hoge p_T .

Acknowledgements

This thesis would not be finished without saying thanks to people who helped me. Our research group at NIKHEF and Utrecht University created a friendly but demanding atmosphere, it was a real pleasure to be part of it for the last four years.

Help from my promotor Thomas Peitzmann and co-promotor Michiel Botje and a good advise from Raimond Snellings certainly made my work more enjoyable and the research fruitful. I am especially thankful to Michiel for the guidance in the preparation of this thesis, it would be almost unreadable without his extensive comments.

Andre Mischke provided the strong support at the beginning of this work and stayed interested in it ever after. The fellow student Martijn Russcher, doing the research on a related subject, was very helpful in discussing the details of the analysis.

Participating in a large experiment, such as STAR, is a very special experience. Here I would like to name people with whom I have spent more than a year at Brookhaven Lab in 2004–2005. Stephen Trentalange, Oleg Tsai and Alexander Stolpovsky provided a very good and productive working environment, which was also an excellent learning place.

On a separate note, I want to mention here my alma mater, Kiev National University in Ukraine, where I received the master's degree five years ago. In these early days Igor Kadenko and Gennady Zinovjev helped me to choose the path of science, and I will always be grateful for that.

